# A COMBINED SCANNING TUNNELING MICROSCOPE AND SCANNING ELECTRON MICROSCOPE

by ROBIN J.N. COOPE

BASc., University of British Columbia, 1993.

A THESIS SUBMITTED IN PARTIAL FULFILLMENT OF

THE REQUIREMENT FOR THE DEGREE OF

MASTER OF APPLIED SCIENCE

in

THE FACULTY OF GRADUATE STUDIES

(Department of Physics)

We accept this thesis as conforming
to the required standard

THE UNIVERSITY OF BRITISH COLUMBIA

July 1996

In presenting this thesis in partial fulfilment of the requirements for an advanced degree at the University of British Columbia, I agree that the Library shall make it freely available for reference and study. I further agree that permission for extensive copying of this thesis for scholarly purposes may be granted by the head of my department or by his or her representatives. It is understood that copying or publication of this thesis for financial gain shall not be allowed without my written permission.

Department of Physics

The University of British Columbia
Vancouver, Canada

Date August 9 1996

## Abstract

A scanning tunneling microscope (STM) was developed to work in conjunction with a Hitachi S-4100 field emission scanning electron microscope (SEM). To achieve the necessary five degrees of freedom for sample and probe movement, an entirely mechanical method was used, employing pairs of parallelogram flexure hinges actuated by set screws driven through gear reduction. The STM was also configured such that the sample is mounted on the piezoelectric scanner and the probe is fixed. This allowed the sample to be positioned close to the objective aperture of the SEM.

The role of the SEM was envisioned primarily as an alignment tool to position the STM probe over a region of interest on the sample. The STM would then complement the SEM by revealing different surface detail. The instrument was successfully used this way, to image small structures such as Molecular Beam Epitaxy (MBE) and Metal Oxide Chemical Vapor Deposition (MOCVD) grown GaAs/AlGaAs heterostructures and long gate MOSFETs. It was also used to measure the depth of e-beam fabricated calibration pits.

Two methods of STM lithography were investigated. Field evaporation of probe material produced mixed results, due in part to the experiments being done in vacuum. Field evaporation proved a useful method for clearing contamination from the probe. STM probe induced modification of passivated silicon surfaces was also investigated. A voltage threshold for depassivation was found and a model for formation of etch masks at positive polarity was proposed. Patterns were written and successfully transferred to the substrate by wet chemical etch. Lines were as thin as 20 nm, and up to 15 nm high.

An important result of the lithography research was the discovery that the SEM could image depassivated regions at low accelerating voltages. This allowed some light to be cast on a number of STM imaging artifacts, as well as allowing precise calibration of imaging range. Artifacts included the effect of a finite tip radius on imaging steps and

grooves, imaging on highly contaminated surfaces, multiple tips and dielectric material acquired by the probe near the tunneling junction.

The effect of electron beam induced carbon deposition was investigated. The STM was used to measure the depth of thin carbon deposits. A deposition rate of between .6 and 2 nm/sec at 300,000X was found.

**Table of Contents**

**List of Tables**

**List of Figures**

## Acknowledgments

I would like to first thank Dr. Tom Tiedje without whose support and advice this project would never have been successful. I am also indebted to the UBC Physics department for their extensive machine shop facilities, particularly the student machine shop. I would particularly like to thank George Babinger for all of his advice and ideas for the mechanical development of the instrument. To Dr. Tom Pearsall and Steven Konsek I owe thanks for our collaborations on lithography which led to so many interesting discoveries. I also appreciate the contributions of my colleagues, Tom Pinnington, Steve Patitsas, Jim MacKenzie, Alex Busch and Christian Lavoie. Finally I must thank John Cole and Steve Fletcher from Nissei Sangyo Canada, and Martine Normandin of NorTel, for providing samples.

A COMBINED SCANNING TUNNELING MICROSCOPE AND SCANNING ELECTRON MICROSCOPE

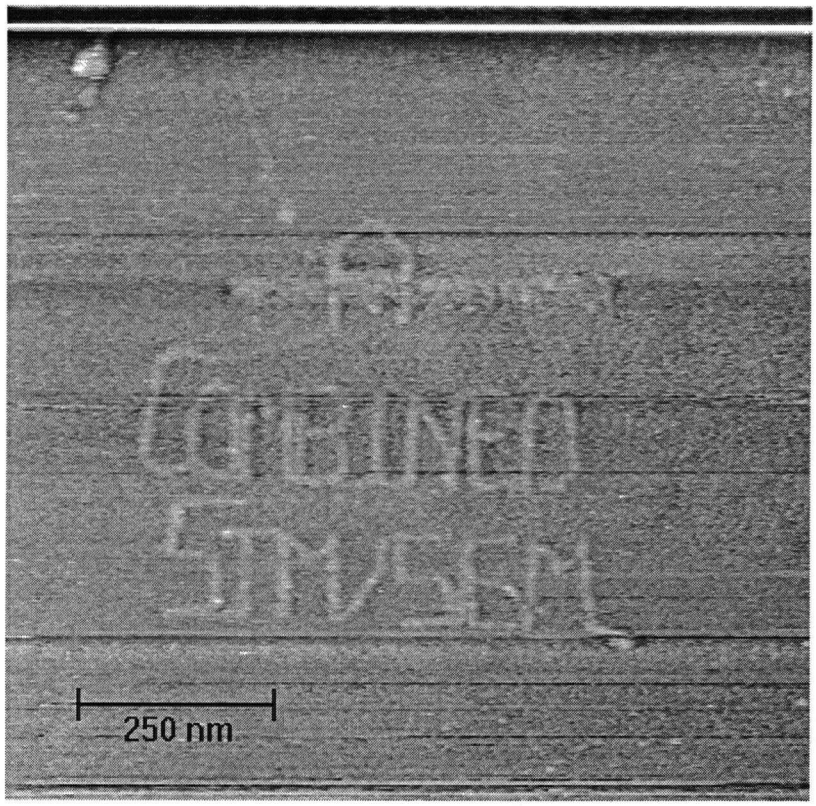


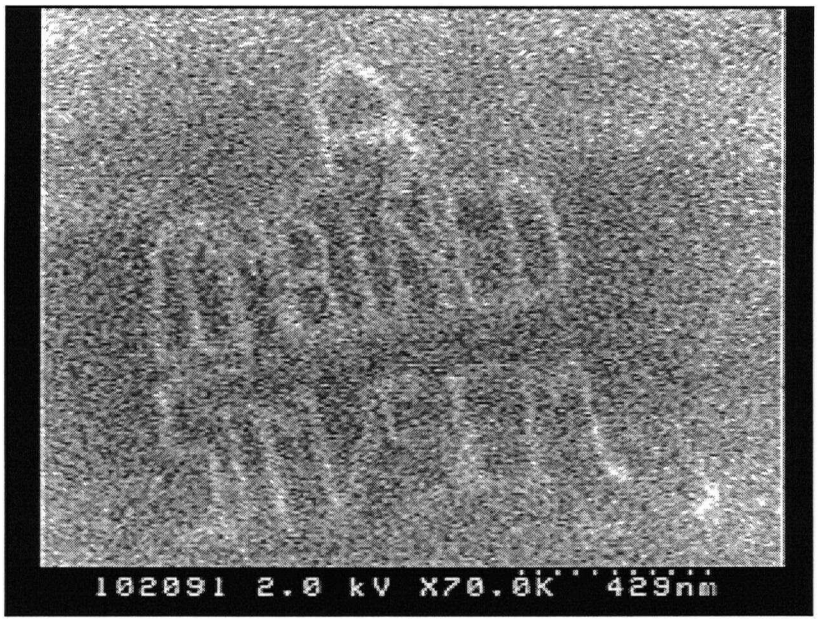


Robin Coope

## 1. Introduction: The Motivation for a Combined SEM/STM

Since its invention[1], the Scanning Tunneling Electron Microscope (STM) has become a popular tool for studying a wide range of materials. Not only can STMs image surfaces with atomic resolution, they have also been used to explore the electrical properties of materials, fabricate nano-scale structures, and manipulate objects on surfaces with great precision. These latter two applications require that the probe of the STM be positioned on the surface with a high level of accuracy. Such a capability is also important for imaging epitaxially grown layers, grain boundaries, semiconductor devices and biological structures whose size is on the order of the STM's scan range.[2] In order to image a specific location on a surface, the STM's probe must be positioned so that the location of interest is within the STM's maximum scan range. Since this region is on the order of 5μm square or less for high resolution instruments, positioning by trial and error is extremely difficult. Accurate positioning in one dimension, to image cross sections of epilayers for example, is quite time consuming. Accurate two dimensional positioning, required to image buried semiconductor devices or specific surface features, is virtually impossible without some external alignment method.

A solution to this problem is to design an STM to work in conjunction with another microscope with a larger field of view. Although it is possible in principle to use an optical microscope as an alignment tool, the short object distance at high magnification would leave insufficient room for the STM's probe. Such an instrument has been built[3] but does not allow simultaneous operation. The Scanning Electron Microscope (SEM) is a much better candidate. The SEM is characterized by a large magnification range, from 10X to 400,000X, excellent depth of field, and a relatively long object distance. With such an instrument, both the STM probe and sample can be simultaneously viewed in focus over a wide range of magnifications. Furthermore, while the SEM can be used to precisely position the STM's probe for imaging specific structures, it is also possible to

take advantage of the different capabilities of the two instruments. The SEM, while less sensitive to surface topography for example, is sensitive to differences in electron density of materials[4] so can show detail different from the STM. The SEM can also be used to observe the quality of the STM tunneling junction, determining for example, whether or not the probe is contacting the surface.

## 2. Design of the STM

### 2.1. Review of Previous Designs

The capability of observing the probe sample junction has been considered important enough that the first combination SEM/STM was developed in 1985 by the group of Gerber, Binnig and Rohrer, the inventors of the STM.[5] Following them have been a number of other implementations, including at least three commercial instruments. A summary of these devices appears in Tables 1.1 and 1.2. There are two broad categories of instruments. The first are dedicated ultra high vacuum (UHV) systems where the SEM is integrated with the STM and often other surface characterization tools, such as RHEED and Auger spectroscopy.[5,17,18] These instruments also usually have tip and sample exchange capability so in situ sample and probe preparation is possible. The other form integrated SEM/STMs take is an STM integrated into a commercial SEM operating in high vacuum (HV). Topometrix's Observer Scanning Probe Microscope, for example, allows tunneling microscopy, atomic force microscopy and lateral force microscopy in conjunction with Hitachi 4000 series SEMs.[19] The instrument described here is also of this type.

Each arrangement has advantages and disadvantages. HV systems are typically less expensive, given an existing SEM. They also tend to have superior SEM performance, due to a combination of shorter objective distances, optimal detector placement, vibration isolation and other factors. The major advantage of UHV systems is lower pressure, typically $10^{-9}$-$10^{-10}$ torr compared to $10^{-6}$-$10^{-7}$ torr for HV. HV STMs cannot image unpassivated semiconductors well, and sample surfaces are subject to hydrocarbon deposition by the electron beam. Operating in UHV avoids this latter problem, which is important for atomic resolution.

Table 2.1: Summary of existing SEM/STM systems. Some range and resolution values were inferred from images.

| Group (et al.) | Date | Vacuum Type | SEM | SEMRes | Simultaneous Op. | Obj. Dist | STM Range (μm) | STM Res | Sample Tilt | Scan Method |
|---|---|---|---|---|---|---|---|---|---|---|
| Gerber (5) | 1985 | UHV | HB-100 | na(1) | Y(2) | 25 cm | <1 | 3Å | 45° | Tp |
| Ichinokawa (6) | 1987 | HV | ISI DS-410 | 30 nm | N(5) | 30 mm | 1 X 1 | 2Å | Varies | Tp |
| Emch (7) | 1987 | UHV | Escalab | na | na | na | 50 X 50 | 20Å | na | Sp |
| Anders (8) | 1987 | HV | Leitz 1200 | na | Y | na | 19.6X 3.5 | na | 45° | Sp |
| Vazquez (9) | 1988 | HV | Jeol 840 | na | Y(2) | 14-29 mm | 1.2 X 1.2 | 3Å | 45° | Tp |
| Takata (10) | 1988 | HV | na | na(1) | na | na | na | 3Å | 45° | Tp |
| Ehrichs (11) | 1990 | UHV(6) | Jeol 820 | 1μm | Y(2) | 5 cm | na | 3Å | 45° | Dp |
| Stemmer (2) | 1991 | HV | Hitachi S-800 | 20 nm | Y | 7 mm | na | na(3) | 45° | Sp |
| Troyon (12) | 1991 | HV | ISI Super II | 20 nm | Y(2) | 10 mm | 0.6X0.6 | 3Å | 45° | Tp |
| Golubok (13) | 1991 | Both(7) | Hitachi S-2500 | 10 nm | Y | 4 mm | 5 X 5 | >2Å | 0-20° | Sp |
| Nakamoto (14) | 1991 | HV | Jeol 820 | 20nm | Y | 30 mm | 2 X 2 | > 4Å | 0(4) | Shear |
| Yamada (15) | 1992 | HV | Hitachi S-2800 | 5 nm | Y | na | na | na | 45° | Sp |
| Rosolen (16) | 1992 | UHV | na | 100 nm | Y | na | na | na | 45° | Sp |
| Thibado (17) | 1994 | UHV | na | >1μm | Y | 25 mm | 2-20 | na | 70° | Sp |
| Omicron (18) | 1994 | UHV | na | 20 nm | Y | 25 mm | na | 3Å | Varies | Sp |
| Topometrix (19) | 1995 | HV | Hitachi S-4XXX | 0.5-2 nm | Y | na | na | 3Å | 45° | Sp |
| Coope | 1995 | HV | Hitachi S-4100 | 2nm | Y | 15 mm | 5X5 | 10Å | 30° | Sp |

**Legend:**

Tp: Tripod Scanner Sp: Single Probe Scanner Dp: Double Probe Scanner

Shear: Piezo Shear Plate scanner

**Notes:**

(1) Vibration problem with STM isolation

(2) Only at low beam current

(3) Biological Samples

(4) Probe at 30°

(5) STM image on SEM screen electron beam

(6) STM in separate chamber with orifice for

(7) Compatible with many SEM's & bakeable

na: Data not available

Table 2.2: Axis actuation for different systems. Column 2 refers to whether the STM mounts on an existing SEM stage. The Added STM axes column show the type of actuation for the different axes between sample and probe. Scan Configuration describes whether the probe or sample is scanned to obtain STM images

| Group | Existing SEM Stage Y/N | Added STM Axes Movement Type X | Y | Z | Scan Configuration | Comments |
|---|---|---|---|---|---|---|
| Gerber | Y | None | None | L | SP | Application of "Pocket Size" STM |
| Ichinokawa | Y | Iw | Iw | Iw | SP | |
| Emch | Y | W | W | StSl | SP | Novel Walker design for Coarse Approach |
| Anders | Y | StSl | StSl | StSl | SP | 3 Tube Walker for XY Baseplate |
| Vazquez | Y | M | M | M | SP | Only STM w/ Mech Axes with bearings |
| Takata | Y | Iw | Iw | Iw | SP | Spring Locked Inchworms |
| Ehrichs | N (Iw) | StSl | StSl | Iw | Sp/SS | Probe has Z, Sample X & Y |
| Stemmer | N | Iw | Iw | Iw | SP | Uses Entire Replacement SEM Stage |
| Troyon | Y | Iw | Iw | Iw | SP | Similar to Gerber's with Extra DoF |
| Golubok | Y | StSl | StSl | StSl | SP | Most Compact & Versatile STM. |
| Nakamoto | Y | W | W | W | SP | |
| Yamada | N (M) | Iw | Iw | Iw | SP | Hitachi V-3000 |
| Rosolen | N | Iw | Iw | Iw | SP | Largest STM, long Working Dist. |
| Thibado | N | Iw | Iw | M | SP | Full Capability UHV Chamber |
| Omicron | N | Iw | Iw | Iw | SP | Full featured UHV Chamber |
| Topometrix | N (M) | Iw | Iw | Iw | SP | STM/LFM/AFM -- "Observer" SPM |
| Coope | N (M) | M | M | M | SS | Only Flexure Hinge Application |

Legend:

L: Louse Motor
M: Mechanical Actuation
W: Piezoelectric Walker
Iw: Inchworm Motor

StSl: Piezoactuated Stick Slip Motion
SP: Scanned Probe (Fine motion on probe)
SS: Scanned Sample (Fine motion on sample)

Some generalizations can be made about these instruments. In all cases, the ability to position the STM probe precisely was cited as the major motivation for development. Generally the instruments using commercial HV SEMs have much better SEM resolution than their custom UHV counterparts. The UHV systems all claim much better resistance to e-beam induced carbon deposition though.[16,17] A number of different actuating techniques have been used, but the majority of systems developed since 1990 use piezoelectric inchworm motors. This likely reflects improvements in commercial inchworm technology. Piezoelectric walkers and "louse"[5] motion systems are no longer used. A commonly cited advantage of piezoelectric actuation is it avoids added mechanical feedthroughs. This is particularly important if the STM is piggybacked onto an existing SEM stage, and in all cases considerably simplifies mechanical design. Another property all but one system share is a sample stage tilted with respect to the SEM's secondary electron detector (SED). Not only does this allow the tip sample junction to be seen better, it causes the SED to see a shadow on the sample behind the probe.

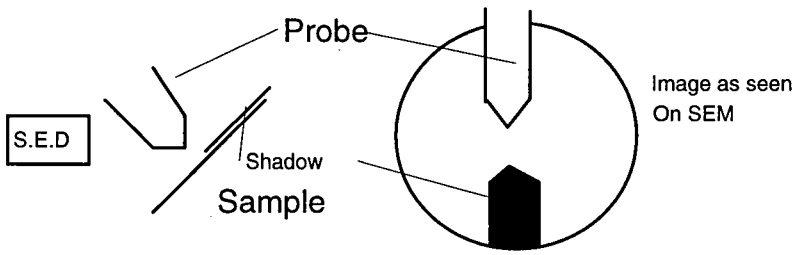


Figure 2.1: Tip shadowing. The shadow is caused by secondary electrons emitted from the surface being stopped by the probe on the way to the detector. The image on screen appears from the perspective of the incident primary electrons.

Tip shadowing, shown in figure 2.1, was cited as a useful aid in coarse probe approach[9,10,17]. The separation between tip and shadow reflects the distance from the probe to the surface. Probe characterization and the ability to gain different information from the same sample were also mentioned. In the following section we describe the

precise requirements for an STM operating in the S-4100 SEM and other design considerations.

## 2.2. Design Requirements

The goal of the combined SEM/STM was to be able to select a region on the sample with the SEM and then scan that region with the STM. To do that, it had to be possible to bring both the desired region of the sample, and the end of the probe, within viewing range of the SEM. That region is the area which can be accessed using the SEM's X and Y beam adjustments. It is about +/- 15μm in X and Y in the case of the Hitachi S-4100. The probe therefore had to move in X and Y over the sample, and the probe and sample had to move together in X and Y with respect to the SEM. In addition, the probe had to move perpendicular to the sample, in the Z direction, to establish the tunneling junction. A total of five degrees of freedom were required, with three degrees of freedom between the probe and sample. The precision of the axes between the probe and sample had to be a fraction of the STM's maximum scan area. The more precise the position of the probe, the less the STM's scan offset controls would have to be used, making the STM easier to operate. The instrument described here used a piezotube with a maximum scan area of 5x5 μm, so a positioning accuracy of at least 1μm or better was required. It was also desirable that each axis have as much range as possible, to minimize prealignment outside the chamber, and maximize the possible sample area which could be accessed by the STM.

A primary requirement of any STM design is that all vibration modes are small in amplitude and above typical frequencies associated with imaging. This is normally done by isolating the STM from the surrounding environment, and making the mechanism between the probe and sample as rigid and light as possible. Both of these strategies are challenging in the context of a combined SEM/STM. The necessity of three degrees of

freedom between probe and sample militates against rigidity. Motion isolation requires the isolated structure be connected to the external environment by a spring of low restoring force. This means the isolated STM can vibrate with respect to the SEM, reducing SEM resolution, or move during axis actuation, so the tunneling junction leaves the SEM's field of view. Vibration in the isolation mechanism has been reported as a problem.[5]

The instrument described here had to satisfy a number of requirements in addition to those detailed above. Cost was a major consideration, which placed constraints on choice of actuation methods, and it was desired that no modifications be made to the SEM stage to use the STM. Piezoelectric inchworm motors and vacuum compatible stepper motors were rejected as actuation mechanisms because of cost and concerns about reliability. Inchworm actuators would have also required the construction or purchase of control software and electronics, a considerable added expense. The only remaining option was a purely mechanical system with manual actuation by rotary feedthroughs. As a result, it was not possible to use the existing SEM stage, as in addition to two electrical feedthroughs, three more mechanical feedthroughs would be required. A replacement stage was necessary.

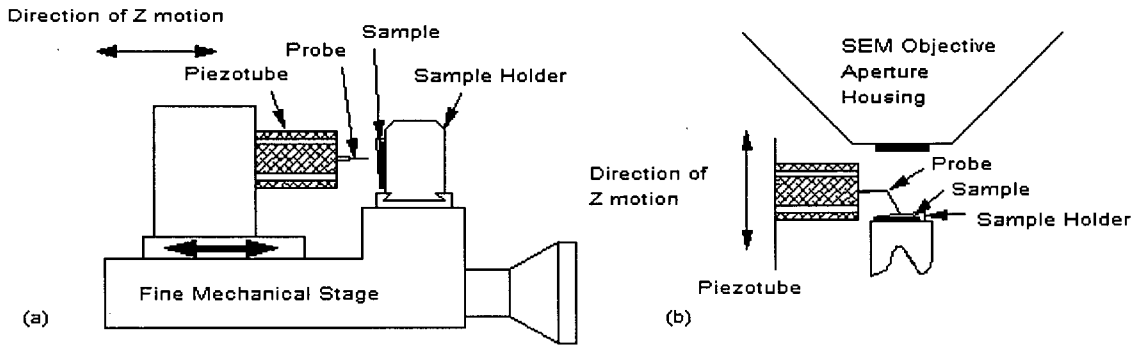


Figure 2.2: Comparison of STM layouts for air operation and a possible SEM configuration

The specimen chamber of the Hitachi S-4100 field emission SEM presented significant challenges for packaging. This instrument has a relatively short objective-

sample distance of about 15mm, and a shallow conical objective housing. Interference between a conventional STM as shown in figure 2.2(a) and the objective housing, would render such a design impracticable. Most integrated SEM/STM's, including Hitachi's own V-3000, have avoided this problem with longer object distances at the expense of resolution.[15]

## 2.3 System Design

A light, compact, and rigid three axis stage without stick slip motion was required for the probe. Some linear translation stages using roller bearings are sufficiently free of stick slip motion for use in an STM, but are expensive and heavy. Instead, motion was obtained with parallelogram flexure hinges, actuated by set screws. Flexure hinges would be potentially less rigid than linear translation stages, but lighter and more compact. Hinges could also be fabricated in house, allowing greater flexibility in the design.

Figure 2.3 shows a parallelogram hinge assembly. The hinges are made from 0.006" stainless steel shim stock with 0.050" stainless steel stiffening plates added to prevent vibrations in the shim stock. The actual hinging occurs in the approximately 1 mm wide bending sections at either end of the hinge. One side of the stiffening plates and end clamps are machined out to produce 0.010" ridges along the edges of the bending sections. That insures that clamping occurs along those edges, and not inside, maximizing stiffness. The hinge is controlled by a combination of springs and a set screw. Depending on the axis, springs either push or pull the hinge against the set screw, which is located so that it moves the free end of the hinge. Figure 2.3 shows the configuration used for the probe and sample Y axes.

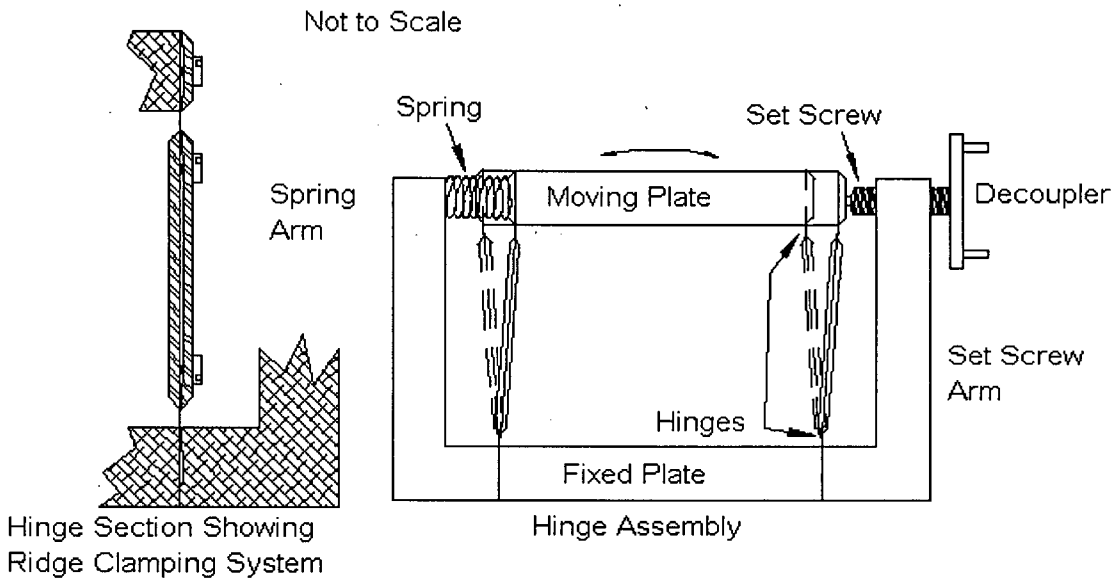


Figure 2.3: The hinge mechansim

The three degrees of freedom between the probe and sample were achieved by adopting the design of Hall et al.[20] This is a three axis flexure hinge stage which arranges each pair of hinges sequentially in the form of a cube, with the last hinge moving in three dimensions. Figure 2.4 shows the final version of this stage. From the base, the X hinge moves the rest of the assembly back and forth. It is actuated by a set screw mounted in a block behind the stage, and constrained by tension springs attached to the same block. The Z axis is next. It is actuated directly by a worm gear driven set screw from the top of the stage. The bearing mounts shown in figure 2.4 hold the worm for this axis. Both tension springs at the sides and a compression spring below constrain the hinge. To the movable end of the Z hinge is attached the X hinge assembly, shown separately. It uses the control arm arrangement with a compression spring, shown in figure 2.3.

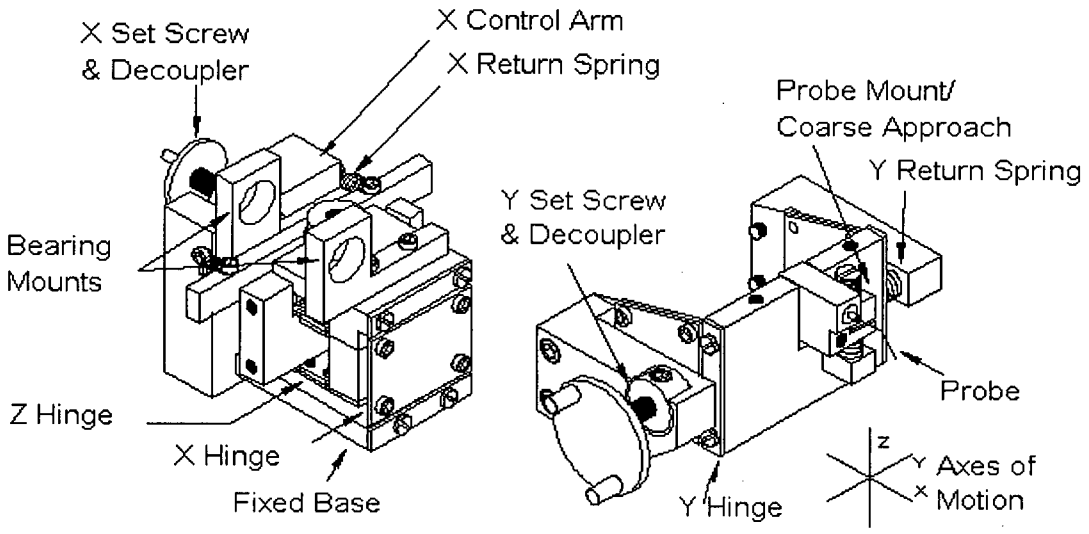


Figure 2.4. Exploded view of the three axis probe stage

The sample's Y movement, shown in figure 2.5, is similar to the probe's, with a single set of hinges with control arms. The piezotube itself is made from PZT-5 and is 20.4 mm long, 10 mm wide and has a wall thickness of 0.84 mm. Maximum electrode voltage is 200V and the tube is shielded with a grounded aluminum cylinder. The samples mount on standard SEM mounting stubs although most experiments were done on insulating sample holders to facilitate tip ablation (Section 7.2) Sample stubs are secured by a set screw in an aluminum plug, glued to the top of the piezotube. Table 2.3 shows the range of the axes.

Table 2.3: The range of the different axes

| Axis | Range |
|---|---|
| Probe X Axis | 2 mm |
| Probe Y Axis | 3 mm |
| Probe Z Axis | 2 mm |
| Sample Y Axis | 2 mm |
| Probe/Sample X Axis | 5 mm |

The STM chassis, shown in figure 2.6, is laid out in the following way. The back plate has five rotary feedthroughs and two electrical feedthroughs, one for the high voltage control signals and one for the tip current signal. The STM preamplifier is mounted beside the sample Y gearbox. The STM is mounted on a horizontal chassis which is attached to the back plate. The chassis houses the probe/sample X stage which

uses linear bearings on 3/16" steel rods. The rods can be removed by removing the ram plate, which acts as a stop for the SEM's pneumatic stage lock. This stage also decouples the STM from the rest of the assembly with four viton shock mounts similar to those found in hard disk assemblies. The probe and sample stages are mounted to the isolated plate by slotted screws. This affords some fine lateral adjustment to ensure that with the Y axes centered, the SEM is aiming at the center of the sample holder. The larger range of the sample/probe X axis satisfies this requirement in the X direction.

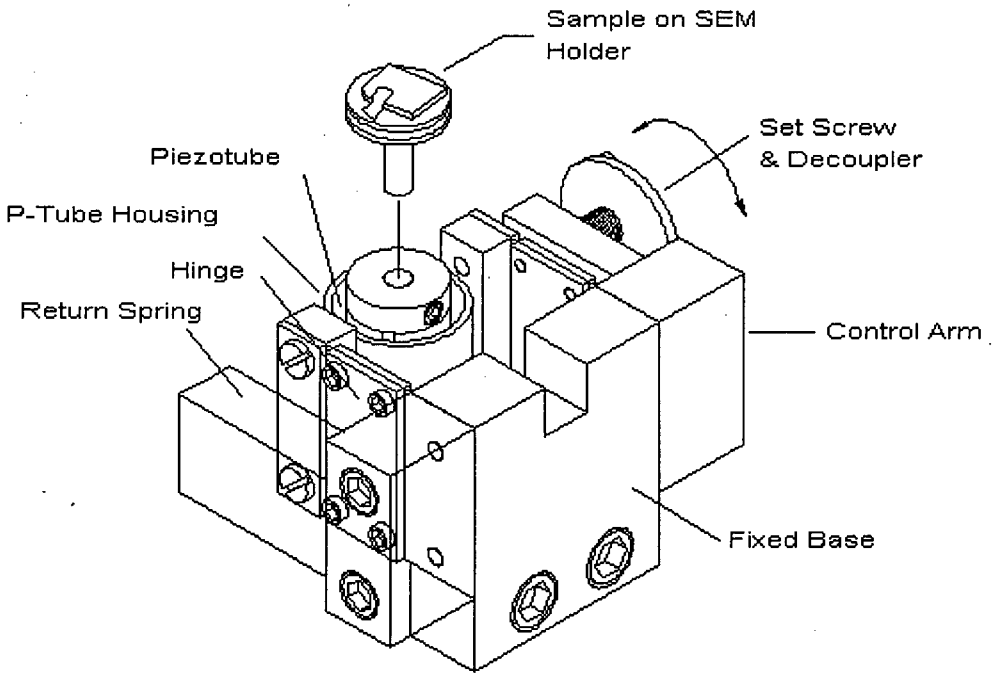


Figure 2.5: Sample stage with piezotube and Y axis hinge

Most designs use an existing XY stage below the STM to position the probe and sample together, then move either the sample or probe independently into the SEM's field of view. In this case, a lack of space in the SEM chamber made adding a linear translation stage for the Y axis difficult. For that reason, an independent Y movement was added to the sample, which is the mechanism shown in figure 2.5 This arrangement is not optimal, as it adds an extra degree of freedom in the probe sample loop, but the

extra movement is much stiffer than the probe stage, so does not reduce the performance of the STM.

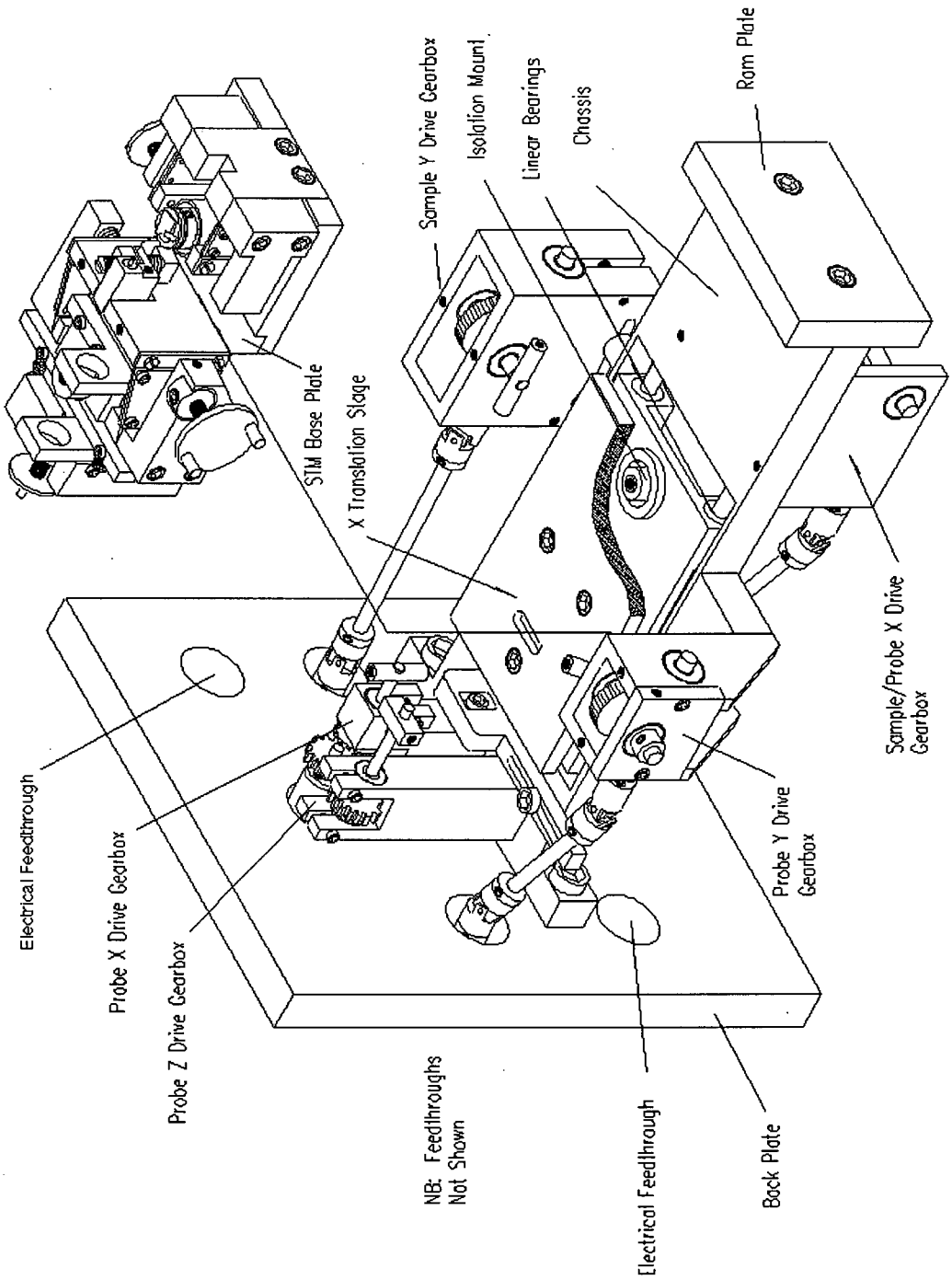


Figure 2.6: Exploded view of the complete STM showing the isolation mounts and linear bearing assembly.

The isolation mounts were found to reduce the average noise in the feedback loop (measured with the STM stationary) by up to a factor of five. The motion isolation does not cause the STM to vibrate with respect to the SEM, and no difference in SEM resolution was observed between the STM and the regular SEM stage. It does however, allow the STM to rock slightly, particularly when actuating the Y axes. The two middle shock mounts are close together, for packaging reasons, so they are not resistant to lateral forces. This effect is somewhat alleviated by set screws on the edge of the stage, which limit the isolated platform's range of side to side motion to about 25 μm. The isolation mounts consistently return to the same position however, within 200 nm, so in fact the movement is not a serious problem.

The axes are actuated by rotary feedthroughs on the vacuum plate. Drive goes from the feedthrough, via u-joint driven shafts, to reduction gears consisting of a worm and wheel, then to decoupling devices which turn Newport Instruments 80 tpi set screws. The set screws have adjustable thread tension to control backlash. Differential thread actuators were considered in place of worm gears and set screws, but such mechanisms would add mass to the isolated part of the STM. Gear reduction was a compromise between adjustment speed and accuracy. For all the X and Y axes, 30 tooth double thread worms driving 80 tpi set screws, give 21.6 μm per feedthrough turn. This allows a positioning accuracy of approximately 750 nm. The probe Z drive uses a single thread worm to produce 8.8 μm per turn. That yields a positioning accuracy of about 300 nm.[21] The probe can readily be brought to within 200 μm of the surface with the coarse adjustment and then only about 25 turns of the feedthrough need to be made to establish tunneling.

The decoupling devices shown in figure 2.7 have two purposes. Since all set screws move relative to the chassis, the drive shafts have to have some flexibility. The probe's Y-axis set screw for example, moves off-axis in response to movement in the probe's X axis, the sample/probe X-axis and the probe Z-axis. Flexibility could be achieved with U

joints except for the other reason for decoupling: vibration isolation. This arrangement minimizes the isolated mass, allowing the gearboxes to be mounted to the chassis.

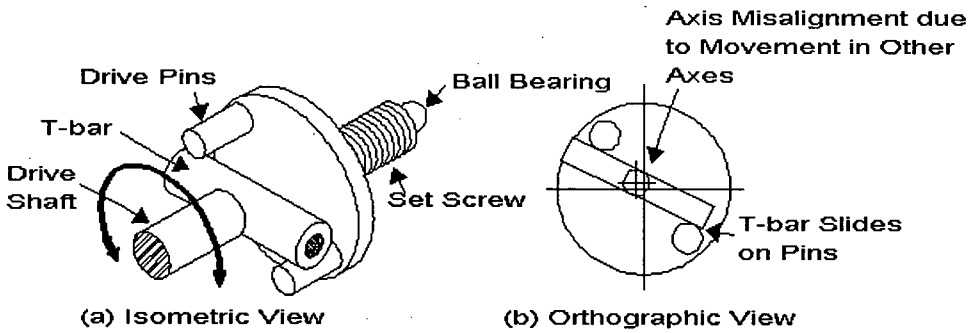


Figure 2.7: Decoupling mechanism

The back plate is mounted on a larger flange which holds the STM at 30°. The only functional change from the tilt is that distances in Y on the SEM screen are all shortened by a factor of cos(30°) or 0.886. The whole image remains focused because the depth of field of the SEM is very good.

## 2.3 (a). Piezotube Configuration

Most modern STM designs have the probe mounted on a single piezotube, whose electrodes are configured to allow movement in three dimensions.[13,15-19] In our initial design, this arrangement was modified to fit in the SEM by installing the tube horizontally and bending the probe 90° to the sample (figure 2.2(b)). The controller was also modified to rearrange the X,Y and Z signals from those shown in figure 2.8(a) to those in figure 2.8(b). It was found that this configuration had several disadvantages. The piezotube deflects about half as much longitudinally as in the bending axis, so this asymmetrical scanning configuration produced highly distorted images. To avoid rewriting the existing control software, the scanning range on the bending axis had to be

reduced by a factor of two, reducing the maximum image size from $(5\mu m)^2$ to $(2\mu m)^2$. In compensation, the Z range was doubled, but this was unnecessary.

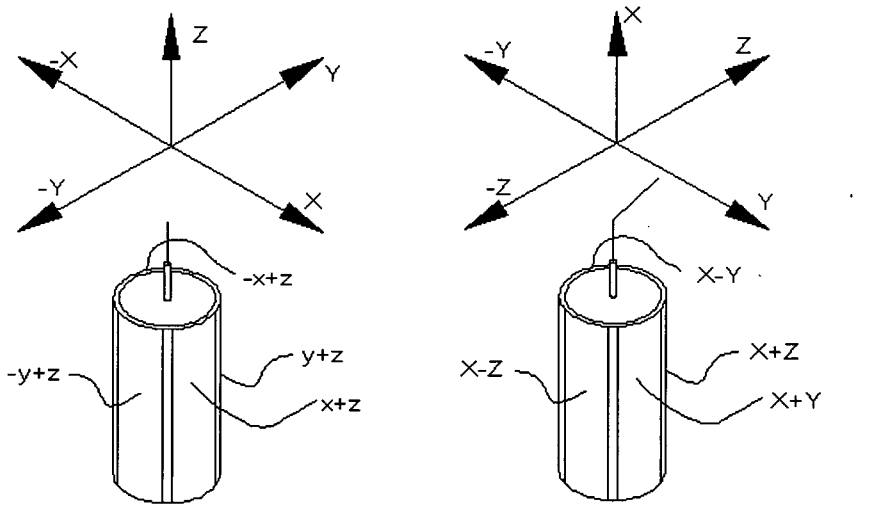


Electrode Signals and Coordinates for On Axis Operation

Electrode Signals and Coordinates for Bent Tip Operation

(a) (b)

Figure 2.8: Comparison of axes and signals for two different scanning geometries

Another problem was bending of the SEM beam. Despite a shielding tube on the probe housing, the X signal, which was sent to all tube electrodes, would cause the SEM's beam to move, giving the appearance of sample movement. The problem was worst when the ac X signal was sent to all electrodes, as in figure 2.8(b). Exchanging the X and slowly ramping Y signals improved the situation, and reduced the distortion,[22] but still held the probe to a small scan range, and made ac calibration measurements impossible.

Within the context of the design which finally evolved, the horizontal tube design was also undesirable as it added mass to the most vibration prone area of the STM. To solve both these problems, the STM was rearranged so the sample was mounted on the tube and the probe was fixed in a hinged bracket as shown in figure 2.4. The advantages of this arrangement are that it is compatible with existing controllers, maintains scanning tube symmetry and lightens the mass on the most vibration sensitive area of the assembly.

It also makes the instrument easier to use because the hinged probe mount makes changing probes and samples much easier.

The only drawback of moving the sample with the piezotube is coupling of the bending to the Z axis if the probe is scanning off center. Figure 2.9 illustrates this situation.

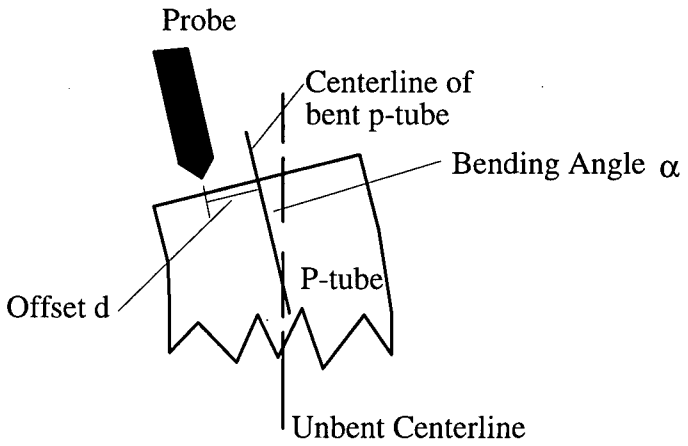


Figure 2.9: Z coupling effect when scanning with stationary probe

If the probe is offset from the piezotube's centerline by a distance d, and the probe is bending at an angle $\alpha$, the coupled movement in Z is $d\sin(\alpha)$. With a 2 μm displacement of the 25 mm tube, and a 4 mm probe offset for example, the coupled vertical movement is 300 nm, which the STM must compensate for. The solution to this problem was to position the STM so the piezotube's centerline was coincident with the SEM beam when all the STM axes were centered. The probe was thus centered on the piezotube when operating in the SEM.

## 2.4 Vibration Analysis

Vibration control was a significant challenge in the design, due to the complexity of the instrument. During development, attempts were made to identify and remove vibrational modes. Three different techniques were employed to measure vibrations. The first was to drive one electrode of the piezotube and measure the output of the other, with

a Stanford Research Systems SR 565 Lock-In Amplifier. This method is appealing in principle because it is not affected by the quality of the tunneling junction. It did not, however, yield satisfactory results. It was impossible to determine repeatably if fluctuations in the output actually corresponded to potential mechanical modes. Modifying the STM by adding weight or removing the set screws did not produce reproducible changes in the spectra. A possible problem was insufficient piezotube drive voltage. The analog output of the Lock-In was 3Vp-p but the piezotube can accept up to 400Vp-p. A resonant frequency of the piezotube was clear however and appeared at 25kHz, far higher than any other modes.

A simpler and more successful method was to measure the response of the piezotube to manual tapping. Output from one piezotube electrode was recorded on a storage oscilloscope and the dominant frequencies were determined manually. A dominant mode at approximately 400Hz was seen. This frequency corresponded with approximate values for the fundamental modes of two control arms. The X control arm, with a estimated fundamental mode at 380Hz was replaced with a much stiffer block, but the problem persisted. The probe Y hinge was then isolated by attaching the whole outer assembly (Seen on the right side of figure 2.4 but at that time including the tube) to a rigid block. The mechanism showed a clear resonance at 400Hz. When the set screw was removed, this mode disappeared so it was concluded that the probe Y control arm was vibrating. A new, stiffer arm was installed and the 400Hz mode rose to 575Hz with much reduced amplitude. Several other small changes to the mechanism also reduced vibration, such as moving the piezotube to the sample stage, stiffening the probe X and Z hinge mounts, and adding clamping ridges to the hinges. Quantifiable data on these changes were not obtained, but a noise reduction in the STM was observed.

After development of the STM was complete, vibration spectra were obtained by observing the feedback signal of the stationary STM with a spectrum analyser.[23] The spectra, which were averaged eight or sixteen times, were output on the analyser's analog

X Y plotting outputs. Those outputs were then sampled by the computer with a program developed for the purpose, and the results plotted.

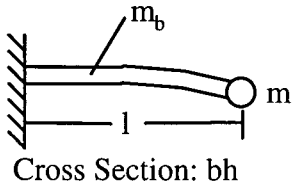


Figure 2.10: Model of a vibrating beam

The vibration frequencies of various different STM components were estimated. These components were modeled as beams, fixed at one end as shown in figure 2.10. Frequencies were estimated using the following formula,[24] and are shown in table 2.4.

$$\omega_n = \sqrt{\frac{3EI}{(m+0.23m_b)l^3}} \qquad \text{where} \qquad I = \frac{bh^3}{12}$$

$E$ = Young's Modulus ($7 \times 10^{10}$ Pa)
$m_b$ = mass of beam
$m$ = load a end on beam

Table 2.4: Table of estimated frequencies for vibrational modes STM components. Upper and lower bounds come from different estimates of the length or moment of inertia of the various components.

| STM Part | Upper Estimate (Hz) | Lower Estimate (Hz) | Comments |
|---|---|---|---|
| Probe Y Control Arm | 664 | 403 | New Configuration with lighter probe mount |
| Sample X Control Arm | 1,585 | na | New rigid block |
| Sample Y Control Arm | 2,130 | na | |
| Chassis* | 125 | 77 | Gearbox mass averaged along length |
| with 24.3 g added | 122 | 75 | |
| with 230.2 g added | 94 | 59 | |
| with 283.2 g added | 90 | 56 | |
| Chassis (2nd Harmonic) | 500 | 308 | |
| Sample Y Gearbox | 25,000 | na | Assuming all vibration comes from the mounts |

* The chassis was modeled as both a solid rectangle, with the added mass of the STM and gearboxes, averaged along its length, and as a C channel because of the volume removed for X axis movement.

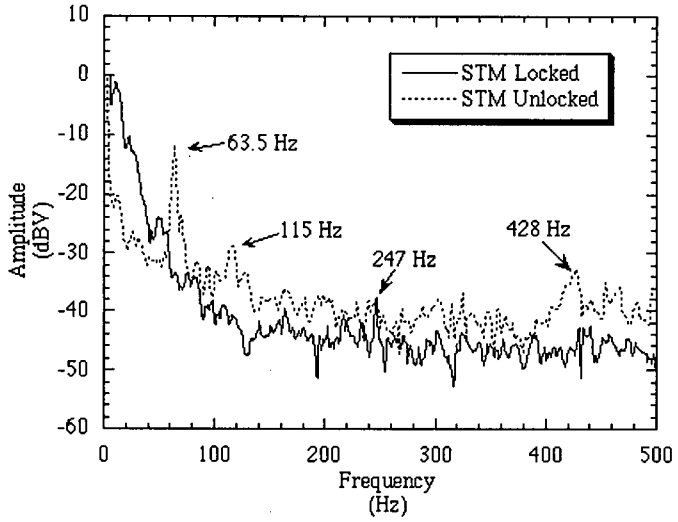


Figure 2.11(a) Vibration spectra of the STM operating in the SEM with the mechanical pumps off.

Figures 2.11 and 2.12 show plots of the vibration spectra of the STM in different configurations. Most of the modes which appear consistently were below 100 Hz, lower than any estimated modes, save the fundamental mode of the chassis. At higher frequencies, between 200 and 500 Hz, changes in the tunneling junction caused modes to appear inconsistently. Above 500 Hz, no significant modes were seen. It was not possible to positively identify any modes with a particular component of the mechanism.

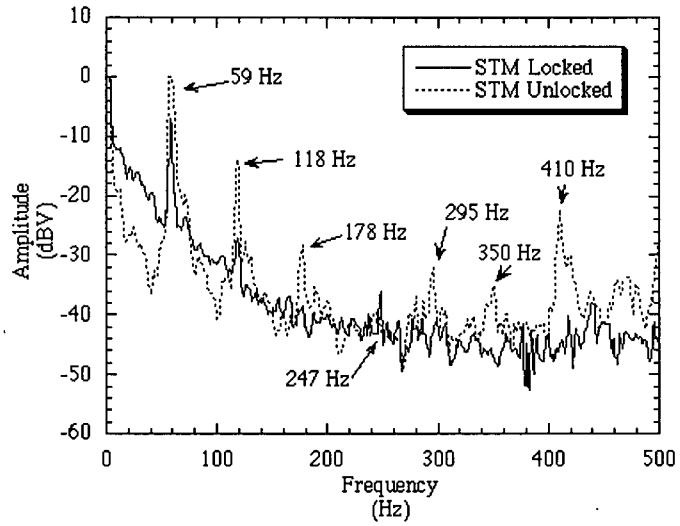


Figure 2.11(b) Vibration spectra of the STM operating in the SEM with the mechanical pumps on.

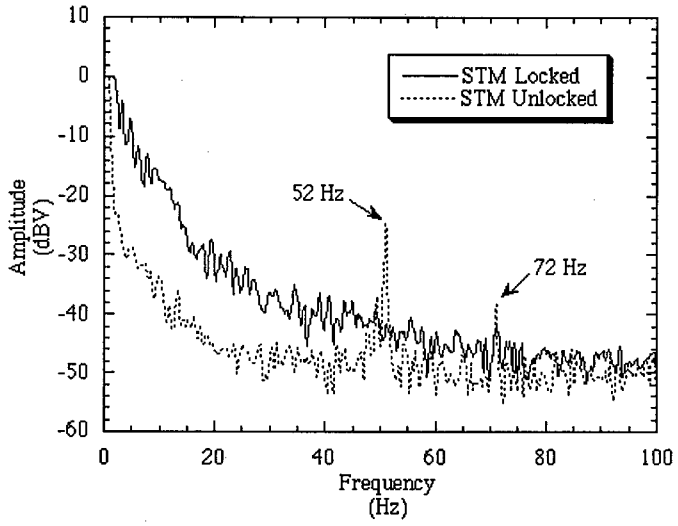


Figure 2.12(a) Vibration spectra of the STM operating in air with the STM stand locked and unlocked.

Figures 2.11(a) and (b) show the spectra of the STM, operating in the SEM with the SEM's pneumatic stage (ram) lock and adjacent mechanical pumps on and off. With the ram lock off, the chassis was free to vibrate in its fundamental mode. With the mechanical pumps on, modes were seen which are approximately multiples of 60 Hz (The difference may be due to errors in the sampling program). They were reduced, but did not entirely disappear, when the chassis was locked. Modes in the 400 Hz range were not consistent, and it is believed that these originate from the tunneling junction. With the chassis locked and the pumps on or off, a common mode appeared at 247 Hz.

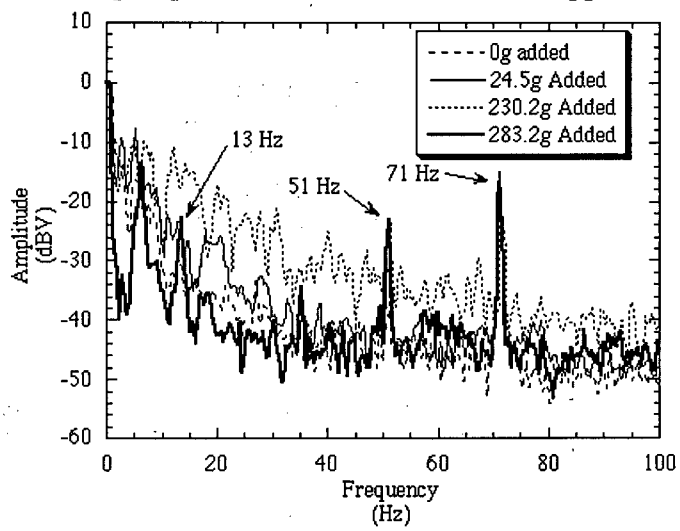


Figure 2.12(b) Vibration spectra of the STM operating in air with weight added to the end of the chassis. The STM stand is unlocked.

Figure 2.12(a) shows modes at 52 and 72 Hz, which consistently appeared when the STM was operating in air with the chassis unlocked. If these modes were due to chassis vibration, they should change in response to mass added to the free end of the chassis, as shown in table 2.4. They should likewise change in response to the removal of gearboxes. In neither case did they change frequency. When the STM was separated from the chassis on foam pads however, these modes disappeared. A possibility is that the 52 and 72 Hz modes originate in the building. Because they did not appear in the mechanically isolated SEM however, this question was not persued.

In conclusion, this method of vibration analysis was not ideal for analysing the STM's vibration spectrum. There was too much dependence on the quality of the tunneling junction and external modes seemed to dominate the spectra. This might however, be an excellent method of studying the effect of changes in the tunneling junction, including integrator values and current setpoints. The lowest noise figure recorded in the feedback signal was 10 mV, equivalent to 4Å vertically.

## 2.5. Range Calibration

The STM's drive electronics and software assume a linear relationship between voltage and displacement.[24] In fact the piezotube's behavior is more complicated as in particular, deflection is dependent on signal frequency. The ability to view the STM with the SEM allowed novel methods of range measurement which could be compared with previous results.

### 2.5 (a). Lateral Calibration

T. Pinnington calibrated an air STM with a similar piezoelecric scanning element as the instrument described here, using two different methods. Individual carbon atoms were

resolved on graphite, and knowing the interatomic spacing from x-ray measurements,[25] the deflection factor was found to be 12 nm/V. The same measurement was done at large scan ranges using a TiN sample with via holes of known size and spacing.[26] At scan ranges of 2x2μm, deflections were found to be 12 nm/Volt in X and 19 nm/Volt in Y. The difference is due to hysteresis effects in the tube. The scanner deflects considerably more under the near dc bias of the Y ramp than the ac X signal.

With the combination SEM/STM, the scan range could be measured directly with the length scale on the SEM screen. This is the set of ten lines at the bottom right corner of all SEM images. An identifiable point on the sample was selected and its movement observed relative to the lines. For the Y movement, measurements were made with the SEM's image rotation control at 90°, and then corrected for the 30° tilt of the STM.

To measure dc deflection, the STM's offset controls were ramped slowly across their whole range. The results are plotted in figure 2.13. Hysteresis, characteristic of these piezotubes, is evident along with the fact that the range is symmetric in X and Y.

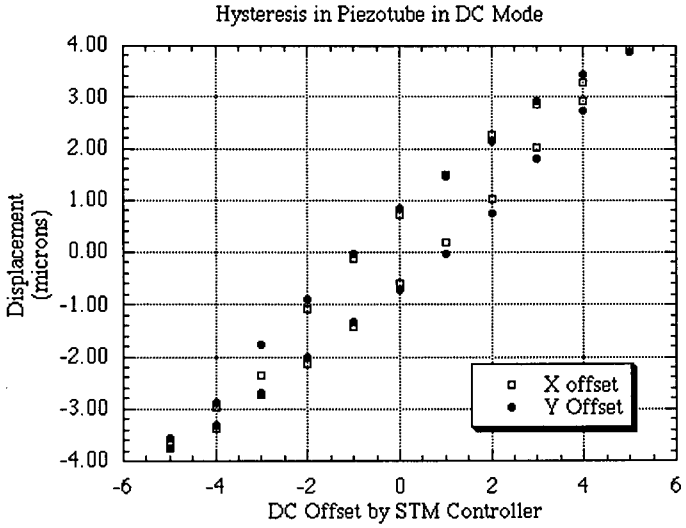


Figure 2.13: dc offset measurements of piezotube range

The STM's range while scanning was measured in two ways. The first was to observe the displacement of a point on the sample directly with the SEM, as above. At a constant scan rate of 0.66 Hz, the actual X scan range was measured at different

controller ranges. The graph in figure 2.14 shows that the range in X is approximately 500 nm/unit of XY scan range or 12.5 nm/V, which agrees well with Pinnington's value. Note also that the measured maximum of 4.5 μm is less than the 7 μm range measured in the dc case.

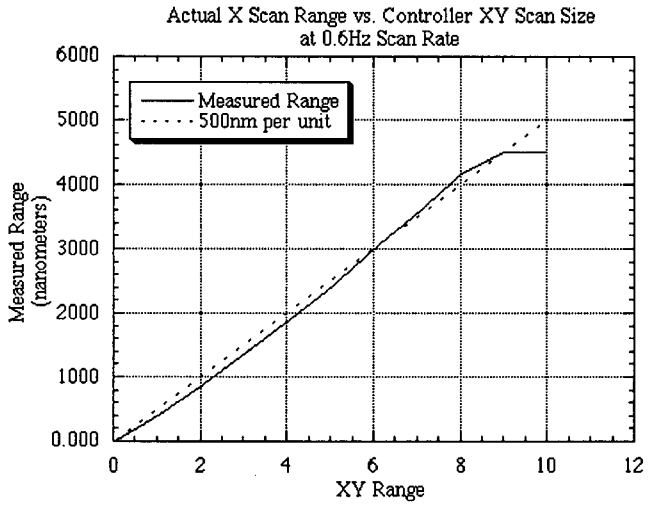


Figure 2.14: STM X range as measured in SEM

A second, novel method, involved scanning a region of passivated silicon <111> at high negative polarity, and measuring the dimensions of the area left depassivated by the scan, as in the nanolithography experiments discussed in chapter 7. This method had the advantage of being able to accurately measure both the X and Y ranges, and the change in scan area at different rates.

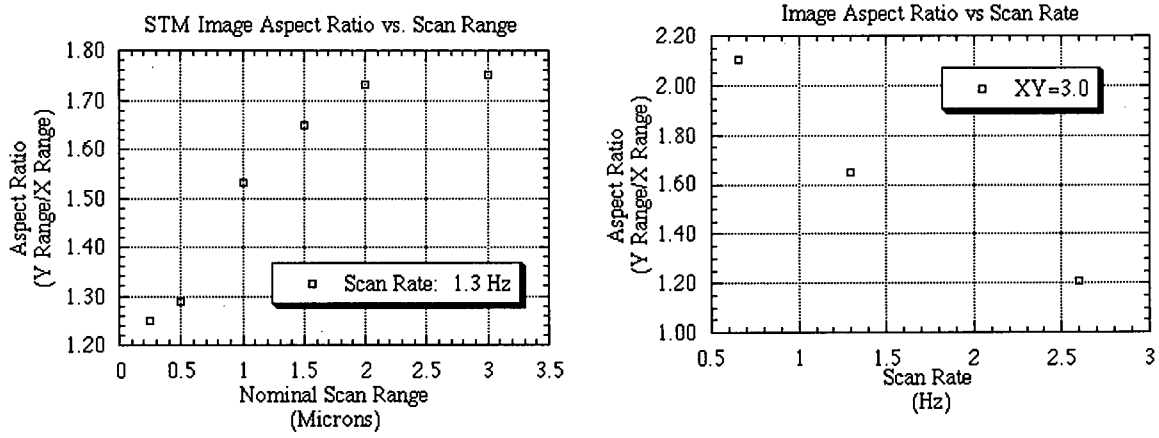


(a) (b)

Figure 2.15: Image aspect ratios vs. scan range and scan rate.

Two observations were made. The first was that within the normal range of STM operation, scan speed did not affect the X range. Both scan rate and range did, however, affect the Y range. Figure 2.15(a) shows the aspect ratio rising as the XY range is increased at a constant scan rate. Figure 2.15(b) shows the drop in aspect ratio as the scan rate is increased at a fixed range. The change in aspect ratio of the piezotube is due to hysteresis.[27] The piezotube will deflect more when the voltage is changed more slowly, or over a larger range. Since the measured X range was not observed to change at different scan rates, the change in aspect ratio is due to a change in the Y range. Figure 2.15(b) suggests that the change in tube behaviour occurs between 200 and 800 seconds for a full scan (based on a 400 line image). The time scale may however couple to the scan range. Further investigations could be easily carried out using this method.

**2.5 (b). Vertical Calibration**

The Z range of the air STM was measured by T. Pinnington with an optical range finder.[28] A calibration factor of 50Å/V was found. The feedback monitor from the STM controller has a range of +/- 15 V, so the signal on the oscilloscope actually represents 650 Å/V. With the SEM, range could be measured directly, as in the lateral case. Since the STM is tilted at 30° in the Y direction, a piezotube movement L in Z will appear to the SEM as Lsin(30°) or 0.5L in Y. With the probe away from the surface and the feedback loop off, a 1Hz, 10 Vp-p signal was applied to all four piezotube electrodes. The resulting Z movement of the sample was measured and found to be 40±10 Å/V. To measure the tube response at large voltages, a tunneling junction was established at the zero dc point, and the tip retract was turned on. The resulting movement was measured and a calibration figure of 50±2.5 nm/V was obtained. These results agree well with the figure obtained by Pinnington. The problem of Z calibration at atomic scales still exists however since such movements would be impossible to measure with the SEM.

## 3. Probe Fabrication

It has been shown that for air operation, mechanically sheared platinum iridium (PtIr) probes are generally as effective as PtIr probes produced by electrochemical etching.[24] Although the STM discussed here is effectively an air instrument, in that no in-situ sample or probe preparation is possible, cleaved probes are actually not satisfactory. To facilitate accurate positioning, the probe must be macroscopically slender so that the area of sample immediately surrounding the tunneling junction can be viewed by the SEM. While cleaved tips are microscopically sharp, the bulk of the wire shields the tunneling junction from view. A good example of the advantages of a sharp probe is shown in figure 3.3, where the surface structure around the scanning region is clearly visible. End radii smaller than the STM's offset range are desirable.

Forward and reverse etching techniques were investigated. Instead of obtaining the probe from a short piece of wire dropping off a longer piece, as in forward etching, reverse etching creates the tip on the end of the long piece of wire, which must then be cut into a probe. Forward etching is also often referred to as the drop off technique. Experiments were done with three different probe materials, all in the form of 250μm wire: gold, platinum 10% iridium, and tungsten.

### 3.1 Reverse Etching.

Reverse etching,[29] shown in figure 3.1 was used with tungsten wire in 2M NaOH solution. The wire is shrouded in Teflon tubing with the last two or three millimeters exposed and pointing upwards. A 5Vac signal is applied to the wire and stainless steel electrode. As bubbles form from etching the exposed wire, they float upward, remaining close to the wire due to surface tension. This causes the probe to form a conical figure with a sharp apex. The etching process must be monitored so that etching can be halted

when the probe has the correct shape. If not, the probe will continue to etch until all the exposed Tungsten is gone. This process was found to produce very sharp probes, with end radii from 500 nm down to 100 nm. Radii as low as 1 nm have been reported.[29] After etching, probes were rinsed in DI water, and blown dry with nitrogen gas.

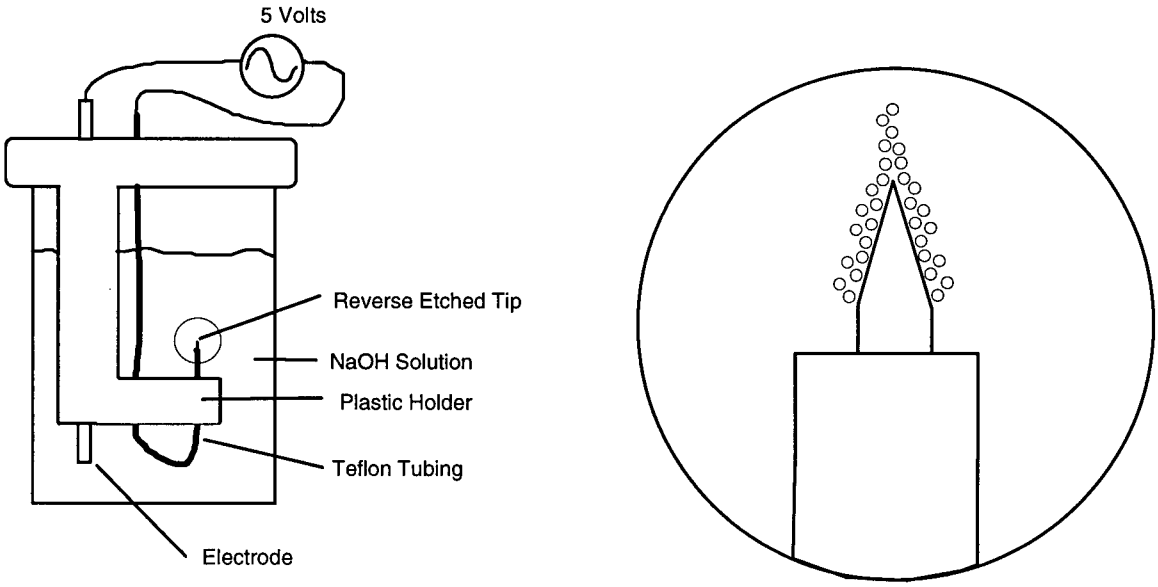


Figure 3.1: Reverse etching

### 3.2 Forward Etching.

The forward etch, or drop off method,[30,31] involves encasing the wire in Teflon tubing but leaving 1-2mm exposed, 15 mm from the end of the wire. The setup is shown in figure 3.2. The wire is then held in the solution with the exposed section at the surface. This is done to prevent large bubbles forming around the etched region, and bringing the etching process to a halt. 5-10Vac is applied between the wire and a stainless steel electrode. The etching proceeds until the wire becomes so thin that the short section drops off and the etching stops. The short section of wire then forms the probe. It is rinsed in DI water in an ultrasonic cleaner for two to five minutes and blown dry with nitrogen gas before use.

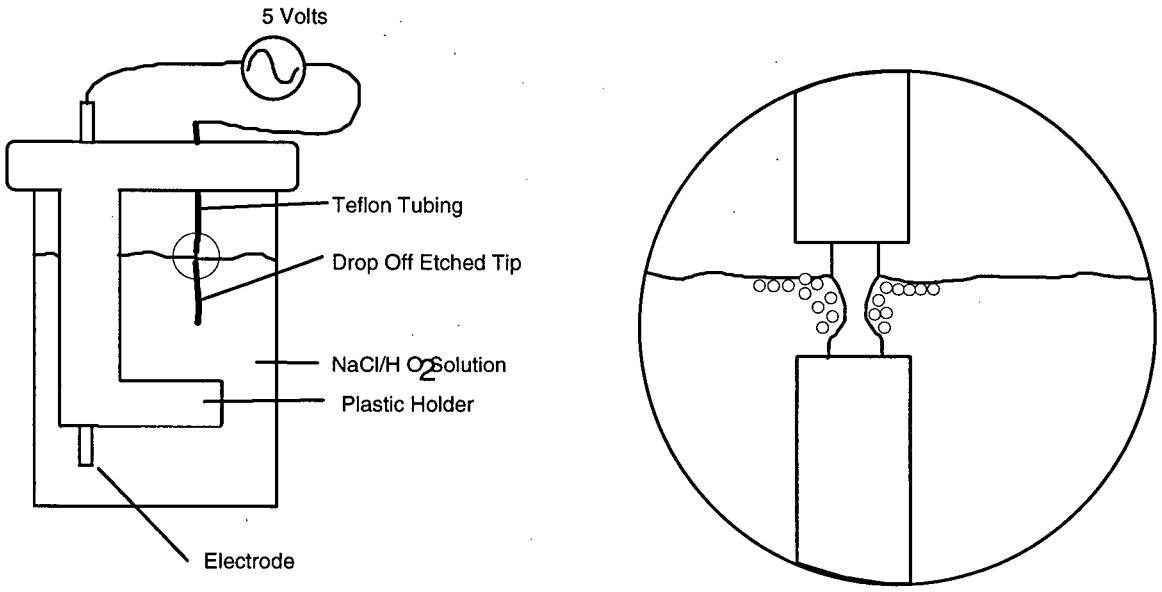


Figure 3.2 Forward etching

### 3.3 Comparison of Techniques

With the drop off method, end radii were generally larger than those produced by reverse etching. Radii between 1 and 5 μm were typical, although the probe in figure 3.3 has an end radius of about 100nm. It was observed that tungsten probes were microscopically much smoother than PtIr. Etched PtIr probes such as the one shown in figure 3.3, have rough surfaces with many ridges and points. Tunneling may take place from such structures, which can be at least as sharp as the SEM's resolution limit of 2 nm. The advantage of reverse etching in producing sharper probes is therefore negated. The drop off technique has another advantage over reverse etching in that it does not require monitoring; the etching process stops automatically when the probe falls. This conveniently allows the user do other tasks during probe fabrication, saving considerable time.

The key criterion for judging probe materials and etching techniques is image quality, not end radius. On that basis, the forward etched PtIr probes were superior to the sharper tungsten probes. Tungsten has been found to perform better in UHV where probes can be baked prior to use.[32] PtIr probes also suffered less degradation from crashing, which

considerably enhanced practicality. The microscopic sharpness of the PtIr probes could explain this phenomenon. Gold probes were used only for field evaporation experiments. While gold probes produced images of similar quality to PtIr, etching required conc. HCl, which complicated process handling.[33] Gold probes also formed very high aspect ratios, like that shown in figure 3.4, which is undesirable.

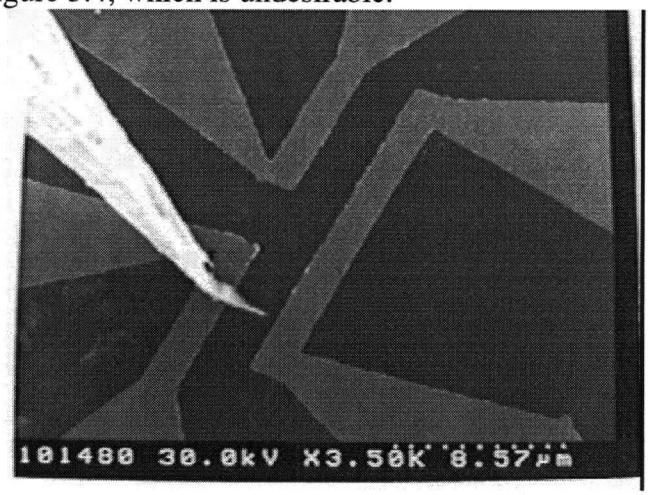


Figure 3.3 SEM image of a PtIr probe forward etched in NaCl


Figure 3.4. SEM image of a gold probe forward etched in HCl

Probes with very high aspect ratio tips were found to have two practical disadvantages. The first was difficulty in estimating the location of the end of the probe with the naked eye. That made coarse probe positioning much more difficult. Very thin probes were also not resistant to crashing and surface contact while scanning. Either

event could bend the probe to the point where it was unusable. To avoid this problem in reverse etching, the gap in the Teflon tubing was kept under 2 mm. The aspect ratio of gold probes did not appear affected by this gap however. The weight of the 15 mm section was enough to draw the wire out when the etch site got sufficiently narrow. Unfortunately, byproducts of both the PtIr/NaCl and Au/HCl, reactions are opaque, so it was difficult to observe the exposed wire during etching.

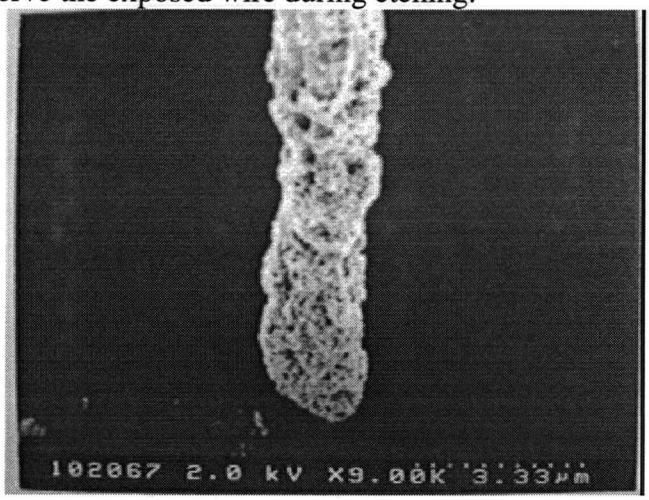


Figure 3.5. Encrustation on a probe left overnight in solution

The cleaning process for PtIr probes was found to be satisfactory provided the probe was not allowed to sit in solution for too long. Figure 3.5 shows a PtIr probe left in solution for approximately 10 hours. Although it was washed, it maintained an encrustation of foreign material, either crystallized salt or reaction products. Generally, probes were fabricated immediately before use.

## 4. STM Alignment and Simultaneous Imaging

A major advantage of a combined SEM/STM over an STM operating alone, is the ability to find specific structures with the SEM and image them with the STM. This capability is demonstrated here. While these examples show the expected superior lateral and vertical resolution of the STM, they also demonstrate limitations of the STM. Structures with large vertical topography, insulating regions or wafers with imperfect cleaves can all limit the STM's ability to produce accurate images. In this chapter and the following chapter, the SEM's ability to determine whether the STM is giving a true picture of the surface is discussed.

### 4.1 STM Alignment

Aligning the STM with a region of interest on a sample was an iterative process. First, the probe and sample were loaded on the STM and manually positioned to ensure that the STM was able to bring both the sample's region of interest and probe under the SEM beam. Once in vacuum, the SEM was used to bring the probe to within at least 100μm of the target region. The probe was then lowered to within a few microns of the surface. This was accomplished by checking the difference in focus point between the probe and sample, until they were within a fraction of a turn of the fine focus adjustment. The probe was then moved to within about five microns of the target region and lowered until tunneling was established. The probe could then be moved a few microns with the tip either retracted or raised half a turn of the Z feedthrough. The tip was retracted farther for longer movements. Since probes typically have end radii on the order of .5 to 5μm, final alignment had to be done by trial and error. Fine adjustment of the probe's position was done with the XY offset controls on the STM controller. The smaller the STM scan, the more the XY offset controls could be used to further position the probe. Large scans

or large offsets could result in the STM controller overloading, leading to distorted scanning.

## 4.2 Imaging of TiN via holes

The first attempts at simultaneous imaging were made with a sample with arrays of via holes in TiN, fabricated by photolithography.[26] These are holes with conducting sides which allow current to flow from one layer to another in a semiconductor device. Figure 4.1 shows SEM images of the surface at different magnifications. In this case, the tip radius was smaller than the via holes' radii, so it was possible to image specific holes. Figure 4.2 is an STM image of the same surface. It displays considerably greater surface topography than the SEM image, in particular showing ridges running along the surface between the holes. Despite being quite sharp, the STM could not reach the bottom of the holes without part of the probe contacting the edge and producing a false image. This effect is examined in greater detail in Chapter 5.

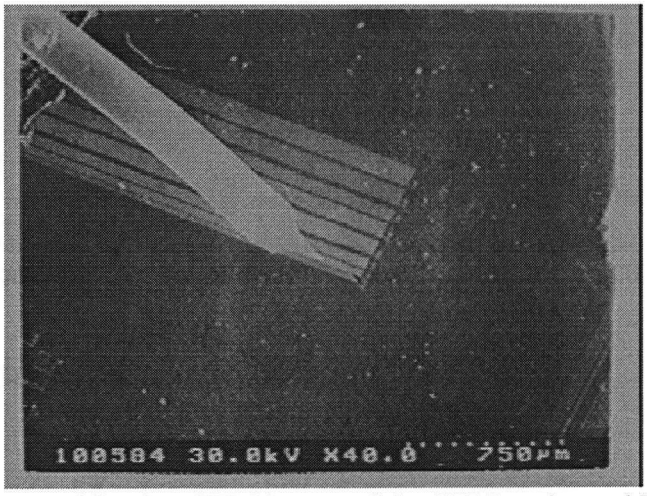


Figure 4.1(a): Low magnification SEM image of the STM probe and TiN via holes.

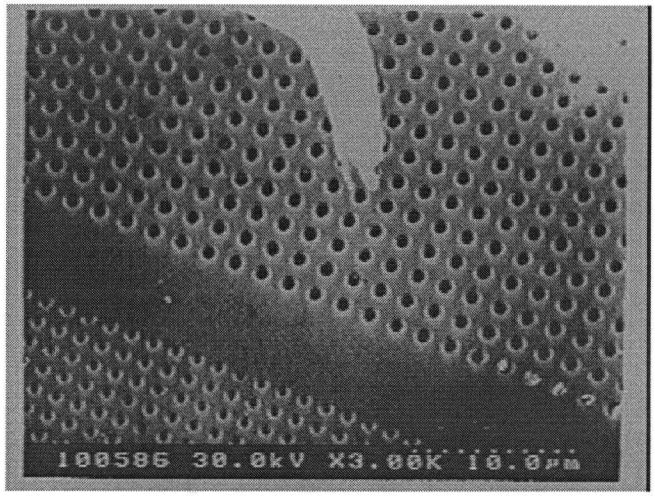


Fig 4.1(b): Close up of STM probe on TiN via holes.

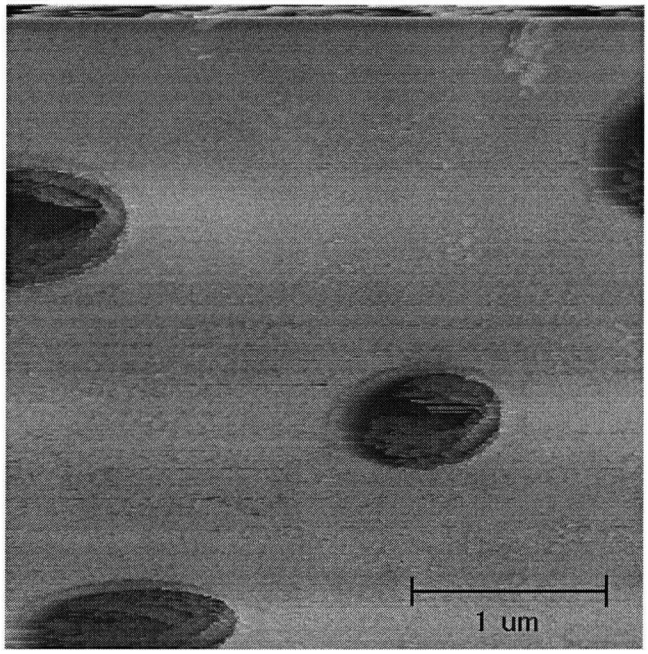


Figure 4.2: STM image of TiN via holes. V = +1V, i=1na, XY = 8.0

### 4.3 Imaging of E-Beam Calibration Pits

Unlike the SEM, the STM can make quantitative measurements of vertical topography. Its image is formed by the STM controller's feedback loop, which contains information about the relative height of features. The only way to measure the height of surface structures with the SEM is to cleave a sample and view the structures edge on.

An example of STM topography measurement is shown below. Figure 4.3 and 4.4 show SEM and STM images of pits in GaAs, made by e-beam lithography.[34] Arrays of these pits were made to investigate the relationship between beam dose and etch depth, so it was necessary to measure the depth of the pits. The sample was coated with 50Å of chrome and 150Å of Gold. In this case the probe was not microscopically very sharp, but the pits were sufficiently shallow that their depth could be measured without the topographically induced distortion effects seen in figure 4.2.

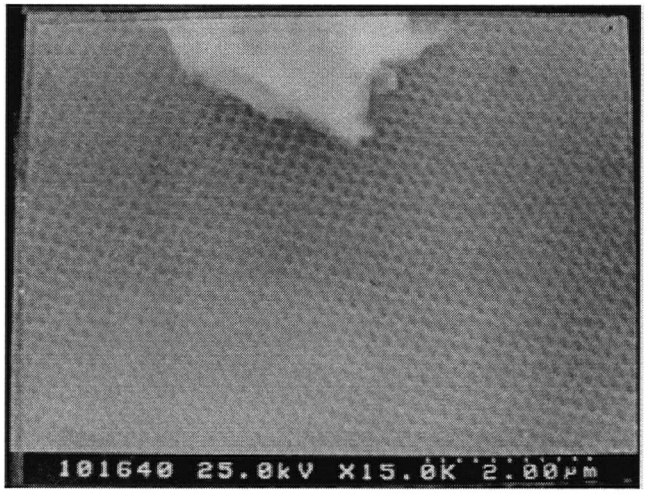


Fig 4.3: SEM image of e-beam fabricated pits. The probe is seen at the top of the image.

Comparing figures 4.3 and 4.4 allows the lateral distortion in the STM image to be investigated. The SEM micrograph shows that the holes are indeed round and evenly spaced, allowing for the 30° sample tilt. The STM image however, shows twice as many holes vertically as horizontally. The resulting image aspect ratio is approximately 2, which agrees with the data in figure 2.4. It can also be seen though, that the movement in Y is not linear. The top row of pits is less distorted than the following rows, and the most distorted rows are at the bottom. Such movement is expected from the hysteresis plot in Figure 2.12, where the slope of the curves increase towards the end of the displacement. This distortion is a major problem for imaging at large scales and low speeds. Commercial STM vendors, use either a software model of the tube in the scan wave

generator,[35] or optical feedback of the scanner position[36] to compensate for distortion. If this is not done, the STM's usefulness as a tool for large scale imaging is limited.

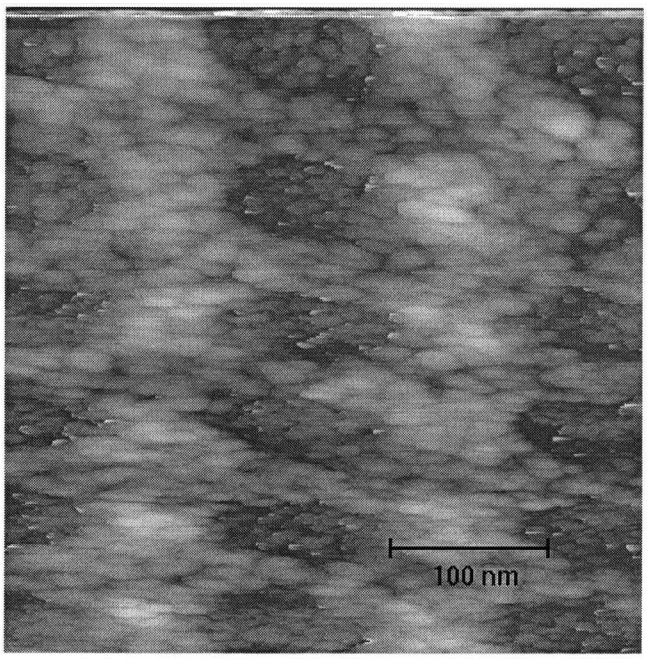


Figure 4.4: STM image of the same pits as in Figure 4.3. V = 1V, i = 1nA, Scan Rate = 0.66 Hz, XY = 1.0. The pits are the dark ellipses. The "cloud top" surface is characteristic of evaporated gold.

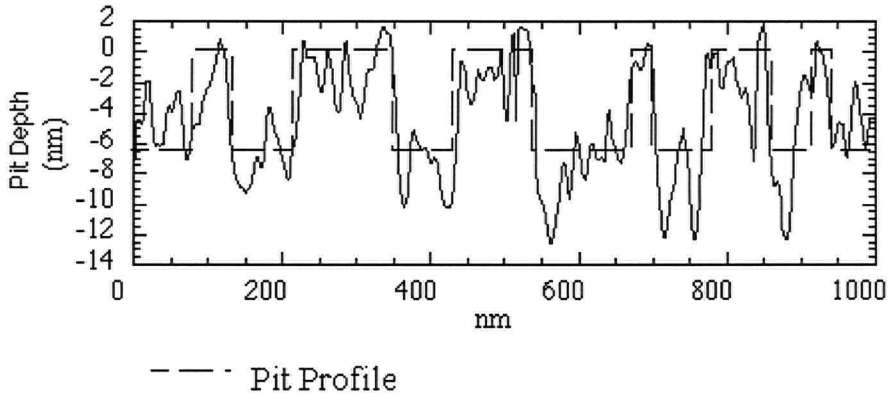


Figure 4.5: Topography of the surface, measured down the center of the image. Average pit depth is 10 nm.

## 4.4. Imaging a Specific Microstructure.

The previous examples show imaging of microstructures where the required alignment accuracy was several microns, Each array of pits in figure 4.4 was 10μm square. The TiN via holes have actually been imaged by STM in air using an optical microscope for alignment. In these cases, precisely which holes or pits were imaged was not of interest. Figure 4.6 though, shows a specific microstructure, a boundary marker between pit arrays. In this case, it was necessary to position the probe with an accuracy of about 0.5μm in X and Y.

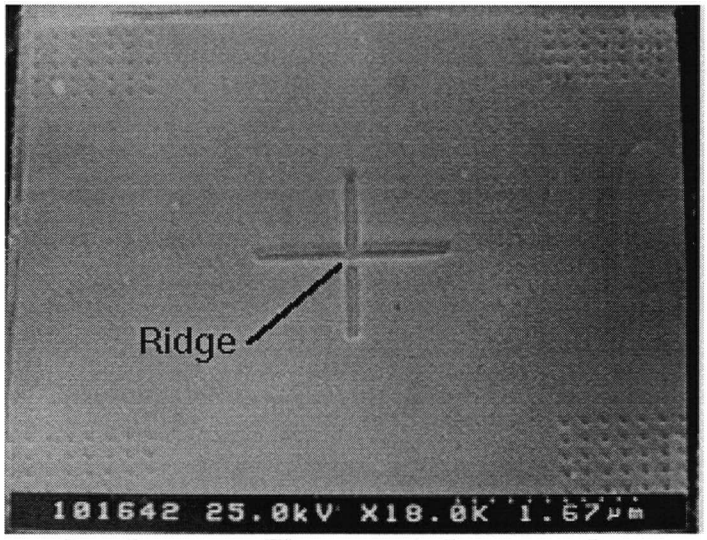


Fig 4.6: SEM of a registration cross. Pit arrays can be seen at the corners of the image.

Figure 4.7 (a) to (c) show successively higher magnification images of the same region as figure 4.6. Once again, the STM has superior vertical resolution, but has trouble imaging the deep trench of the cross. Figure 4.6 for example, shows a small ridge bisecting the vertical axis of the cross, an artifact of the e-beam writing process. This ridge does not show up clearly in figure 4.7(a) or (b). This is likely due to the finite tip radius of the STM, which is discussed in greater detail in section 5.3(b). Figure 4.7(b) also shows raised areas around the center of the cross which do not appear in the SEM image.

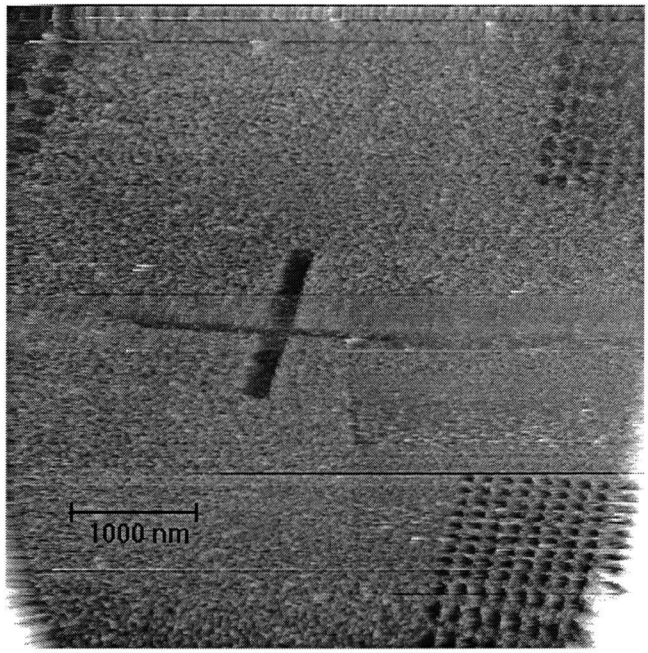


Figure 4.7(a): STM image of the same registration cross. V = 1.0V, i=1nA, XY = 9.0. The white areas on the lower corners are due to the scanner being driven close to the surface, because at extreme lateral range, vertical range is reduced. The sample is tilted slightly down towards the top of the image.

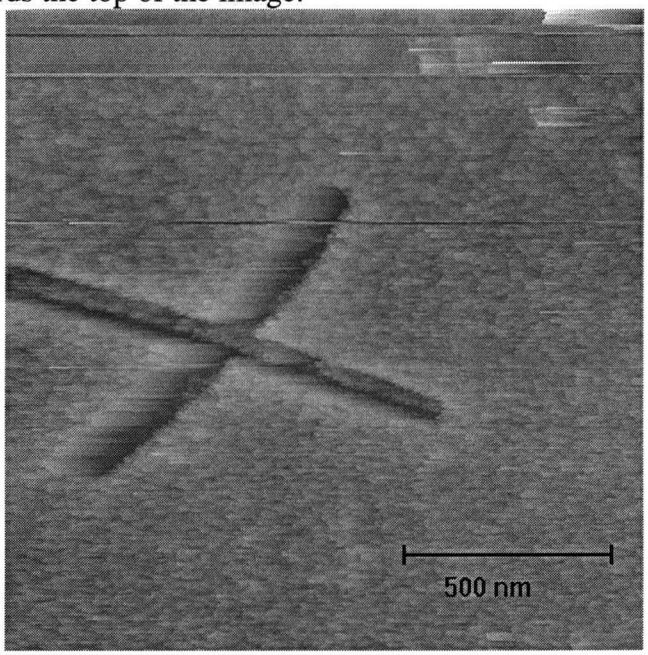


Figure 4.7 (b): Higher magnification STM image of the same cross. V=1V, i=1 nA, XY=3.0 . Note the raised regions around the center of the cross, which do not appear in the SEM image. These are likely due to the STM controller overcompensating for the trench.

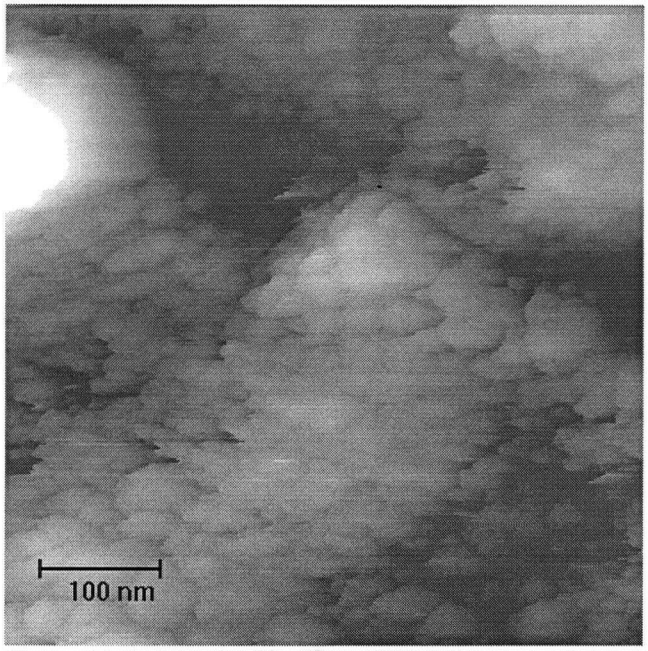


Figure 4.7(c): Even higher magnification STM image of the center of the cross. V=1V, i=1nA, XY=0.5

## 4.5 Imaging of a long gate MOSFET.

Imaging integrated circuit cross sections is another application which for which the combined instrument is well suited. The STM can for example, give some insight into the electrical properties of the different elements in a device. SEM and STM images of a "SEMstrip" are shown below.[26] These are very long MOSFETs, which have been fabricated for easy cleaving and viewing by SEM. Figures 4.8(a), and (b) show views of part of the structure with several MOSFETs side by side. The STM image in figure 4.9 is of the region shown in the square in figure 4.8(b). Neither SEM image shows any evidence of the doped source or drain regions on either side of the long polysilicon gate structure. The Si (100) wafer was passivated for 30 s in buffered HF, rinsed and blown dry.

This structure proved difficult to image with the STM because the devices are buried under layers of $SiO_2$. Any contact with these layers would cause tip-surface contact and imaging would be brought to a halt. In this crude way, the STM was used to determine

which parts of the structure were conducting and which were insulating. Figure 4.9 shows the gate region of the MOSFET. The substrate is to the left. The p doped gate area is at center, with a heavily doped polysilicon layer to the right. To the right of the image is a tungsten layer and then the first layer of $SiO_2$, which the STM was unable to image.

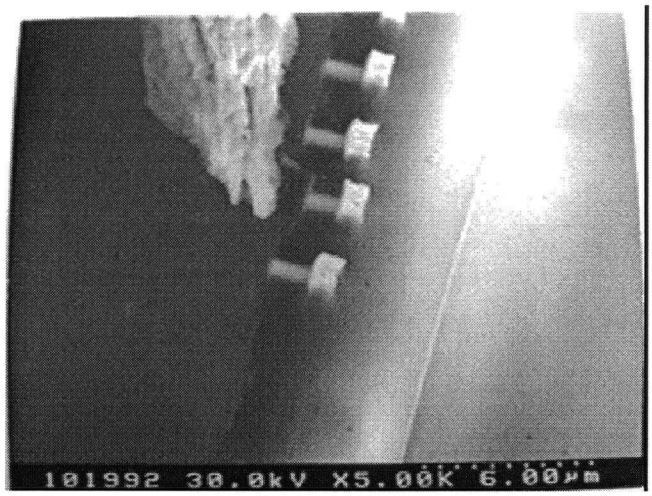


Figure 4.8(a) SEM image of the STM probe over the FET structure. The probe is positioned over the last MOSFET in Set 4D of the sample

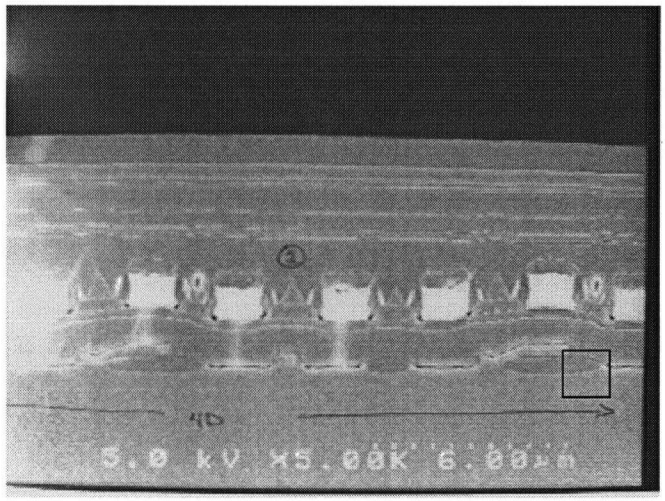


Figure 4.8(b): NorTel SEM image of the same structure showing the location of the STM image in figure 4.10. It is marked by the black square at lower right.

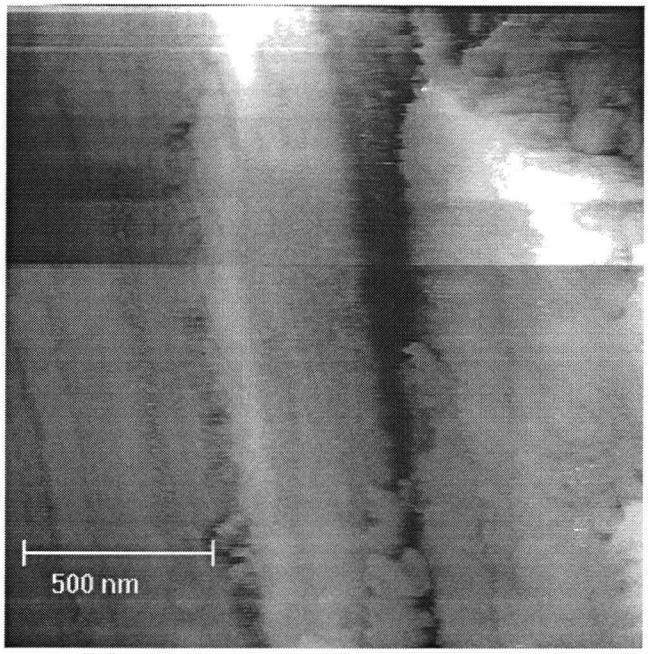


Figure 4.9: STM image of the region shown above. V = +4V, I = 0.2 nA, XY = 3.0. This image is oriented the same way as figures 4.8(a). It is rotated 90° and mirror reversed from figure 4.8(c)

Preliminary studies were made of MBE grown GaAs epilayers. While results were not outstanding, this was thought to be due to poor probe quality or passivation. The combined SEM/STM itself performed extremely well in rapidly aligning the probe over the epilayers. The time required to successfully position the probe over the structure was on the order of minutes. For a conventional STM, where probe alignment must be done by trial and error, this process can take hours.[37]

The combined instrument's advantage in evaluating cleaves and positioning the probe was demonstrated in attempts to image the MOCVD grown GaAs/AlAs structure shown in figures 5.14 and 5.15.[38] An attempt was made to view this monolayer by UHV STM but no successful images of the structure were obtained. Subsequent SEM observations of the sample revealed a poor cleave, which was thought to be the reason images were not obtained.[32] Unfortunately it was impossible to evaluate the quality of the cleave in UHV because of the lack of an in-situ SEM. As a result, approximately twelve futile hours were spent trying to image that sample.[39] With the combined instrument, an appropriate sample location was found and imaged within 20 minutes of the SEM being evacuated.

## 5. Interaction of the SEM and STM.

A major question during the development of the integrated SEM/STM was what, if any, interaction would there be between the two instruments, and would simultaneous imaging be possible. In fact, other than contamination, discussed in Chapter 6, very little interaction was found between the two instruments, and what little there was did not affect operation. It was found however, that the SEM was of considerable help in determining the causes of poor STM imaging.

### 5.1 Effect of the SEM on the STM

The most serious potential problem was whether the SEM's beam current would interfere with the tunneling process. If the beam current from the SEM was similar in magnitude to the STM's current setpoint, it might seriously interfere with STM operation. This has been reported as a problem[5], and in some cases, beam currents have had to be limited to allow the STM to operate.[9] In fact, the operating beam current of the S-4100 SEM was approximately 15 pA,[40] at least an order of magnitude smaller than the STM's current setpoint, which ranged from 0.15 nA for Si to 5 nA for graphite. For that reason, there was no difficulty in imaging simultaneously at all times.

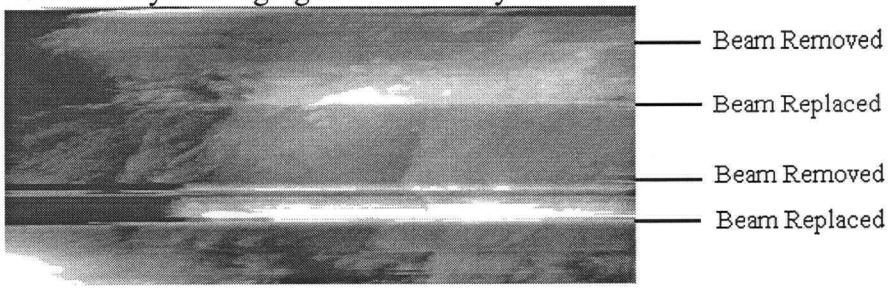


Figure 5.1: GaAs/AlGaAs heterostructure showing how imaging became less stable when the SEM magnification was reduced and the beam was no longer concentrated on the epilayers. Stability returned when the beam was again concentrated on the structure. SEM beam at 30kV. STM imaging conditions were: V = +4V, i = 0.15 nA.

Interaction was found in one instance, when imaging an MBE grown GaAs/AlGaAs heterostructure[41] shown in figure 5.1. It was found that when the SEM beam was applied

continuously to the epilayers, by SEM imaging at high magnification on the structure, STM imaging was stable. When the beam was removed from the region by reducing the magnification, imaging became unstable.

An explanation for this may lie in the effect of the electron beam on suface states. Heike et al observed $SiO_2$ on silicon using Hitachi's V-3000 SEM/STM.[42] The SEM was used to irradiate the sample with electrons to allow tunneling. They observed a decrease in the bandgap at the surface, which may be due to an increased density of states. The beam current in our case was too small to affect the STM, but band bending might have liberated more electrons from the surface, allowing the positively charged probe to maintain its current setpoint from farther away. Changes in vertical topography would be consequently smoothed out, as observed. When the beam was removed, the probe would then move closer to the surface, amplifying changes in topography. In this case the image didn't become darker when the probe moved closer to the sample because a high pass filter was applied to the feedback signal.

### 5.2 Effect of STM on the SEM

The STM was found to have two mild effects on the SEM. The first of these only appeared in the original configuration, where the probe was mounted on the piezotube (figure 2.2(b)). In this case, the high voltage signals to the piezotube's electrodes caused the SEM beam to bend. When the STM was scanning. the entire SEM image would oscillate. That made it impossible to precisely determine the location or range of the STM scan. When the piezotube was moved under the sample, the beam bending effect disappeared.

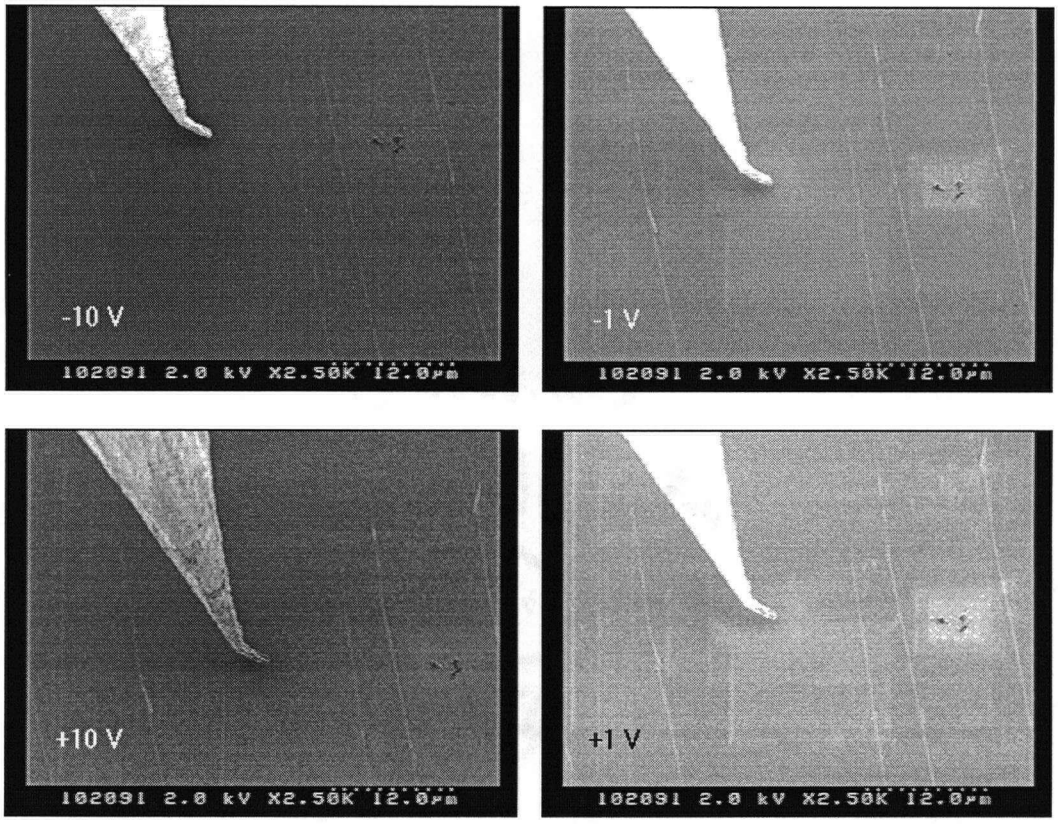


Figure 5.2: SEM images of the probe and sample at different probe voltages. The probe voltage is shown at lower left. The SEM's imaging conditions were fixed.

The other effect the STM had on the SEM, was to change its image contrast, brightness, and position depending on probe voltage. Figure 5.2 shows a series of four images of the same region of passivated Si (111) with the probe at different voltage setpoints. The probe is retracted, but images were unaffected by whether or not the instrument was tunneling. The SEM image brightness, contrast, and position controls were held constant while these images were recorded. One observation is that the image was shifted about 10µm from -10 to +10 Volts. Fortunately this is a dc effect; the STM probe voltage is not generally adjusted during imaging. The only problem stemming from this effect is the image would occasionally move out of the SEM's viewing range with voltage changes. The second observation is that the image, particularly the sample, is much brighter at low voltages. The SEM is able to view surface detail that can't be

seen when the probe voltage is high. For example, the bright squares at right center, formed from beam induced depassivation, cannot be seen at +/- 10 V but can at +/- 1 V.

### 5.2 (a) Discussion of STM bias on SEM Image Position and Contrast

The explanation for both the brightness and movement lies in the balance of voltages between the probe and secondary electron detector (SED), which has a dc bias of 10 kV around it and is about 15 cm from the sample. At positive polarities, the probe attracts electrons which would otherwise go to the SED. That reduces the electron flux to the SED and makes both the probe and sample appear darker. The probe also draws more primary (incident on the sample) electrons in its direction, so it appears more centered in the image. At negative polarities the local potential is distorted, so that some of the electrons that would be drawn to the SED are repelled into the chamber walls instead. That again reduces the electron flux from the sample, so it appears darker. Figure 5.2 shows however, that the probe is brighter at -10 V than at +10 V. This is because there are more electrons available from the probe at negative polarity. At negative polarity the probe also bends primary electrons away, so it appears off center. A schematic model of this mechanism is shown in figure 5.3, where electric fields in the chamber are modeled as potential wells. Some possible electron trajectories are shown.

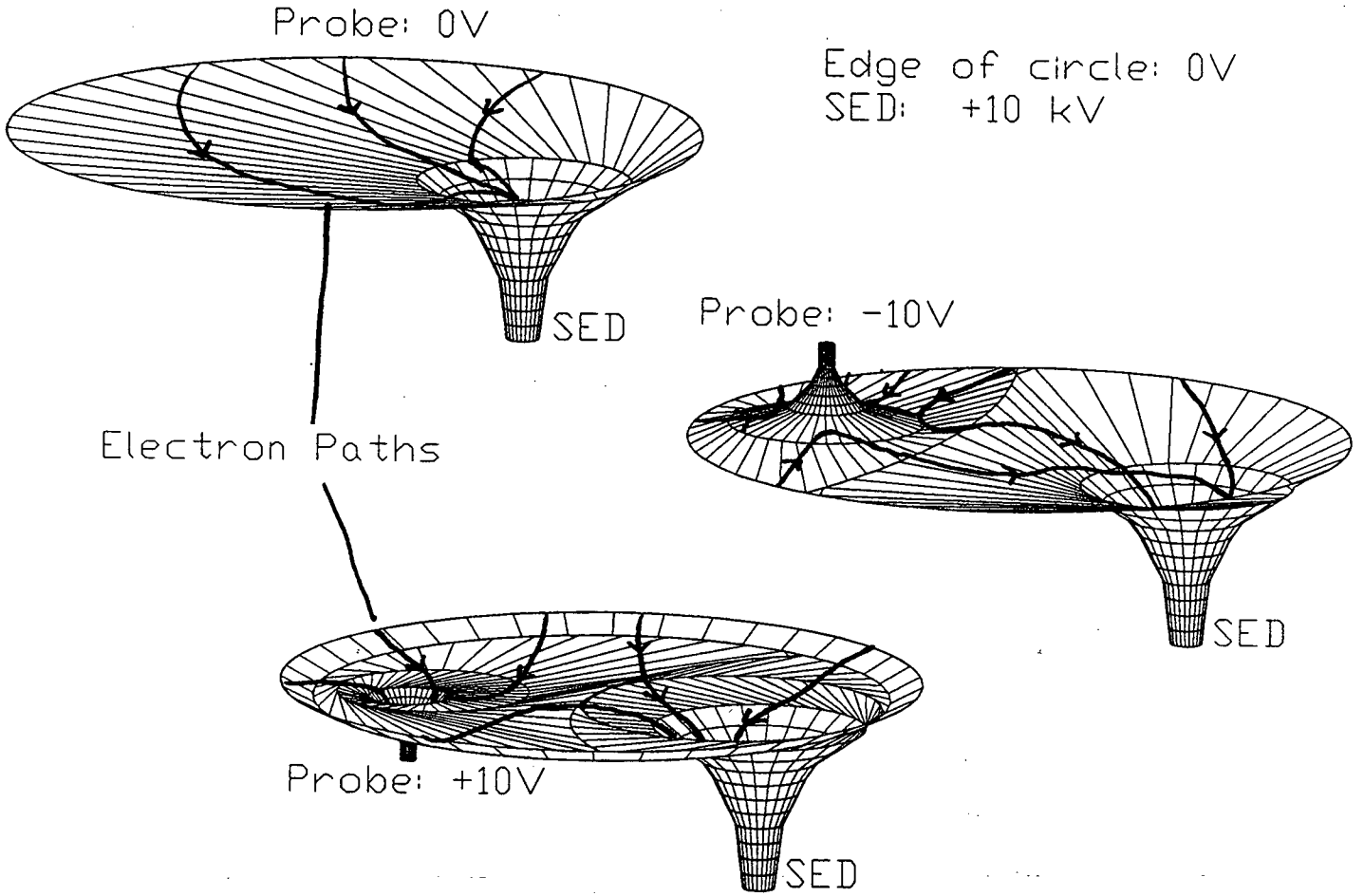


Figure 5.3. Representation of the electric fields in the SEM chamber from the STM probe and secondary electron detector

## 5.3: SEM Characterization of STM Behavior

The SEM has proven to be an excellent tool for characterizing the performance of the STM, in particular helping to determine causes of poor imaging, and to determine when the STM produces false images in response to structures with large vertical topography or multiple tunneling sites.

### 5.3(a) Sources of Poor STM Imaging

There are a number of ways the STM's performance can be degraded. The most dramatic is when the STM encounters insulating material thick enough to stop tunneling completely. Insulating material can either be intrinsic to the surface, such as the insulating components of the FET structure in figure 4.8, or particles of dielectric material acquired by the probe. Even if the intrinsic insulating material only comprises a portion of the total surface area scanned, it will completely destroy the image if sufficiently thick. On encountering the insulator, the probe, no longer finds current, and is driven into the surface, where it sticks. Lateral movement of the scanner can often dislodge the probe, but imaging is fatally compromised.

Figure 5.4 and 5.5 show STM and SEM images of a region of Si (100). In this case, the probe became severely contaminated and stuck to the surface. Scanning just caused it to bend, pivoting back and forth around the contact point. Figure 5.5 shows the corresponding apparent STM image, which is not consistent with normal imaging. This STM is particularly suited to such SEM characterization because the probe is fixed and the sample moves. The probe should ideally remain perfectly still while the STM is scanning. Any probe movement indicates the probe is contacting the surface, either through the presence of insulators, or extreme vertical topography the scanner cannot compensate for.

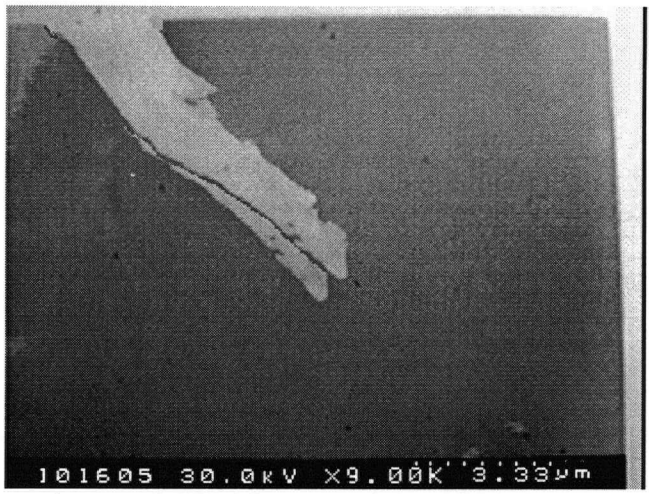


Figure 5.4: Two superimposed SEM images of the STM tip. The tip was stuck to the surface and flexed back and forth as the sample was scanned. The two images were obtained at the limits of the STM's range of motion.

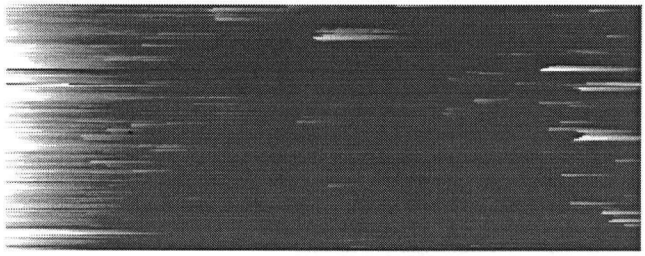

Figure 5.5: STM image taken with probe shown in figure 5.4, XY = 2.0. The surface is Si (100) but the image is clearly inconsistent with other Si (100) images such as figure 7.11.

Contamination of the tunneling junction by acquired dielectric particles resulted in varying image degradation. (100) Si passivated with buffered HF was found to be particularly susceptible to this effect,[43] though it also occurred with GaAs, Au, and Si (111). A method for removing acquired dielectric material is described in Section 7.1(b).

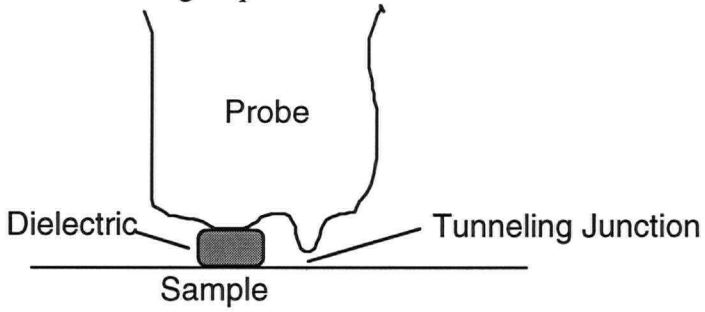


Figure 5.6: A model of probe contamination. The dielectric acts as a spring, causing the tip to bend and reducing the change in current due to tip movement.

Acquired dielectric particulates as shown in figure 5.6, have been modeled by Coombes and Pethica as a spring under the probe.[44] Tunneling still occurs, either through or beside the dielectric, but the effect of changes in the tunneling junction width is reduced by elastic distortion of the tip, due to the added mechanical resistance of the dielectric. The STM controller must amplify movements in Z to maintain the current setpoint, and as a result, vertical topography is exaggerated. Figure 5.7 shows successive clearing and recontamination events. As the probe becomes contaminated, the apparent height of surface structures increases. When the contamination spontaneously clears, tunneling returns to normal, with only small variations in surface height.

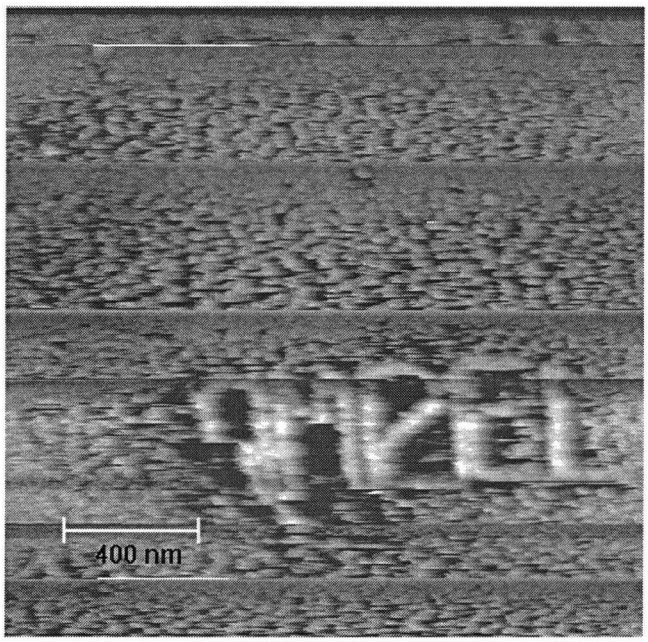


Figure 5.7: Si (100) surface imaged at by STM at -10V, 0.3nA, showing sucessive contamination and tip clearing events. Increasing contamination results in increasing apparent height of topography. The "AMPEL" pattern was written by depassivation lithography as discussed in section 7.2.

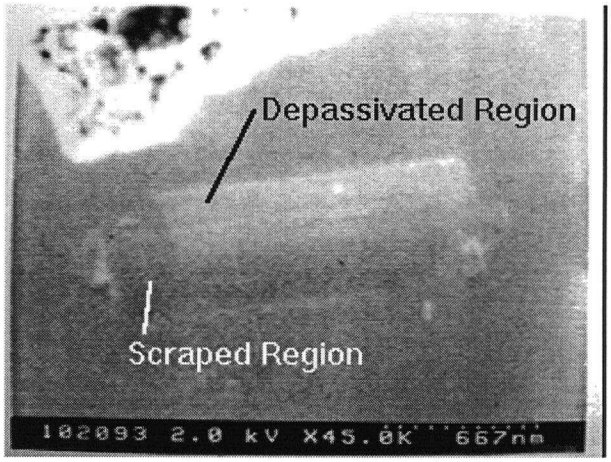


Figure 5.8: SEM image of STM scan area with simultaneous depassivation and mechanical scraping.

Evidence for simultaneous mechanical contact and tunnelling is presented in figure 5.8. This SEM image shows an area of Si (111) scanned by the STM. The silicon had been passivated with HF which removes the surface oxide and repalces it with hydrogen. The STM was operating at -10V and 3nA and the resulting image is shown in figure 5.9. This large negative voltage causes the hydorgen to be removed. This depassivation of the surface is described in detail in section 7.2. Here it is useful because, as in the calibration experiments in section 2.5(a), it reveals the precise region of the surface which has been exposed to the high electric field from tunneling. This region appears as a bright rectangle in figure 5.8. Below the depassivated area is a dark region with material pushed out to either side. It is believed that this area has been mechanically scraped by the probe. When the tunneling junction on the probe encountered the scraped region, imaging, which up to that point was reasonably good, suddenly deteriorated.

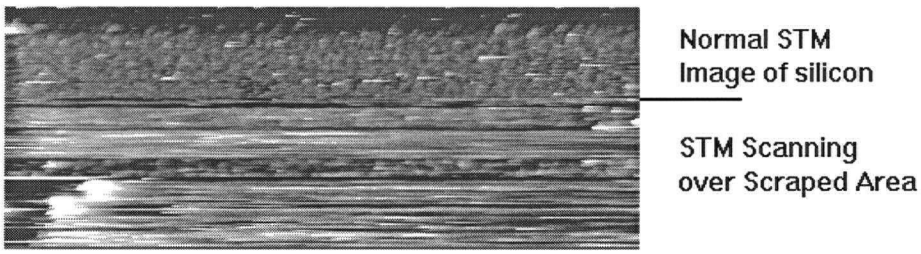


Figure 5.9: STM image corresponding to figure 5.7. Imaging conditions were: V = -10V, i = 3nA, XY = 3.0.

Figure 5.10 shows a similar picture, where the STM was imaging one area of the sample while being in mechanical contact with another. In this case, the scan range was kept small enough that the affected regions did not contact each other. There also appear to be two depassivated areas which implies two tunneling junctions. The upper right site appears to be less depassivated than the lower site, which suggests a weaker field and therefore a greater tunneling gap.


Figure 5.10: SEM of STM scan at XY = 0.5, showing two tunneling sites and a dark scraped region. The three squares are identical in size.

Figure 5.11 shows another case of two tunneling sites on the end of a probe. In this case, a lithography pattern was written, as described in section 7.2. The result was observed with the SEM, which revealed two identical patterns separated by approximately 0.5μm.


Figure 5.11: Two STM depassivation lithography patterns created simultaneously by two tunneling sites on the probe. The writing conditions were: V = -10V, i = 3 nA, XY = 1.0.

### 5.3(b): STM Imaging of Large Steps

Multiple tunneling sites are most likely to appear after a PtIr probe has been crashed so that a larger section of tip lies along the surface. This increases the probability of two sites on the probe coming into contact with the sample. Even when there is only one tunneling site however, a large end radius can limit the STM's ability to produce real images of surfaces with significant vertical topography. Figure 5.12 shows a region of HF passivated Si (111) scanned by a probe (seen in figure 5.2) which had been previously crashed. On the left side of the image is a cleavage step of 25nm. The dark line in the area to the right of the step is a region of sample that was not depassivated by the scan, indicating that tunneling did not occur there. It has a width of approximately 160nm.

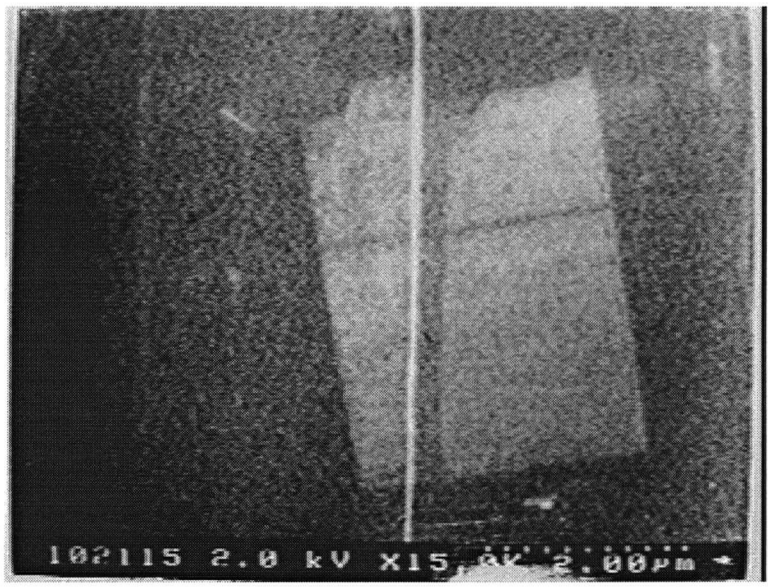


Figure 5.12: SEM image of an STM scan of a 25 nm cleave step on passivated Si (111).

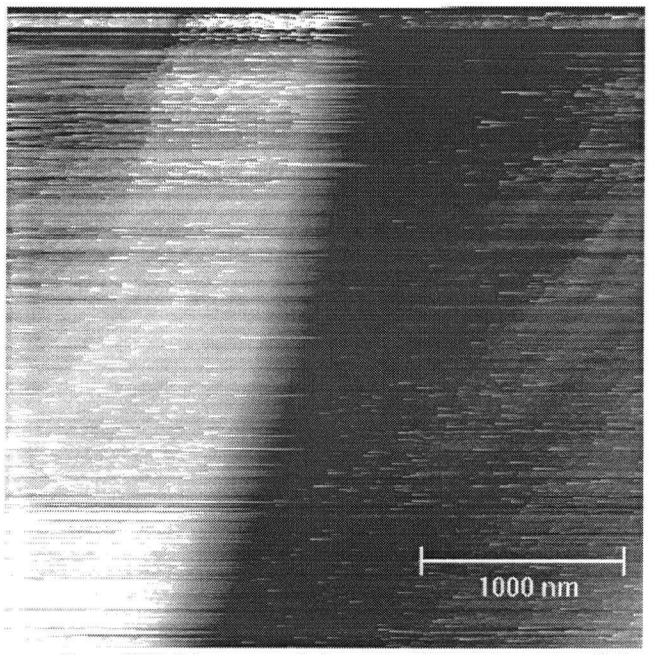


Figure 5.13: Corresponding STM image of the step. Imaging conditions were: V = -10V, i = 3nA, XY = 6.0. The 850 nm wide bright band in the image is thought to be an artifact of the STM controller compensating for the large step.

If the tip is approximated by a sphere, as in figure 5.14(a), its radius can be found using the formula $x^2+y^2=r^2$, assuming the sphere simultaneously touches the edge of the step and the surface 160 nm away. In this case a minimum radius of 525 nm is found. As evidenced by figure 5.13, the STM image does not show any evidence of a discontinuity. Without the SEM therefore, it is impossible to tell that anything is amiss.

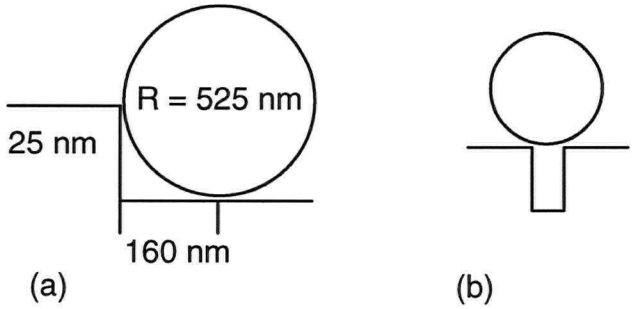


Figure 5.14: Two cases where tip radius limits the STM's ability to image the surface. (a) represents a step, as in section 5.3(b), and (b) represents a groove, as in section 5.3(c)

### 5.3(c): Resolution of High Aspect Ratio Topography

A related situation is presented in figure 5.15 and 5.16. These show a GaAs/AlAs structure grown by M.O.C.V.D.[36] which consists of two 50 nm AlAs layers, seen as dark lines, surrounded by undoped GaAs and sandwiching p-type GaAs. At the center of the p-type GaAs is an InGaAs monolayer. The sample was cleaved in air and passivated in $NH_4S$ at 50°C for 10 sec.[24] The $NH_4S$ preferentially etches aluminum compounds, so the AlAs layers became deep grooves, whose bottom could not be seen by the SEM. Although it was possible to rapidly evaluate the quality of the cleave and position the probe for imaging, the sample itself was very prone to contaminating the probe. The result was multiple tip crashes and many attempts to clean the probe with field evaporation (section 7.1(b)). When stable STM images were obtained, it was found that the AlAs grooves did not appear. This is thought to be due to the situation described in figure 5.14(b), where the end radius of the probe is too wide to allow the tunneling junction to reveal the bottom of the groove. When the tunneling junction drops into the groove, another point on the probe takes over as the tunneling junction until the probe gets to the other side of the groove.

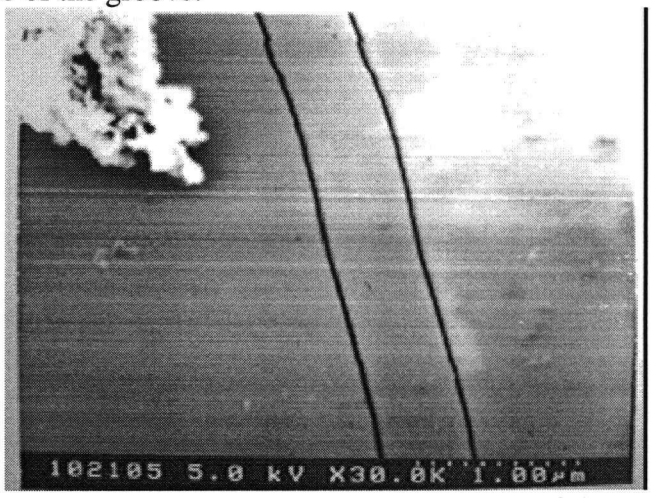


Figure 5.15: SEM image of GaAs/AlAs structure. The edge of the sample is at the upper right corner of the image. The waviness of the dark lines, and the of the lines across the image are due to poor SEM operation.

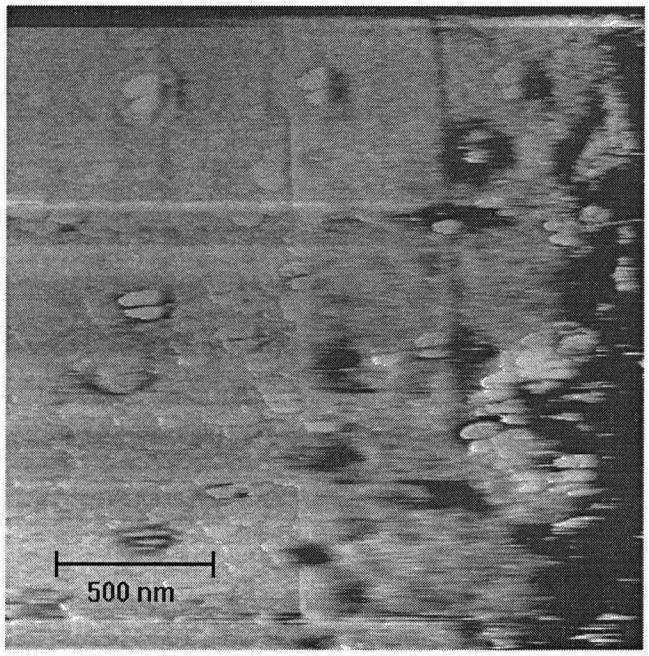


Figure 5.16 (a): STM image of the structure. Imaging was at V = +4V, i = .3 nA, XY = 4.0 . This image displays a number of multiple tip images, evidence a blunt probe. The AlAs grooves are visible as parallel lines at the center of the image.

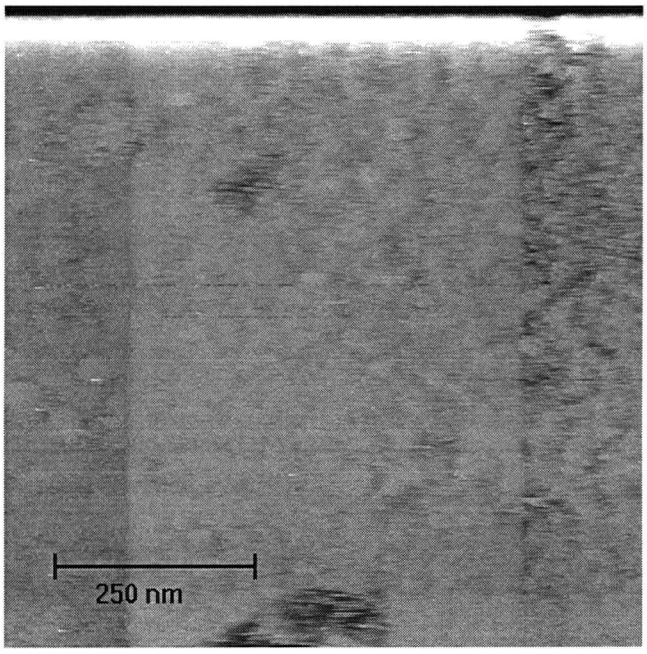


Figure 5.16 (b): Higher magnification image of the same region: XY = 2.0. The grooves are completely invisible although contrast between the undoped GaAs on the left and right, and p-doped GaAs in the center, is visible.

## 6. Carbon Deposition and E-beam Induced Surface Depassivation

An important consideration in the development of the combined SEM/STM was the impact of carbon deposition on the tunneling microscope. This effect, common to all HV SEMs, is due to the presence in the chamber of hydrocarbon molecules from the diffusion pump, SEM stage, or samples. These molecules are cracked by the SEM beam and attached to the sample. Over time, this results in a build up of cross polymerized carbon in the area of the beam, which obscures the actual sample surface.[45] Such a layer poses a potentially serious problem for the SEM/STM because any such buildup might limit the STM's ability to tunnel on the surface.[17] Even a few monolayers would stop the STM from resolving surface atoms.

Experiments were undertaken to determine the significance of this effect, particularly in the case of silicon, where carbon deposition might have an adverse effect on the STM's ability to do nanolithography. Results indicate that while carbon deposition was indeed present, it could be controlled. In the course of investigating carbon deposition, it was found that SEM-induced silicon depassivation was in fact, more damaging and difficult to control.

### 6.1. Carbon Deposition Measurements by STM

The rate of carbon deposition is proportional to the accumulated charge per unit area, or alternately, the square of the magnification.[46] When magnification is doubled, the area exposed to the beam falls by a factor of four, so the deposition of rate carbon per unit area goes up by a factor of four. The difference between buildup rates at lowest and highest magnification is a factor of $5 \times 10^7$ (thickness/time). The strategy for avoiding contamination therefore, was to keep the SEM at its lowest magnification during STM

operation. Magnification was only increased for short periods of time to position the probe or monitor probe behaviour during scanning.

It was found that carbon was deposited faster at low accelerating voltages. This is thought to be due to the fact that low energy electrons interact with the carbon more than high energy electrons. A contributing factor may be less surface heating at low electron energies, which allows the carbon to adsorb more easily.[45] It was also possible to see the surface layer better at low accelerating voltages, because of the shorter penetration depth of the electrons at low energies.[46] This is also evidence of more surface interaction at low accelerating voltages. In the SEM, thin carbon deposits appeared darker than the background on metals like Au and TiN, and lighter on semiconductors like Si, and GaAs. The STM was able to image deposits provided they weren't too thick. Both of these observations are consistent with carbon being a semi-metal.

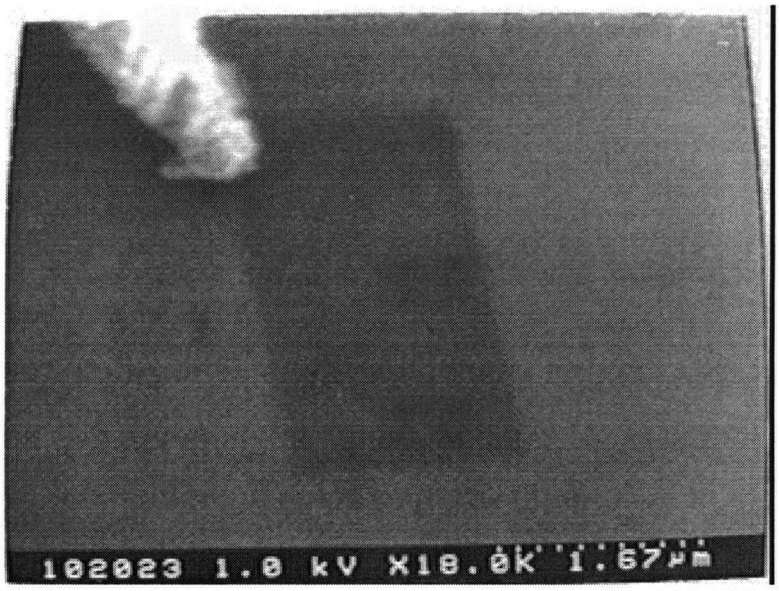


Figure 6.1: SEM image of three carbon squares, each exposed at 300,000X. The squares are 400 nm x 300 nm. Exposure times are shown below in figure 6.2. The STM probe is visible at top left. The lighter area surrounding the carbon squares is the depassivation region left by the STM scan. That scan produced figure 6.2.

Eight experiments of the type shown in figures 6.1 to 6.5 were done. Si (111) samples were cleaved and passivated for 30 s in 10% buffered HF, then rinsed in DI water. Regions on the cleaved edges were then exposed to the SEM beam at 150,000X

and 300,000X, at 1.0 kV. At 300,000X, sets of three squares of carbon were deposited for five, ten, and fifteen seconds, then scanned with the STM. At 150,000X, a single square was deposited and then imaged with STM. The thickness of the deposits were estimated by averaging the STM's feedback signal as it scanned over the deposits. Deposition rates, normalized to 300,000X, of between 0.6 nm/s and 2 nm/s were observed. Within each image, the deposition rates for the squares were within about 20% of each other.

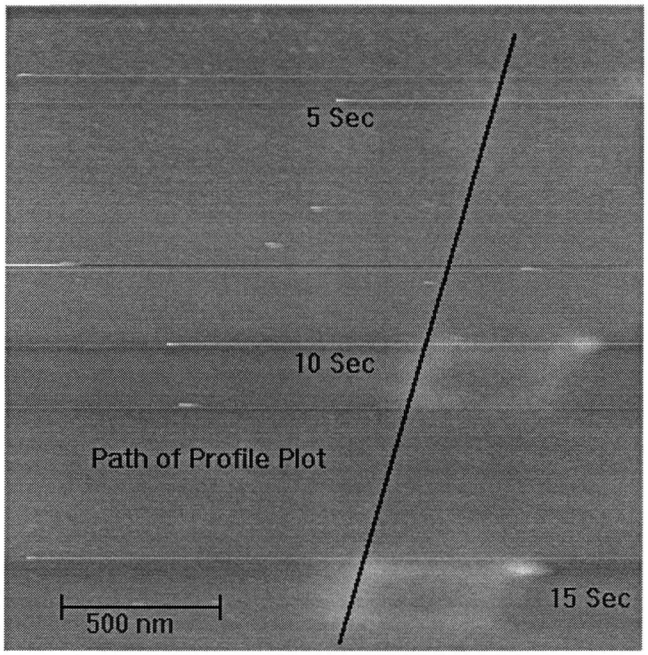


Figure 6.2: STM image corresponding to Figure 6.1. Imaging conditions were: V = -10V, i = .3nA XY = 4.0. Times refer to exposure times of each carbon square. The profile plot appears in figure 6.3

An ion gauge added to the SEM chamber showed that the SEM could be turned on after evacuation with a chamber pressure of $1x10^{-5}$ torr. Over the next two hours, the pressure would drop to $1x10^{-6}$ torr. Deposition rates of about 2 nm/s were seen within an hour of the SEM being pumped down. Rates around 0.6 nm/s were observed the next day, when the SEM had remained under vacuum overnight. The cold trap was filled at the beginning of each day so it should have had the same effect throughout.

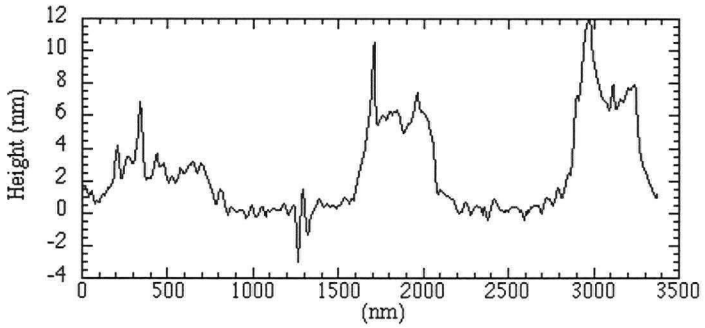


Figure 6.3: Profile plot of the three carbon structures showing the effect of exposure time on depth of carbon deposition.

The deposition rate observed is difficult to compare with those in the literature, as field sizes and accelerating voltages are not always given. Values in the literature range from .1 nm/s to 1 nm/s but the conditions are not quoted.[45-48] A factor of four reduction in deposition has been observed with the addition of a cold trap.[45]

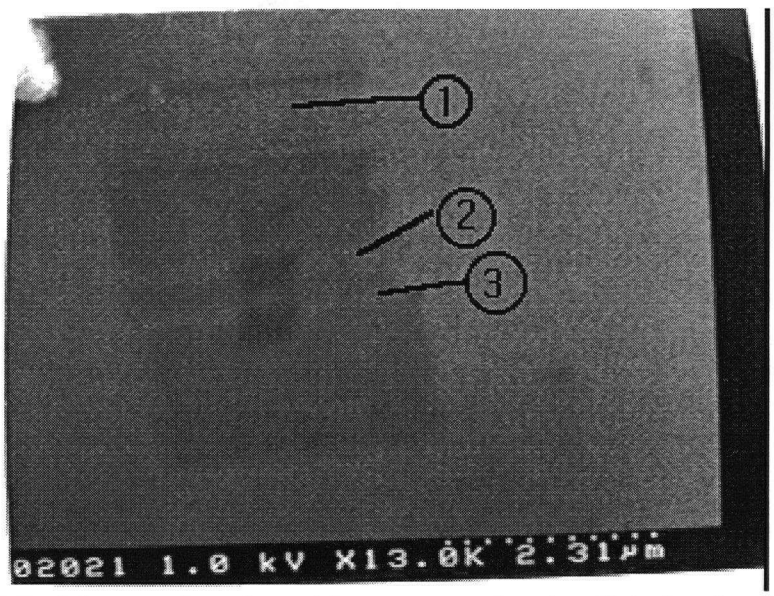


Figure 6.4: SEM of three carbon deposition squares showing light bands where contamination on the probe temporarily halted depassivation. Squares are approx. 400nm X 300 nm. The three light bands are marked and correspond to the three marked regions in figure 6.5

A convenient property of deposited carbon is that it does not adhere strongly to the probe. Consequently, if the probe encounters a carbon deposit, the tunneling region will not be permanently contaminated. Evidence of this is shown in figures 6.4 and 6.5, which again exploit the SEM's ability to image depassivated silicon, as in sections 2.5 and 5.3. During the scan, the tip temporarily acquired some dielectric, possibly carbon, which shielded the surface from the tunneling field, and left non-depassivated regions, marked as 1, 2 and 3 in the figures. The first incidence of contamination is likely due to an acquired surface particle, as it occurs before the STM encountered the carbon deposits. The second and third occurred while the carbon squares were being scanned, but they were only temporary, and the bottom third of the STM image was stable. Figure 6.2, with thinner deposits, shows no evidence of acquired particle contamination, from either the surface or carbon. If the carbon were capable of seriously contaminating the probe, it would significantly compromise the performance of the instrument, so the lack of such an effect is extremely fortuitous.

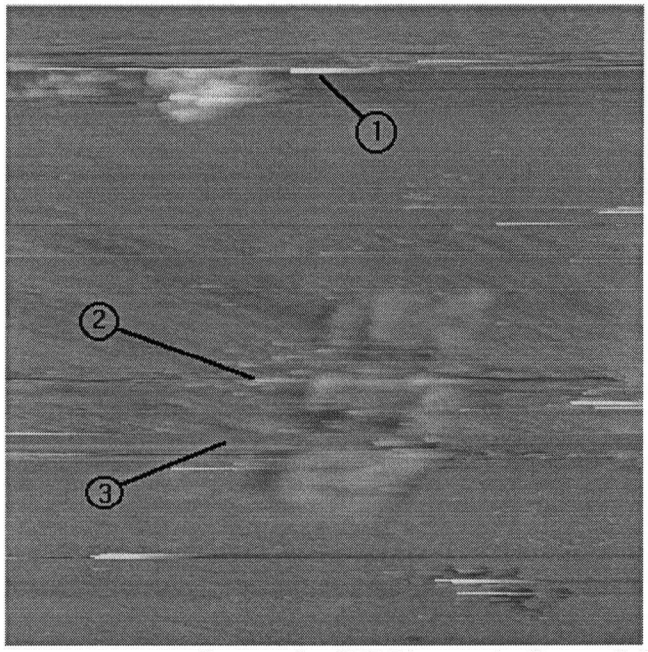


Figure 6.5: STM image corresponding to the SEM image in figure 6.4. Imaging conditions were: V = -10V, i = .3nA, XY= 6.0 The carbon squares are compressed together because of the STM's distortion. The three light bands in figure 6.4 appear as poor image regions in this image.

It is possible that the squares in figure 6.2 are in fact due to beam induced depassivation. There is evidence however, that these squares really are carbon. The most likely mechanism for buildup involves adsorbed hydrocarbons being decomposed and bonding to the sample. More hydrocarbons diffuse across the surface and are cracked as they reach the area scanned by the beam. The result is image sized open rectangles, such as the one shown in figure 6.6. The high point in the upper right corner appears in all depositions and suggests that the beam dwells there for a longer period of time than other areas.

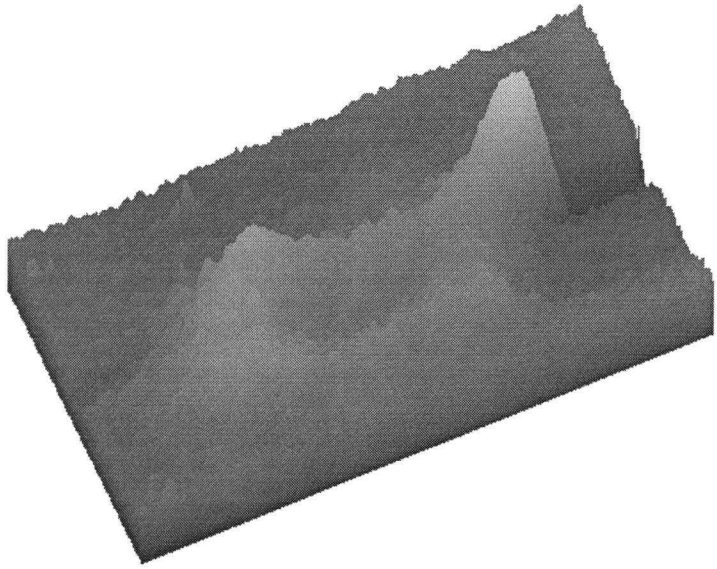

Figure 6.6: Isometric view of the deepest carbon structure in Fig 6.2, displaying the characteristic ridged form of contamination patterns.

## 6.2 SEM Induced Surface Depassivation

A further challenge in the study of passivated silicon surfaces with the combined instrument was the discovery that the SEM was capable of depassivating the surface at all accelerating voltages.[49] The depassivated surface displayed enhanced secondary electron yield, similar to regions depassivated by the STM. Depassivation occurred much more rapidly than carbon buildup; regions began to depassivate after only a few seconds at

10,000X to 50,000X, typical magnifications used for aligning the STM or imaging STM made nanostructures. Figure 6.7 shows a number of depassivated sites on a Si (111) surface. Exposure of different sites varies. Many of the brighter squares were formed when taking Polaroids of STM patterns, which involves exposure of at least two minutes. The less bright contamination occurred when observing the probe for periods typically under one minute.

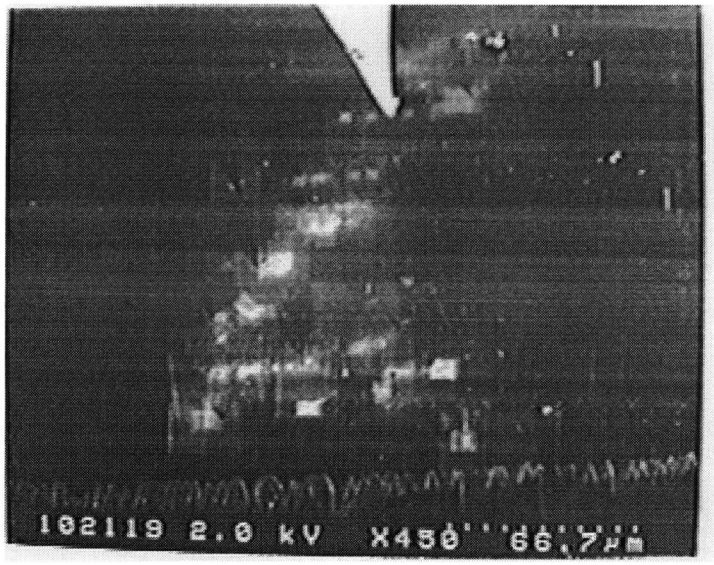


Figure 6.7: SEM image of SEM and STM induced surface depassivation. Brighter regions are due to longer exposure times or higher magnifications. Note the tip shadowing of probe at left center.

Quantitative analysis of this effect was not made, however, qualitatively the rate of depassivation appeared to obey the same magnification-squared rate law as carbon deposition. Such behaviour is to be expected given that the rate of depassivation must be proportional to the charge per unit area. Unlike carbon deposition, depassivation is more severe at high accelerating voltages, particularly with freshly passivated samples. Dagata et al. have suggested that rapid depassivation of fresh samples is due to the presence of OH groups on the surface, from rinsing the sample in water, which aids the depassivation process.[49] It was found here that leaving the sample in the chamber for several hours significantly reduced the depassivation rate.

Whereas the bulk of the carbon deposition occurred at the edges of the exposed region, depassivation occurred evenly across the surface. Evidence that depassivation is indeed beam-induced comes from the shadowing effect of the probe. After a region around the probe was exposed, and the probe was moved, an unaffected region of the surface is revealed, precisely corresponding shape of the probe. Examples of this can be seen in figure 6.7.

SEM-induced depassivation was found to affect imaging of freshly passivated silicon more seriously than carbon buildup. For example, the STM-made patterns detailed in section 7.2 (below), were repassivated after wet etching. Subsequent SEM imaging would render the patterns invisible in less time than was needed to obtain a photograph. The effect of SEM induced depassivation on patterns before transfer was not investigated, but it can be assumed that exposure to the SEM beam could render large areas non etchable. Certainly high magnification imaging of STM made patterns before etching would render the pattern invisible as the surrounding region would become rapidly depassivated. It should also be noted that unlike carbon deposition, this effect is likely to occur in UHV.

## 7. Lithography

Pattern generation using scanning probe microscopes has been an active area of research almost since the invention of the STM. Both STM and atomic force microscopes (AFM) have been employed and several different methods of surface modification have been reported. These include organometallic deposition,[50,51] resist exposure,[52,53] anodization[54], and mechanical deposition or removal of material.[55] Another very promising method has been oxidation of passivated silicon.[1,49,57-63] Using this technique, side gated transistors have been produced.[64-66] Such techniques, particularly depassivation of silicon, hold out the promise of lithography down to atomic scales.[61,67] Another valuable property of SPM lithography is that it can be done using small scale laboratory instruments, which has allowed research at relatively low cost.

Field evaporation and silicon depassivation experiments were carried out. Results were mixed with the former method, although they led to an important discovery for removal of tip contamination. With silicon depassivation, the usefulness of the combined instrument was clearly demonstrated, as it was possible to view patterns by SEM immediately after writing, and recover patterns on samples removed for ex-situ wet etching.

### 7.1 Field Evaporation Lithography

Field evaporation is a process by which atoms are ionized and liberated from a surface by a high electric field. Evaporation is facilitated by the use of a sharp probe as emitter, to concentrate the field. The technique described here uses the STM probe as an emitter, and exploits the small tunneling junction by requiring a relatively low voltage to produce a sufficiently high electric field for tip material to evaporate. The tip acts as a

miniature solid state source of material which can be deposited on the surface in well defined mounds by means of voltage pulses.

Pioneering work in this area was done by Mamin et al.[56,68] They report reliable deposition of mounds from gold wire on gold substrates in air at between -3.5 and -4 V. In UHV, the threshold rises to about -5V and deposition probability drops from near 100% in air, to about 50%. Beyond threshold, the mounds did not appear to grow substantially, although removal of surface material could take place if multiple pulses were made over the same region. Pulse lengths varied from 10 ms to 10 ns. This technique has also been used with a combined SEM/STM to modify e-beam fabricated wires.[69]

To be able to produce voltage pulses in the probe sample junction, the sample was isolated on specially constructed sample holder, shown in figure 7.1. A copper cap was epoxied to a plug made from Vespel, a UHV compatible polyamide, so the holder had the same dimensions as an SEM sample mount. The cap was then wired through the preamplifier feedthrough to a 50Ω coaxial cable and a 50Ω resistor to ground.

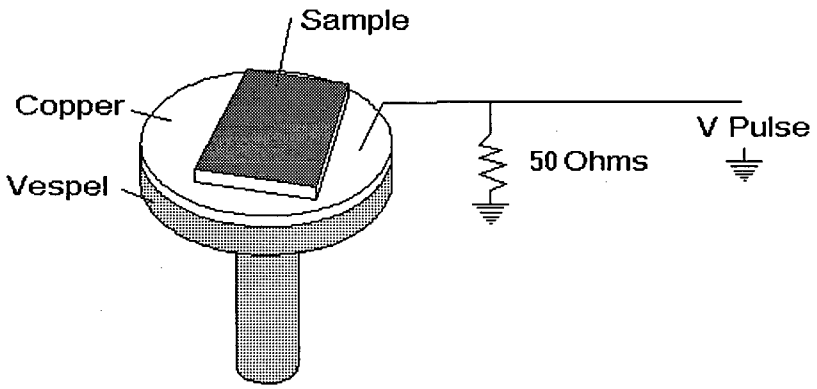


Figure 7.1 Insulated sample holder used for field evaporation lithography and tip clearing

Samples were glued to the copper by means of silver paint. Gold evaporated on silicon was used for most experiments, although attempts were also made with Si, GaAs and TiN substrates. Both Au and PtIr probes were used. Software (See Appendix B) was developed to drive the probe over the surface between points at a specified speed, while

pulses were being generated. Pulse voltages varied from +/- 4 to +/-12 V and lengths were from 10 μs to 50 ns.

Although depositions were made, the deposition probability was much lower than expected and voltage thresholds were higher. No difference was found between Au and PtIr, either in deposition probability or voltage threshold. In contrast to results reported elsewhere, deposition probability also tended to go down after many pulses. The deposition threshold would typically start at -8 V but could rise to above -10 V after a few thousand pulses. Crashing the probe into the gold sample, to coat the probe in gold, would temporarily reduce the threshold, but it would soon rise again.


Figure 7.2 SEM of a square of deposited PtIr, formed by 1μs pulses at -12V and 1.0 kHz.

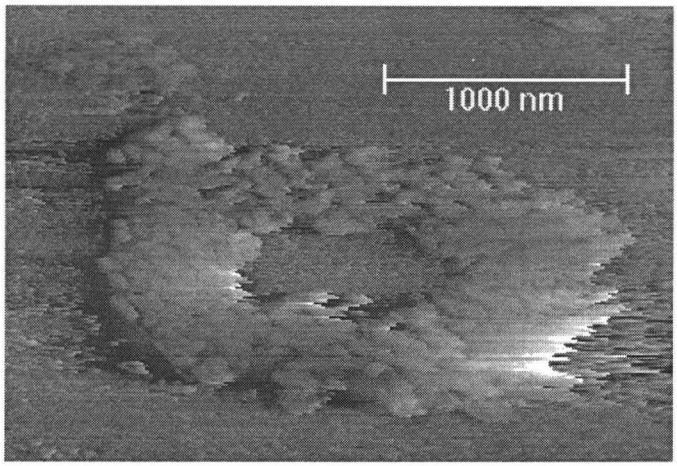


Figure 7.3: STM image corresponding to figure 7.2. The broadening of the mounds into continuous lines is due to superimposed multiple tip images.

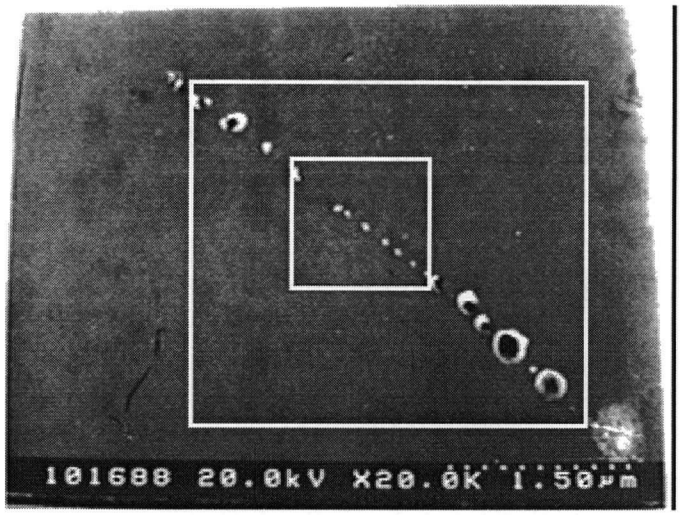


Figure 7.4 SEM image of a line written with a PtIr probe. Pulses were +10V at 1µs and 100 Hz. Writing speed was 0.1 µm/sec. The smaller square is the region shown in fig 7.6 and the larger is the region shown in fig 7.5

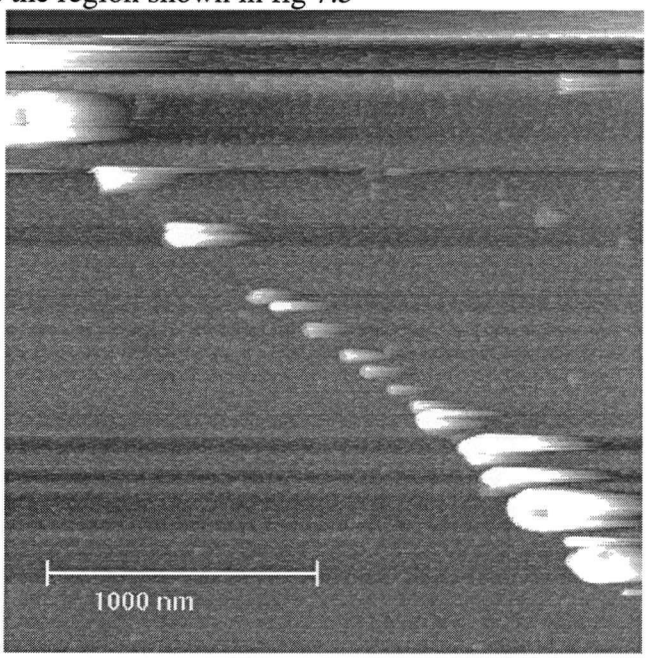


Figure 7.5: STM image of the same line. Imaging conditions were: V = 1V, i = 1 nA, XY = 5.0. The height of the larger blobs is approximately 40 nm

Figures 7.2 to 7.6 show STM and SEM images of patterns made by field evaporation. Both patterns exhibit low deposition probability. The line in figure 7.4 is 4.5µm long and took 45 seconds to write. A total of 4500 pulses occurred with 21 events, some of which were mound depositions and some of which were pit formations. This represents a deposition probability of 0.5% at -12V. The pits formed in the sample at this voltage are consistent with results reported by Mamin.

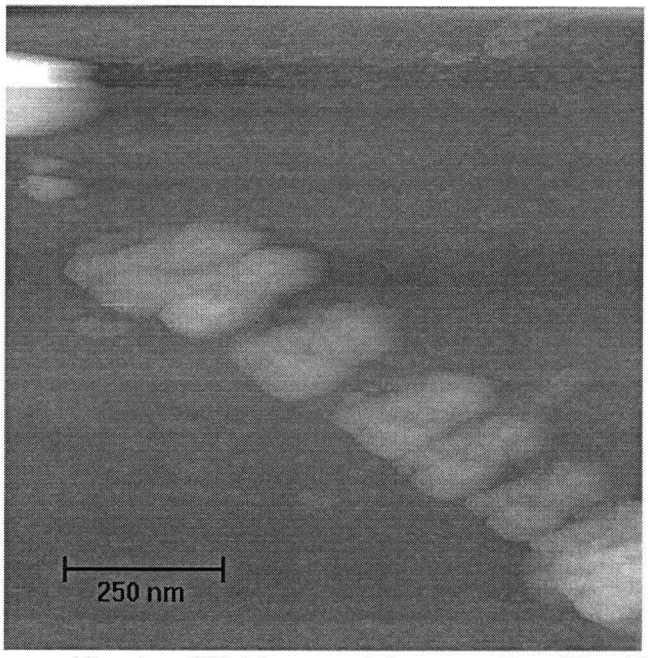


Figure 7.6: Higher magnification STM image of the same line. V = 1V, i = 1 nA, XY = 2.0. The mounds at center are roughly 18 nm high.

Occasionally, the STM would produce dark lines instead of mounds. While figure 7.5 and 7.6 clearly show mounds, figure 7.7 shows a dark groove, as does figure 7.10, to the left of the crater. It is possible that material from the gold surface was evaporated onto the PtIr probe. The effect was inconsistent though and a more likely origin is mechanical scraping by a contaminated tip.

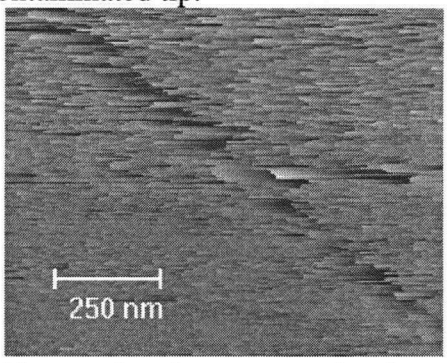


Figure 7.7: Section of STM image showing a groove in place of deposited material.

There are several possible explanations for the low deposition probability that was observed. Mamin observed a lower evaporation probability in UHV, with which these results are consistent. In some cases particularly on the gold sample, screening by dielectric material in the tunneling junction may have reduced the electric field

experienced by the surface of the probe. Evidence for this lies in the quality of the images produced by the STM after patterns were written. In cases where the probe may have been contaminated, the gold surface was not properly imaged. Compare for example, figure 7.7 with figure 4.4, both images of evaporated gold. In the cases where the backgound did not image clearly, the probe either formed grooves or the surface was not modified. Figures 7.4 to 7.6 show a case of material deposition where the background surface is well imaged, evidence of a clean probe. Mamin's experiments were done on (111) gold facets which may have been cleaner than the evaporated gold sample used here.

The rising threshold is thought to be due to smoothing of the probe after many evaporation events. Here, relatively large voltage pulses were used which, when sucessful, typically produced large mounds. This may have smoothed the tip more rapidly than in the case of smaller mound deposition. Preliminary SEM observations were made of the tip of a probe which had been used in this way. The tip appeared much smoother than the side surface of the probe.

### 7.1 (a) Static Discharge Effects

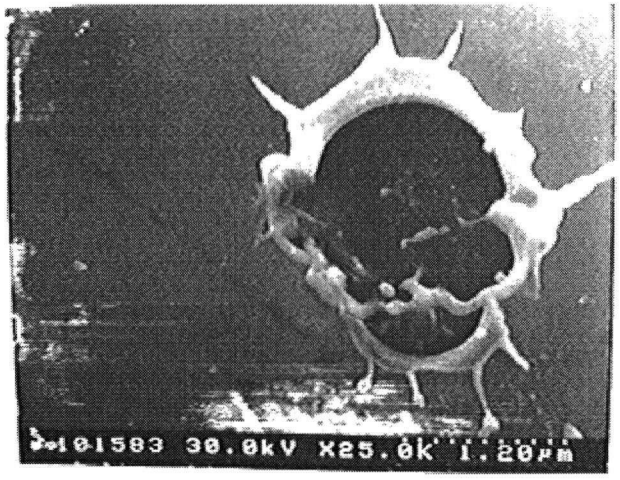


Figure 7.8 A crater formed during imaging of a field evaporation pattern. The line formed by field evaporation is seen at left.

Mamin et al reported that their apparatus was sensitive to static effects, which would result in large uncontrolled depositions.[56] Similar features were observed here, when imaging evaporation patterns on gold. The surface would appear to have been impacted or locally heated so that the gold layer was pulled away from the substrate, forming a crater. This effect could be caused by connecting or disconnecting coaxial cables in the system, but sometimes occurred randomly. The crater shown in figure 7.8 dwarfs all other observed surface modifications, save crashing the tip and dragging it across the surface. Discharges occurred in a lot of cases with this gold sample, and always led to imaging breakdown, although the probe would continue to work if moved to another site.

### 7.1(b) Tip Clearing by Field Evaporation

Although lithography by field emission did not prove to be as reproducible as one would like, it was useful for removing acquired dielectric contamination from the probe (section 5.3). Figure 7.9 shows a particularly dramatic example of this effect.

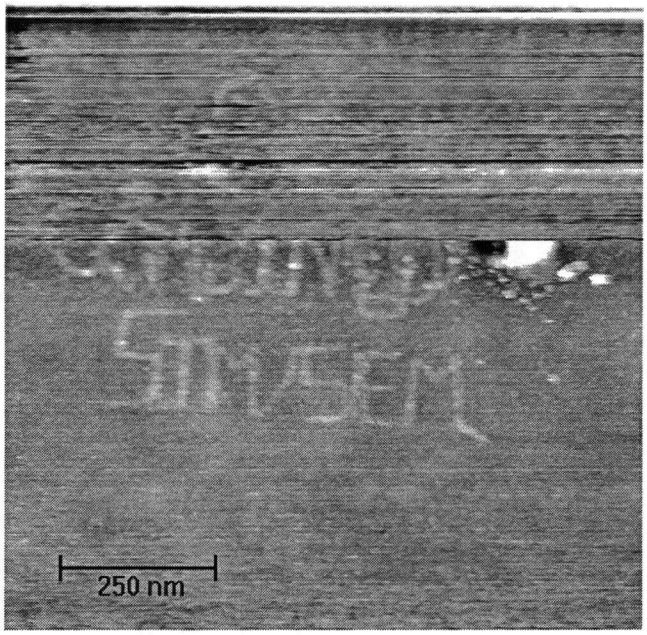


Figure 7.9 STM image where the contaminated tip was cleared by voltage pulses, which restored imaging. The text was written by depassivation lithography. (Section 7.2)

At the point where the imaging improved, a mound on the surface can be clearly seen. Above that, the image displays typical characteristics associated with tip contamination. As soon as the material was released from the end of the tip, without any significant change in position, imaging returned to normal.

Tip clearing was used a great deal. In the case of the combined instrument, it had the great advantage of often avoiding tip replacement, which wastes time, exposes the sample to air, risks misalignment or crashing the probe and raises the SEM chamber pressure. The pulse generator was set at 10 V at a polarity opposite to that of the probe. To maximize the probability of a field emission event, 1 μs pulses at 1 MHz were used . The generator was then switched on for periods of a few seconds, after which the STM's Z-drive signal was examined to determine if its amplitude was consistent with good image quality.

## 7.2 Depassivation Lithography

The other lithography technique investigated was the surface modification of passivated silicon. This depassivation lithography, pioneered by Dagata et al,[49] involves scanning a passivated material with a tip bias above some threshold value, selectively removing the passivated layer and allowing the surface to oxidize where it has been depassivated. The formation of a thin oxide layer is convenient as a patterning method, since oxides tend to be very stable and effective as etch masks, despite being only a few nanometers thick.[57] SPM lithography offers the possibility of making very small structures. Because of the relatively low voltages used (≤10V), there are few of the proximity effects associated with e-beam lithography.[65] Linewidths of 20-25 nm on passivated Si in air,[60] and 1 nm in UHV,[61] have been observed.

The mechanism for patterning is believed to be field induced removal of hydrogen on the passivated Si surface.[49] At low voltages, the surface can be scanned without being affected. Beyond some threshold value however, depassivation takes place and the hydrogen is either replaced with oxygen when imaging in air, or in the case of UHV, the silicon is left exposed. The value of this threshold depends on ambient pressure. Dagata et al, reported patterning in air at +3.0 V.[57] STM images of patterns showed dark structures, evidence of oxidized regions. Lyding et al, working in UHV, reported a threshold at -5.5V and no depassivation at positive polarity. Depassivated atoms appeared lighter than the background, suggesting unoxidized surfaces.[61] It is believed that in air, ambient oxygen and adsorbed water, take part in the reaction.[57]

### 7.2(a) Pattern Transfer

Experiments followed the sample preparation and etching method of Snow and Campbell.[58] The formation of patterns for use as etch masks as well as their transfer to the substrate by etching, were investigated. This led to a studies of voltage thresholds for

depassivation and the effect of different types of silicon on the process. In early experiments, 0.025 Ωcm *n*-type (100) silicon was hydrogen passivated with 6:1 buffered $NH_4F$:HF for 40s, blown dry in dry $N_2$ and mounted flat on the sample holder with silver paint. (100) was used because it is more readily etched than (111).[58] Attempts were made to write patterns at +/- 5 V and 15-20 nA. To locate these patterns after etching, V-shaped scratches were made on the surface with a scribe, and patterns were written in rows, near the apex of the scratch. After a set of patterns was written, the sample was etched in 8M KOH for 1-2 s, rinsed and repassivated. Patterns were written using the software developed for field evaporation experiments.

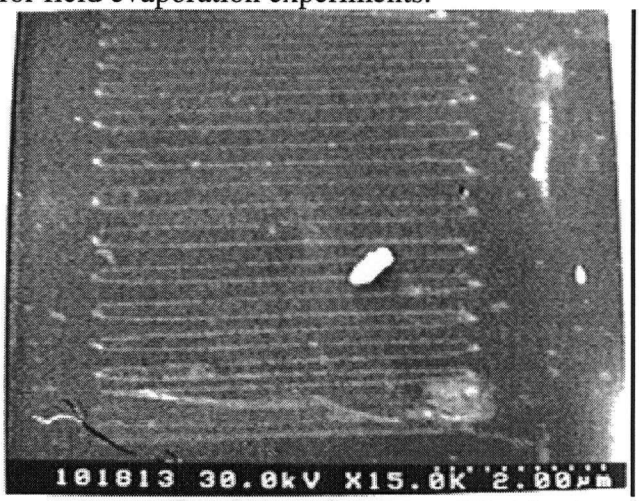


Figure 7.10 SEM image of a grating pattern written at -5V, 15 nA and etched in KOH. Line widths are approximately 30 nm.

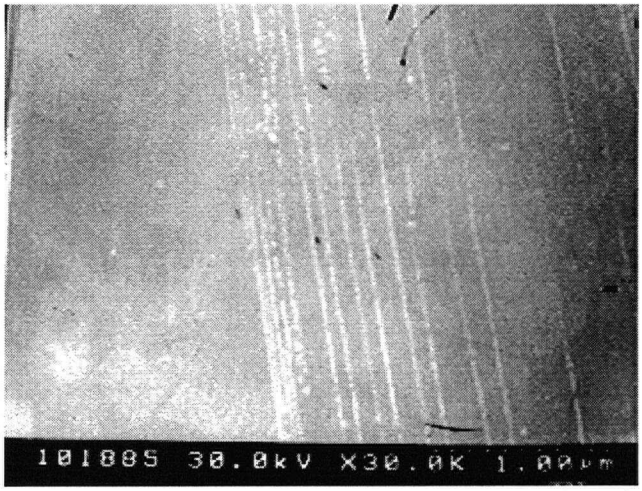


Figure 7.11: SEM image of another grating pattern written at -5V 15 nA and etched in KOH. The 20 nm wide lines have been broken up by the heavy etch.

Figure 7.10 shows an example of a grating pattern written at negative probe polarity and etched. Line widths are 30 nm, characteristic of patterns written at negative polarity. A higher magnification image of a similar grating pattern is shown in figure 7.11. Here, the etch was strong enough to begin breaking up the lines, evidence of significant undercutting. Unfortunately the 1-2 s etch period is so short that the uncertainty in time was large, making the etch difficult to control. Snow and Campbell have argued in favour of hydrazine or RIE over KOH for this reason, and because they are less prone to undercutting. Figure 7.12 shows an STM image of an etched grating. The lines are approximately 15 nm high, consistent with earlier results.[59] Note that recovery by the STM would have been impossible without the assistance of the SEM.

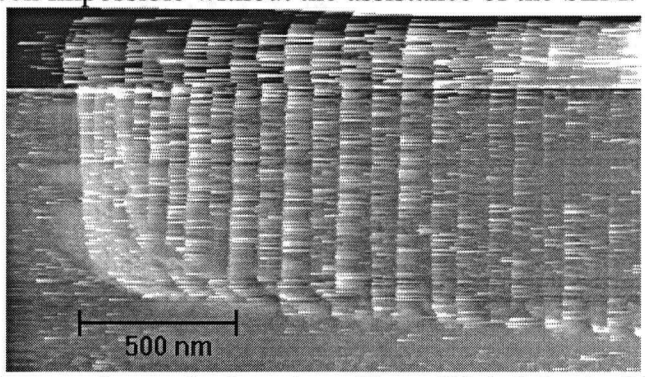


Figure 7.12: STM image of an etched grating. V = +4V, i=0.2 nA. Line height is approximately 15 nm.

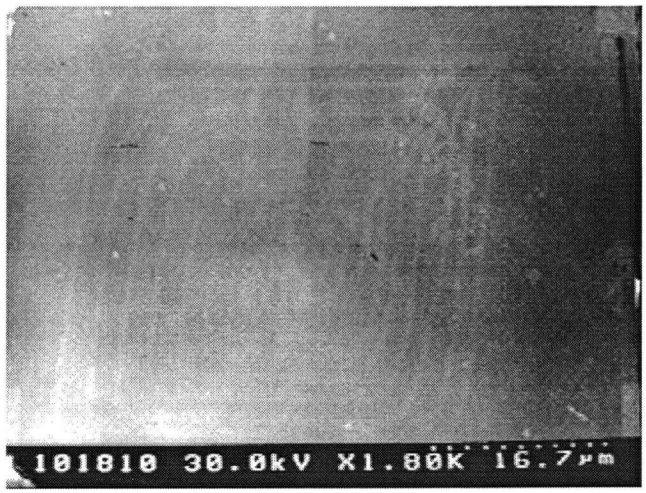


Figure 7.13: Concentric squares written at +5V 15nA and etched. Write speed increases by a factor of 20 from inside to outside, without change in linewidth.

The success rate in recovering patterns in the SEM was quite low. In some cases, the etch left deposits on the surface, which covered the patterns. In most cases though, the patterns simply failed to transfer to the substrate after the oxidation and chemical etch steps. At -5 V and 15 nA, 5 patterns were recovered from about 30 attempts. In contrast to previous work in UHV, patterns written at positive polarities were successfully transferred. The success rate was also low however, with 10 successful transfers from about 60 attempts. An example of positive pattern transfer is shown in figure 7.13. The lines are about 150 nm wide.

### 7.2(b). In-situ Imaging of Patterns and Depassivation Threshold Measurements

The discovery that the STM could image patterns directly after writing, made it possible to investigate the effect of different writing parameters without the uncertainties associated with etching. 10-30 Ωcm *n*-type Si (111) was used for most of these experiments as it was found that (111) was considerably less prone than (100) to contaminating the tip. (100) was examined however, and found to have the same threshold. (111) wafers cleave on other (111) planes at 70.5° to the top plane.[70] To observe the freshly cleaved edge, samples were mounted as shown in figure 7.14.

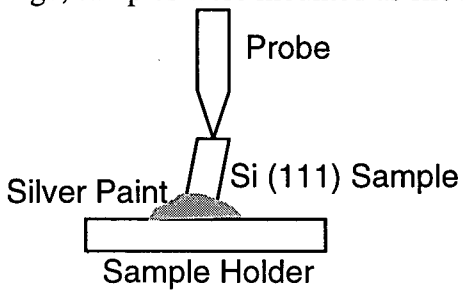


Figure 7.14: Mounting method for Si (111) samples

Figure 7.15 shows a 17 line grating where the voltage was changed for each line. Line densities were measured for a series of patterns of this type, at different current setpoints, and the results are shown in figure 7.16. Imaging was done at -10 V and 0.3 nA for almost all patterns since these parameters were found to produce the most stable

images. The voltage at which depassivation began to occur was found to be between -4 and -5 V, which closely agrees with Lyding et al.[61] This explains the low success rate of the etching experiments, where the patterns had been inadvertently written at the threshold value. In these cases depassivation may have occurred only when the probe was exceptionally clean.

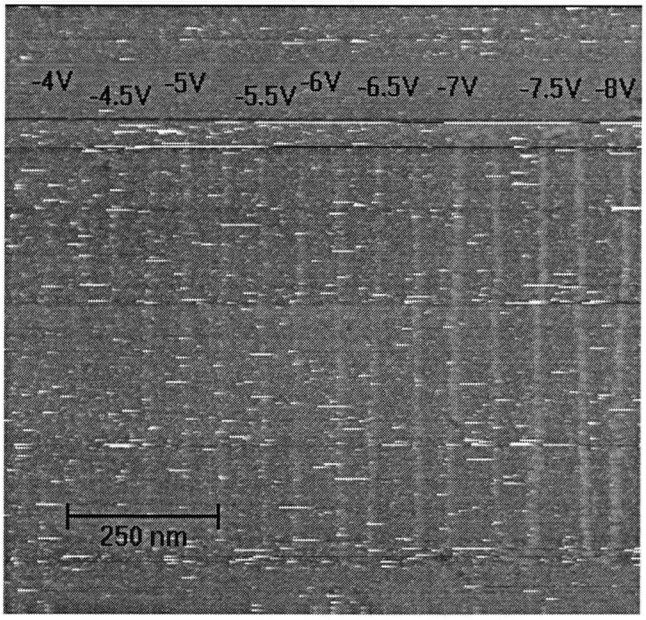


Figure 7.15: STM of depassivation threshold test pattern. Writing conditions were -4 to -8 V, i = 8 nA. Imaging was at -10V, 0.3 nA, XY = 2.0.

STM imaging of the patterns reveals some counterintuitive properties of depassivation. STM images were not significantly affected by whether the STM was operating above or below the depassivation threshold, although images were somewhat more stable at higher negative polarities. Figure 7.17 and 7.18 demonstrate the effects of reimaging above and below the voltage threshold. Imaging above the threshold depassivated the scanned area, obscuring any lithography patterns. This can be seen in Figure 7.17, where the grating has been obscured where the STM was operating at -10V, but not at -4V. A surprising result is that the STM images well while it is depassivating the surface, and depassivation of one scan line does not destroy the surface for the next. Pattern linewidths were consistently about 20 nm. A 500 line scan 1 μm across, such as

in Figure 7.15 has a scan line spacing of 2 nm. It is not known why cross line interference was not a problem. This could be investigated further.

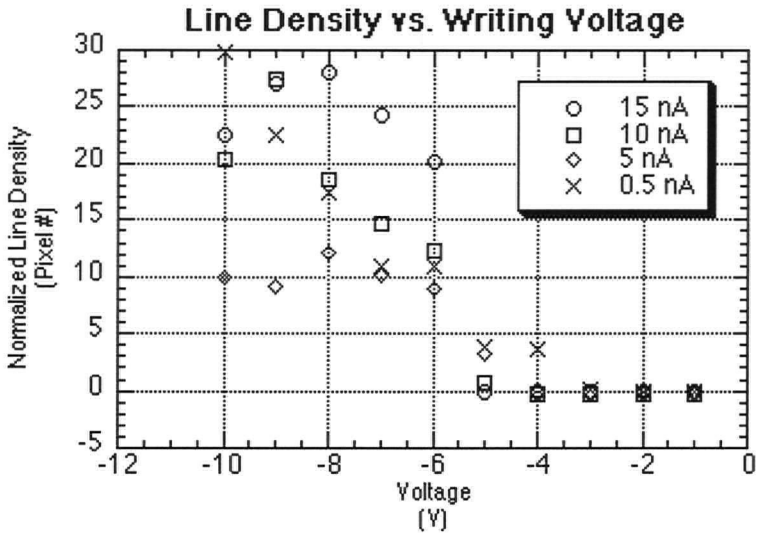


Figure 7.16: Plot of average line brightness vs. writing voltage for different currents. These measurements were normalized to compensate for differences in background brightness in different images.

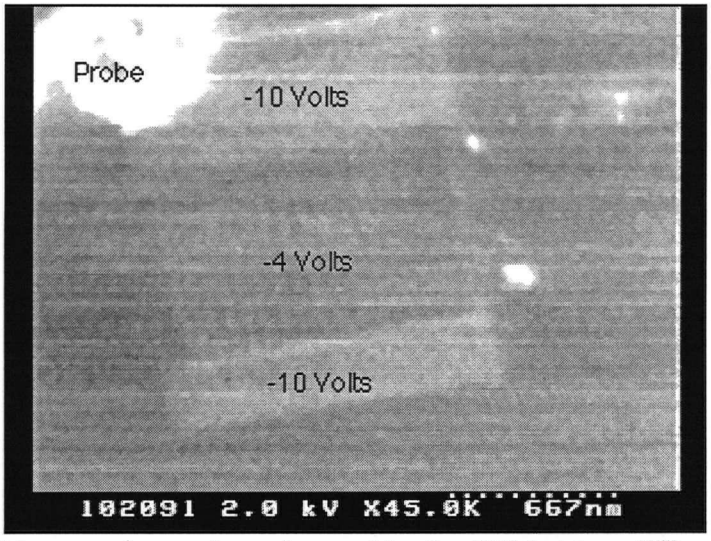


Figure 7.17: SEM image of a grating reimaged by the STM at two different voltages.

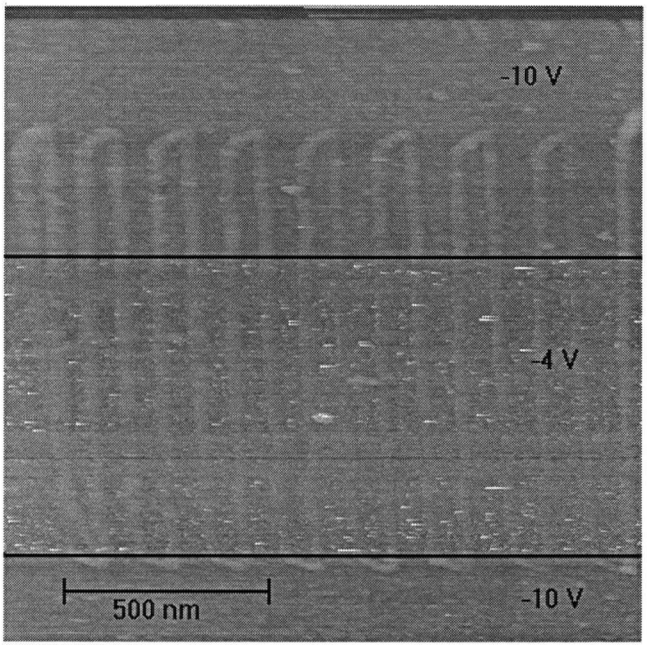


Figure 7.18: STM image corresponding to figure 7.17. i=.3 nA, XY = 3.0 A slight increase in noise is observed at -4V compared with -10V.

Varying writing speed was not found to produce measurable changes in line width, up to the maximum writing speed available, about 1μm/s. No reproducible current threshold was observed, above the threshold voltage. Increasing current did however affect writing stability. For example, when tunneling at -10V with the feedback loop integrator set at 1ms, tunneling would become unstable beyond approximately 5 nA, as shown in figure 7.19. The onset of instability can be seen in the feedback signal during writing, and closely correlates with the appearance of broader, uneven lines in the image. Instability could be easily avoided by reducing the integrator gain in the controller feedback loop.

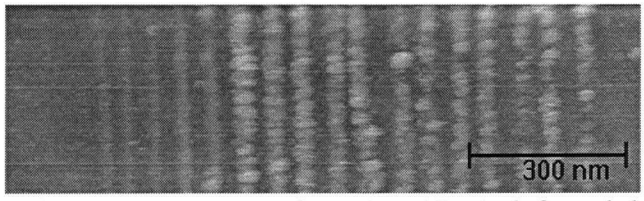


Figure 7.19. Grating where current ranges from 1 to 17 nA, left to right. V = -10 V. Instability appears at 6 nA. Imaging at V = -10V, I = 0.3 nA.

The effect of the presence of different gases was investigated. No change in the character of the lines was observed with the presence of nitrogen, air or methane, up to

$10^{-3}$ torr. Lithography was also investigated with p-type Si (100). Patterns appeared exactly the same as in the n-type case.

Line widths were consistently in the 20 nm range, except when tunneling junction instability occurred. Line heights were typically 3 nm. It is not known if this apparent height is due to increased conductivity of the line, or a physically raised structure. It is also not known whether the lines are exposed silicon, oxidized silicon, or are due to probe induced carbon deposition. The close agreement in voltage threshold with Lyding suggests the former, but as two different models exist for air and at $10^{-10}$ torr, further investigation at this pressure is warranted.

### 7.2(c) Etch Mask Formation at Positive Polarity

The insitu pattern imaging experiments led to the conclusion that an alternate mechanism for patterning at positive polarity exists, based on the probe being in contact with the sample via acquired dielectric contamination. Good pattern writing and imaging at negative polarity occurred when noise in the feedback loop was on the order of 1nm. During positive writing, the signal could fluctuate with an amplitude of 20nm or more, suggesting mechanical contact. This was particularly true of Si (100), on which the first patterns were written. Observations with carefully prepared Si (111) showed no evidence of depassivation at positive voltages when feedback noise was within about 5 nm. The increased probability of tip contamination at positive voltages is consistent with the observations of Avouris and Lyo, who determined that adsorbates move in the direction of electron flow.[71]

The etch mask for the positive patterns could either be depassivation by mechanical scraping, or coating by smearing contamination over the surface during scanning. Figure 5.8 suggests the latter. In this SEM image, the depassivated region is bright while the area under mechanical contact is dark. Had the scraped region exposed unpassivated

silicon, it should have appeared bright, like the conventionally depassivated area. Thus there is evidence that pattern writing selectively coated the surface, providing an etch mask.

A considerable difference in susceptibility to contamination was observed between Si (111) and (100), consistent with the assertion of Kasi et al, that the dihydride layer on the (100) surface is more prone to surface contamination than the monohydride layer on Si (111).[72] Positive imaging on (100) contaminated the probe very quickly and in some cases rendered the probe useless despite repeated attempts at field evaporation. Spontaneous clearing of contamination occasionally yielded a spectacular improvement in image quality, as evidenced by Figure 7.20. In this case, the STM probe was contaminated while scanning the upper half of the image, and exhibited behaviour similar to that in Figure 5.7. At the halfway point, the contamination became detached from the probe and the rest of the image was of high quality. Note that the writing itself appears clear, suggesting the contamination was picked up during imaging.

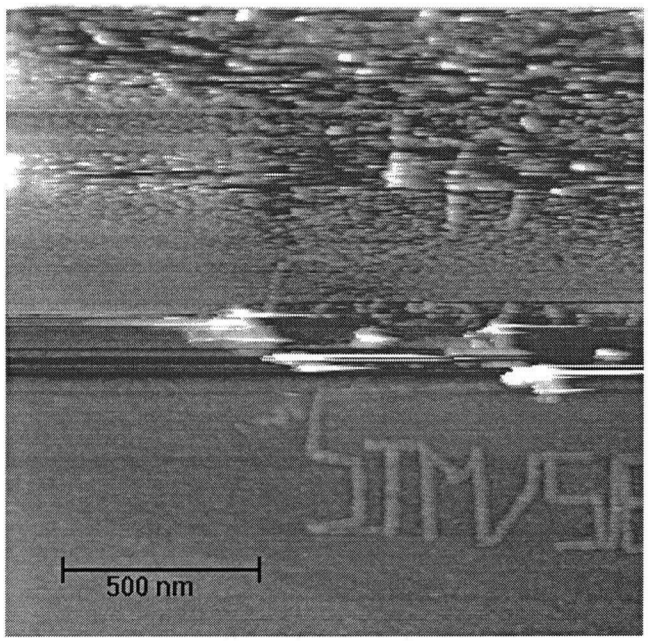


Figure 7.20: STM image (-10V, 0.3nA) of pattern written on Si (100) The clearing event at center occurred spontaneously.

### 7.2(d) SEM Imaging of Depassivation Patterns

During carbon deposition experiments it was observed that depassivated surfaces could be seen by the SEM at low accelerating voltages when the STM voltage setpoint was below 1 V. This had been previously overlooked, as all SEM imaging had been done at 30 kV. At 1 or 2 kV, the SEM could clearly see depassivated lines. The STM probe voltage must be low because of the probe's effect on secondary electrons, discussed in section 5.2(a). Line widths were near the SEM's resolution limit at low accelerating voltages. This is shown clearly in figures 7.21 and 7.22, where the linewidths in the STM image are half those in the SEM image.

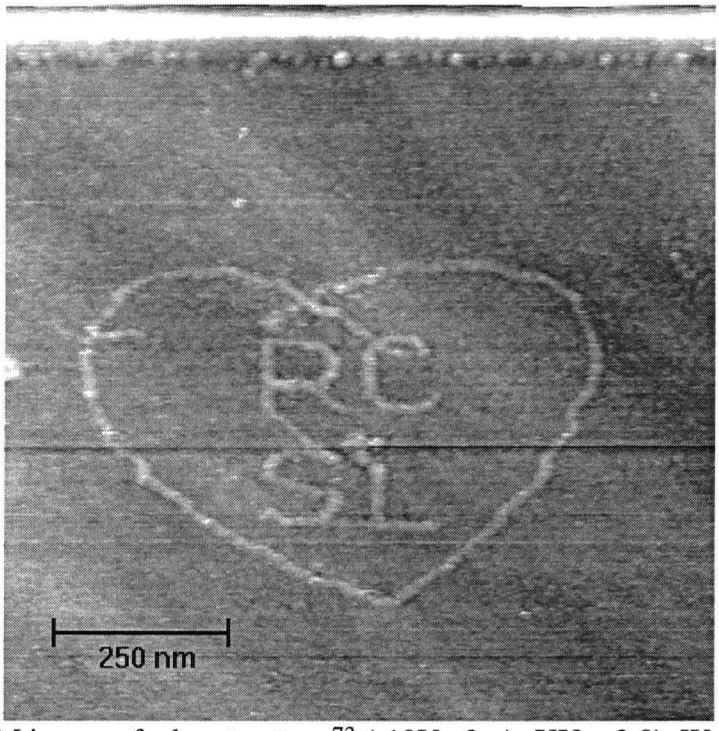


Figure 7.21: STM image of a heart pattern[73] (-10V, .3nA, XY = 2.0). Writing was done at -10V, 3 nA

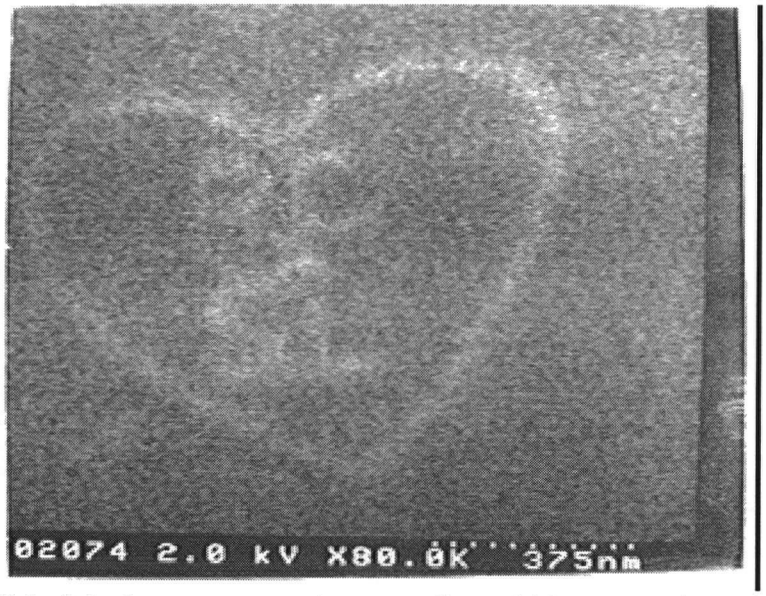


Figure 7.22: SEM of the heart pattern. Apparent line widths are on the order of 50 nm, due to low SEM resolution at this accelerating voltage.

Moore et al. have simulated the penetration depth of an electron beam into carbon at different accelerating voltages.[74] They found that penetration was reduced by an order of magnitude for a factor five decrease in accelerating voltage. Extrapolating from simulations at 25 kV and 5 kV, an average penetration depth of 10 nm could be expected at 1 kV. This is comparable to the depth of the surface modifications.

## 8. Conclusion

Our work represents the successful development of an STM which operates in conjunction with a Hitachi S-4100 field emission SEM. This STM is unique in several ways. A purely mechanical design, it avoids the cost and complexity associated with piezoelectric inchworm actuators and conventional linear translation stages. It further avoids potential reliability problems associated with inchworm technology. The flexure hinges have no static friction, so stick slip motion is entirely avoided. This also makes the device easily adaptable to UHV, unlike many linear translation systems with bearings. Finally the STM is very simple to run, so that operators can be easily trained in its use.

The field emission SEM's ability to image with high resolution at low accelerating voltages was exploited to yield some novel observations of STM tip-surface interactions. In particular the ability of the SEM to image depassivated silicon allowed a number of scan artifacts to be seen and explained. These included simultaneous imaging and dielectric contact, imaging of large steps and the effect of a finite tip radius, tip sticking to the surface, field evaporation, and multiple tips. This instrument was also used to investigate lithography by the depassivation of silicon. This led to a new mechanism for lithography at positive polarities. Future work in this area could exploit the SEM's alignment capabilities to produce devices incorporating a mixture of e-beam and depassivation lithography.

When the combined STM/SEM was originally developed, the primary motivation was to use it as the SEM alignment tool for the STM. Ideally, once the STM's probe had been aligned with a region of interest, excellent images could be readily produced. In practice, the quality of STM images is highly variable, and many attempts have to be made to obtain good images. The SEM has proven to be an invaluable diagnostic tool in determining when and how the STM is imaging poorly, and can save a great deal of time by helping to guide the user to a solution to imaging problems.

The STM itself worked well, but a future instrument could incorporate several improvements. Firstly, the space in the SEM chamber could be put to greater use if a three axis STM, using flexure hinges, were mounted on a separate XY stage made from linear bearings. This would have the advantage of much greater range for two axes, which would make coarse probe and sample alignment easier. When development of the instrument was undertaken, it was thought that any linear bearings would allow too much vibration in the STM. This was found not to be a problem, and one movement was implemented with bearings. This arrangement was not, however, carried to its logical conclusion.

The flexure hinges themselves could be improved by silver soldering a stiffening plate on one side of the hinge, dispensing with the back plate and screws. This would lighten the hinge, but more importantly, give the hinges a greater range of motion, as interference between the screw heads and hinge control arms could be avoided. If an XY stage was employed, the three axis stage could also be dispensed with. Instead a two axis stage for the probe and a single axis for the tube and sample would improve both stiffness and axis range. Overall however, this instrument performed well, and a number of apparently unique results have been obtained.

**References**

1. G. Binnig, H. Rohrer, Ch. Gerber, and E Weibel. Appl. Phys. Lett. **40,** 178 (1982).

2. A. Stemmer, R. Reichelt, R. Wyss and A. Engel. Ultramicroscopy. **35**, 225 (1991)

3. M. Yasutake and C. Miyata. J. Vac. Sci. Technol. A. **8,** 350 (1990)

4. D.D. Perovic, M.R. Castell, A. Howie, C. Lavoie, T. Tiedje and J.S.W. Cole. Ultramicroscopy. **58,** 104 (1995).

5. Ch. Gerber, G. Binnig, H. Fuchs, O. Marti, and H. Rohrer. Rev. Sci. Instrum. **57,** 221 (1986).

6. T. Ichikawa, Y Miyazaki and Y. Koga. Ultramicroscopy. **23,** 115 (1987).

7. R. Emch, Ph. Niederman, P. Descouts, ∅ Fischer. J. Vac. Sci. Technol. A **6,** 379 (1988)

8. M. Anders, M. Mück and C. Heiden. Ultramicroscopy. **25**, 123 (1988)

9. L. Vázquez, A. Bartolomé, R. Garciá, A. Buendía and A.M. Baró. Rev. Sci. Instrum. **59**, 1286 (1988).

10. K. Takata, S Hosoki, S. Hosoka and T. Tajima. Rev. Sci. Instrum. **60**, 789 (1989).

11. E.E. Ehrichs, W.F. Smith and A.L. de Lozanne. J. Vac. Sci. Technol. **9**, 1380 (1991)

12. M. Troyon, H.N. Lei and A. Bourhettar. Ultramicroscopy. **42-44,** 1564 (1992)

13. Alexander O. Golubok and Vladimir A. Timofeev. Ultramicroscopy. **42-44,** 1558 (1992)

14. K. Nakamoto and K. Uozomi. Ultramicroscopy. **42-44,** 1569 (1992)

15. O. Yamada, Y. Nakaizumi E. Hazaki. US Patent 5,081,353 (1992)

16. G. C. Rosolen and M.E. Welland. Rev. Sci. Instrumen. **63,** 4041 (1992)

17. Paul M. Thibado, Yong Liang and Dawn A. Bonnel. Rev. Sci. Instrum. **65,** 3199 (1994)

18. Omicron Brochure

19. Topometrix Website: http://www.topometrix.com/observer.htm

20. KF. Hall, G. Chambers. US. Patent 4,635,887. (1987)

21. This is considerably finer resolution than that available from the lab's air STM. Its Klinger optical stage fine adjustment gives 50 μm per turn or about 1 μm positioning accuracy. The instrument detailed here is therefore easier to use as there is a greater margin of error in bringing the probe into tunneling range.

22. Since the probe moves much more under a near dc ramp than an ac signal. The extra sensitivity of the bending axis would be partially cancelled out by the added movement in the longditudinal axis. See section 1.6

23. Hewlett-Packard 3582A Spectrum Analyser.

24. Eugene Avallone, Theodore Baumeister III. *Marks Standard Handbook of Mechanical Engineering.* McGraw Hill (1987)

24. MASc Thesis. Thomas Henry Pinnington. *Scanning Tunneling Microscopy of Epitaxial Semiconductor Films at Ambient Pressure.* University of British Columbia (1992)

25. W.A. Harrison, *Electronic Structure and the Properties of Solids,* Dover Publications (1989)

26. Sample provided by Dr. Martine Simard Normandin, Northern Telecom.

27. Burleigh Instruments Ltd. *The Piezo Book* (1995)

28. Optodyne CDDN 3 Optical Range Finder. 125 nm resolution.

29. Micrea Fotino, Rev. Sci. Instrum. **64,** 161 (1993)

30. A.J. Melmed, J. Vac. Sci. Technol. B. **9,** 601 (1991)

31. H. Borque, R.M. Leblanc, Rev. Sci. Instrum. **66,** 2695 (1994)

32. Steve Patitsas, private communication

33. H.J Mamin, S. Chiang, H. Birk, P.H. Guethner and D. Rugar. J. Vac. Sci. Technol. B. 9, 1394 (1991)

34. Sample supplied by Alex Busch, AMPEL.

35. Private communication with Digital Instruments' Western US Sales Rep.

36. Topometrix Brochure

37. Tom Pinnington, private communication

38. Sample provided by Richard Ares, Simon Fraser University

39. Richard Ares, private communication

40. Manoj Kanskar, private communication

41. Sample gown by Shane Johnson. MBE run 410.

42. Seji Heike, Yasuo Wada, Seiichi Kondo, Mark Lutwyche, Ken Murayama and Hiroshi Kuroda. Appl. Phys. Lett. **64,** 1100 (1994)

43. E.S. Snow, P.M. Campell and P.J. McMarr. Appl. Phys. Lett. **63,** 749 (1993)

44. M. Coombs, P. Pethica. IBM J. Res. Develop. **30** 455 (1986)

45. Oliver C. Wells, *Scanning Electron Microscopy,* McGraw Hill, 1974.

46. Ludwig Reimer, *Scanning Electron Microscopy* Springer Verlag, 1985.

47. J.A. Swift, *Scanning Electron Microscopes* Barnes & Noble, 1970.

48. Audrey M Glauert Ed. *Practical Methods in Electron Microscopy.* North Holland, 1982.

49. J.A. Dagata, J. Schneir, H.H. Haray, C.J. Evans, M.T. Postek, and J. Bennett. Appl. Phys. Lett. **56,** 2001 (1990)

50. M.A. McCord, D.P. Kern and T.H.P. Chang, J, Vac. Sci. Technol. B **6** 1877 (1988)

51. R.M. Silver, E.E. Ehrichs and A.L deLozanne, Appl. Phys. Lett. **51** 247 (1987)

52. C.R.K Marrian and R.J. Colton. Appl. Phys. Lett. **56,** 755 (1990)

53. Chrisite R.K. Marrian, Elizabeth A. Dobisz and John A. Dagata. J. Vac. Sci. Technol. **10,** 2877 (1992)

54. F.K. Perkins, E.A. Dobisz, S.L. Brandow, J.M. Calvert, J.E. Kosakowski, C.R.K. Marrian. Appl. Phys. Lett. **68,** 551 (1996)

55. Hiroyuki Sugimura, Tatsuya Uchida, Noboru Kitamura, Hiroshi Masuhara. Jpn. J. Appl. Phys. **32,** 553 (1993)

56. H.J Mamin, P.H. Guethner and D. Rugar. Phys. Rev. Lett. **65,** 2418 (1990)

57. J.A. Dagata, J. Schneir, H.H. Haray, J. Bennett, W. Tseng. J. Vac. Sci. Technol. B. **9,** 1384 (1991)

58 E.S. Snow, P.M. Campbell, P.J. McMarr. App. Phys. Lett. **63** 749 (1993)

59. P.M. Campell, E.S. Snow and P.J. McMarr. Solid-State Electronics. **37,** 583 (1994)

60. E.S.Snow, W.H. Juan, S.W. Pang and P.M. Campbell. App. Phys. Lett. **66,** 1729 (1995)

61. J.W. Lyding, T.C. Shen, J.S. Hubacek, J.R. Tucker and G.C. Abeln. Appl. Phys. Lett. **64,** 2010 (1994)

62. J.W. Lyding, G.C. Abeln, T.C. Shen, C. Wang, and J.R. Tucker. J. Vac. Sci. Technol. B. **12,** 3735 (1994)

63. T.C. Shen, C. Wang, J.W. Lyding, and J.R. Tucker. Appl. Phys. Lett. **66,** 976 (1995)

64. P.M. Campbell, E.S. Snow and P.J. McMarr. Appl. Phys. Lett. **66,** 1388 (1995)

65. J.A. Dagata. Science. **270,** 1625 (1995)

66. E.S. Snow and P.M. Campbell. Science. **270,** 1639 (1995)

67. D.M. Eigler, C.P. Lutz and W.E. Rudge. Nature **352,** 600 (1991)

68. H.J. Mamin, S. Chiang, H. Birk, P.H. Guethner, D. Rugar J. Vac. Sci. Tech. B. **9,** 1398 (1991)

69. G.C. Rosolen, A.C.F. Hoole, M.E. Welland, A.N. Broers. Appl. Phys. Lett. **63,** 2435 (1993)

70. PhD. Thesis. Duncan Rogers *STM Study of Silicon Surfaces in UHV.* University of British Columbia (1994)

71. I-W. Lyo and P. Avouris. Science. **253,** 173 (1991)

72. S.R. Kasi, M. Liehr, P.A. Thiry, H. Dallaporta and M. Offenburg. Appl. Phys. Lett. **59,** 108 (1991)

73. Pattern created by Stacey Lobin

74. Andrew Moore and Alexandra Smith. *Bulletin of the Microscopical Society of Canda.* **24,** 14 (1996)

**Appendix A.** The Pattern Writing Program and Sampling Program

A Spectrum Systems TMS 320C DSP Card is used by the Quantum Vision Software to drive the STM controller. This made it the obvious choice as a platform for the pattern generating software. The software was challenging to write however, as the DSP card requires two separate programs, one which runs on the PC, and the other which runs on the DSP. These programs were developed from the programs supplied with the DSP, particularly DOTP and RAMP, respectively a dot product calculating and ramp waveform generating program.

Patterns were generated by hand on graph paper. Lines' start and end points were recorded sequentially so the end of one line became the start of the next. The coordinates of these points were then recorded along with a writing speed in microns/second. The coordinates are on a Cartesian grid ranging from -10 to 10 in x and y. The speed value with a given coordinate controls the writing speed from the previous coordinate to that coordinate. The following listing is a section of the file for writing grating patterns.

```
-10,-10,1
-10,10,.2 --- .2 µm/s to this point
-9,10,1  ---  1 µm/s to this point
-9,-10,.2
-8,-10,1
-8,10,.2
-7,10,1
-7,-10,.2
-6,-10,1
-6,10,.2
....
```

To ensure that the speed is correct, the program prompts for the XY Scale on the STM controller. This value controls the actual size of the grid, so if the XY scale is reduced, the program slows down the DSP ramp to compensate. After each line is

complete, the DSP informs the PC which tells the user how much time it took. This allows a more accurate determination of the line writing speed.

```
/*
RUNBLOB.C - Run 30BLOB.OUT  This program will accept X and Y
coordinates and time coordinates from the user and output the
appropriate signals to the DSP to write lines
*/

#include <tms30.h>
#include <stdio.h>
#include <stdlib.h>
#include <30lib.h>
#include <math.h>
#include <conio.h>
#include <time.h>
#include <dos.h>

#define BOARDADR    0x290   /* factory default io address */

#define  COMM0                  0x30000
#define  PCPROCEEDFLAG          COMM0+0
#define DSPPROCEEDFLAG          COMM0+1
#define  INPUTVECT              COMM0+2

#define  MAXCOUNT               20000
#define  M                      5

void InitBoard(void);
void timeout(void);

void InitBoard( )       /*Initialize Board and load program*/
{
int  loadstat;

SelectBoard(BOARDADR);
loadstat = coffLoad("30blob.out");

if (loadstat != 0)
 {
 printf("\n\nError During Program Load!!!!\n");
 printf("coffLoad() returned %x\n\n", loadstat);
 exit (0);
 }
}
void timeout(void){   /*Wait to see if there are problems with DSP*/
        int a;
        for(a=0;(a<MAXCOUNT) && (Get32Bit(PCPROCEEDFLAG,DUAL) != 0X1L);a++);

        if (a == MAXCOUNT){
                printf("Timeout waiting for DSP");
                exit(0);
        }
}
void main(void)
{
        float startcoord[3],endcoord[3],inputvect[M],length,scale;
```

```
int ch,i,j,inputvectloc;
char filename[30];
clock_t  start,end;
FILE  *fp;

clrscr();
InitBoard();

printf("\n\nWelcome to Pattern Writer, the STM lithography Program\n");
printf("\nThis program uses text files written as lists of\n");
printf("of coordinates as follows: <x,y,spped> (no spaces) \n");
printf("Each line is wriiten from the coordinate preceeding\n");
printf("to the new coordinate.  The speed is in microns/second\n");
printf("The coordinate system is based on a grid of +/- 10 units in X and Y\n");

printf("Enter the name of the file to read:  ");
gets(filename);

printf("Enter the XY Scale from the controller  ");
scanf("%f", &scale);

if ((fp=fopen(filename,"r")) == NULL) {
printf("Can't open file %s\n" , filename);
exit(1);
}
else{
fp=fopen(filename,"r");
fscanf(fp," %f,%f,%f\n",&startcoord[0],&startcoord[1],&startcoord[2]);          /*Read in one set of coords*/
}
i=0;
while(fscanf(fp," %f,%f,%f\n",&endcoord[0],&endcoord[1],&endcoord[2]) != EOF){  /*repead until EOF*/
        inputvect[0] = startcoord[0]/4;                                         /*Scale for DSP program*/
        inputvect[1] = startcoord[1]/-4;                                        /* This is a fix for the DSP*/
        inputvect[2] = endcoord[0]/4;
        inputvect[3] = endcoord[1]/-4;

        inputvect[4] = endcoord[2]/scale*10;                    /*Send nortmalized rate to DSP*/

        Put32Bit(PCPROCEEDFLAG,DUAL,0X0L);
        Put32Bit(DSPPROCEEDFLAG,DUAL,0X0L);
        Reset();        /* Start the DSP program.   */
        timeout();      /*Subroutine*/
        Put32Bit(PCPROCEEDFLAG,DUAL,0X0L);

        inputvectloc = Get32Bit(INPUTVECT,DUAL);

        WrBlkFlt(inputvectloc,DUAL,M,inputvect);

        Put32Bit(DSPPROCEEDFLAG,DUAL,0x1L);

        printf("The STM is writing line #  %d . . . ",i+1);
        start = clock();
        while(Get32Bit(PCPROCEEDFLAG,DUAL) != 0x1L){
                end = clock();
                if((end-start)/CLK_TCK > inputvect[4]*length+25){
                  printf("Timeout waiting for DSP\n");
                  exit(0);
                }
        }
        sound(440);
        printf("done\n");
```

```
                printf("The line is %.3f microns long and ",length);
                printf("took %.2f sec to write\n",((end-start)/CLK_TCK));
                nosound();
                for(j=0;j<=2;j++)
                startcoord[j] = endcoord[j];   /*Set old end cood to new start coord */
                i++;
                }
        Put32Bit(PCPROCEEDFLAG,DUAL,0X0L);
        fclose(fp);
        printf("\nThank you for using fwrite. We hope your pattern came out.\n");
        AssertReset();
        }
}
```

Tremendous difficulties were encountered trying to get a PC program to compile using the coffload() function. coffload() is used by the PC to upload the DSP program. Finally, a file called coffsml.obj was obtained from Spectrum which solved the problem. coffsml.obj must be included in the make file.

The following program runs on the DSP. Data is transferred between the two programs by functions (ReadBlkFlt, WrtBlkFlt, etc, which are used in the PC program) This program takes each pair of co-ordinates and calculates a step size for X and Y. Problems have been encountered with round off error so diagonal line writing is not perfect. Writing speed is also not entirely accurate. Maximum writing speed is software limited to 1 μm/s.

```
/*
30BLOB.C -    Generate a ramp waveform and output it via the
                  Channel A  D/A.
*/
asm (" .length 58");         /* Adjust assembly language listing  */
asm (" .width  120");        /* (filename: 30SINOUT.LST).         */

#define  MINVAL     -32768        /* Min amplitude of ramp.    */
#define  MAXVAL      32767        /* Max amplitude of ramp.    */
#define  N   5

#define DACaddressA (int *) 0x804000
#define DACaddressB (int *) 0x804001
#define SWtrigger   (int *) 0x804008
#define StereoControl (int *) 0x800004
#define StereoA (int *) 0x800006
#define StereoB (int *) 0x800007

#define  ON    8000
#define  OFF   0

#define  XChannel    0                /*Specify which channel each */
```

```
#define  YChannel    1                  /*output is on            */
#define  Pulsechannel 2
#define  Conversion   13106             /*distance to integer factor */

#define  DELAYTIME    108               /*delay function so timing is*/
                                        /*correct                 */
float inputvect[N];                     /* Input row vector array (from PC).*/
long  *PCproceedflag,*DSPproceedflag;   /* PC communication flags.  */

extern  long  Comm0, Comm1;             /* Use these absolute-location      */
                                        /* communication parameters for flags.*/
extern float   *Comm2;          /* Pointers to array inputvect      */

void Delay(float maxval){               /*delay loop so lines write at appropriate speed*/
int i;
for(i=0;i<=(maxval);i++);
}

void main()
{

float i,j,length;                       /*loop variables for writing  */
float x1,x2,y1,y2,time;                 /*simpler cordinate variables */
float xincrement,yincrement;
float  Delayval;

PCproceedflag = &Comm0;                 /* Assign meaningful names to pointers to    */
DSPproceedflag= &Comm1;                 /* flags used to communicate with PC.        */

Comm2 = inputvect;                      /* Locate starting address of input          */

*PCproceedflag = 1;                     /* Tell PC that all pointers are initialized.  */
                                        /* (The PC inits this to zero, then puts it    */
                                        /* back to zero after each time it goes high.) */


while (*DSPproceedflag == 0)            /* Wait for PC to download input arrays. */
 ;

*DSPproceedflag = 0;            /* Set flag back to zero (not needed    */
                                        /* here, but it's good form).          */

x1 = Conversion*inputvect[0];           /*Convert inputs to 16 bit integers */
x2 = Conversion*inputvect[2];
y1 = Conversion*inputvect[1];
y2 = Conversion*inputvect[3];
time = inputvect[4];

if(abs(x2-x1)<abs(y2-y1)&&((x2-x1)!=0)){       /*assign increments based*/
   xincrement = 1;                      /*on lengths of movement */
   yincrement = abs((y2-y1)/(x2-x1));    /*in each direction*/
   }
else if(abs(x2-x1)<abs(y2-y1)&&((x2-x1)==0)){
   xincrement = 1;
   yincrement = 1;
   }
else if(abs(x2-x1)>abs(y2-y1)&&((y2-y1)!=0)){
   xincrement = abs((x2-x1)/(y2-y1));
   yincrement = 1;
   }
else{
```

```
   xincrement = 1;
   yincrement = 1;
   }

i = x1;
j = y1;

Delayval = DELAYTIME/time;

if((x1>x2)&&(y1>y2)){                    /*four separate cases depending*/
 while((i>=x2)||(j>=y2)){                /*on the direction of the line*/
          *DACaddressA = (int)(i) <<16;  /* Output X value */
          *DACaddressB = (int)(j) <<16;  /* Output Y value */
          *SWtrigger =1;
          Delay(Delayval);
          if(i>=x2)
          i=i-xincrement;
          if(j>=y2)
          j=j-yincrement;
  }
}
else if ((x1<=x2)&&(y1>y2)){
 while((i<=x2)||(j>=y2)){
          *DACaddressA = (int)(i) <<16;
          *DACaddressB = (int)(j) <<16;
          *SWtrigger =1;
          Delay(Delayval);
          if(i<=x2)
          i=i+xincrement;
          if(j>=y2)
          j=j-yincrement;
  }
}

else if ((x1<=x2)&&(y1<=y2)){
 while((i<=x2)||(j<=y2)){

          *DACaddressA = (int)(i) <<16;
          *DACaddressB = (int)(j) <<16;
          *SWtrigger =1;
          Delay(Delayval);
          if(i<=x2)
          i=i+xincrement;
          if(j<=y2)
          j=j+yincrement;
  }
}

else if ((x1>x2)&&(y1<=y2)){
 while((i>=x2)||(j<=y2)){
          *DACaddressA = (int)(i) <<16;
          *DACaddressB = (int)(j) <<16;
          *SWtrigger =1;
          Delay(Delayval);
          if(i>=x2)
          i=i-xincrement;
          if(j<=y2)
          j=j+yincrement;
  }
}
```

```
*PCproceedflag = 1;

} /* End of main(). */
```

The XY Sampling program, was a modification of the Pattern writing software. In this case, the DSP was used to sample input on two channels, save the result in an array, and pass it back to the PC when sampling was ended.

```
/*
RUNSAMPL.C - Run 30SAMPLE.OUT This program will sample input to the DSP
for a specified period and number of samples and then output an array to a text
file
*/

#include <tms30.h>
#include <stdio.h>
#include <stdlib.h>
#include <30lib.h>
#include <math.h>
#include <conio.h>
#include <dos.h>

#define BOARDADR    0x290   /* factory default io address */

#define COMM0                   0x30000
#define PCPROCEEDFLAG           COMM0+0
#define DSPPROCEEDFLAG          COMM0+1
#define ASAMPLEVECT             COMM0+2
#define BSAMPLEVECT             COMM0+3
#define IOVECT                  COMM0+4

#define MAXCOUNT                20000
#define N                   10000
#define Conversion              10922

void InitBoard(void);
void timeout(void);

void InitBoard( )       /*Initialize Board and load program*/
{
int loadstat;

SelectBoard(BOARDADR);
loadstat = coffLoad("30sample.out");

if (loadstat != 0)
 {
 printf("\n\nError During Program Load!!!!\n");
 printf("coffLoad() returned %x\n\n", loadstat);
 exit (0);
 }
}

void timeout(void){   /*Wait to see if there are problems with DSP*/

        int a;
```

```
        for(a=0;(a<MAXCOUNT) && (Get32Bit(PCPROCEEDFLAG,DUAL) != 0X1L);a++);

        if (a == MAXCOUNT){
                printf("Timeout waiting for DSP");
                exit(0);
        }
}

void main(void)
{

        float j,Asamples[N],Bsamples[N],iovect[2];
        int i,numsamples,Asampleloc,Bsampleloc,iovectloc;
        char restart,Afilename[30],samplecontrol[1];
        FILE *fpA;

        clrscr();
        InitBoard();

        printf("\n\nWelcome to SAMPLE 4.0, the DSP sampling program\n");
        printf("This program takes input on DSP Channels A and B\n");
        printf("over a specified period and saves the data in a text file\n");

        restart = 'y';
        while(restart == 'y'){

        printf("Input the name of the file to write to: ");
        gets(Afilename);
        printf("Enter the sampling frequency in Hz: ");
        scanf( "%f",&iovect[0]);

        Put32Bit(PCPROCEEDFLAG,DUAL,0X0L);
        Put32Bit(DSPPROCEEDFLAG,DUAL,0X0L);
        Reset();        /* Start the DSP program.   */
        timeout();      /*Subroutine*/
        Put32Bit(PCPROCEEDFLAG,DUAL,0X0L);

        iovectloc = Get32Bit(IOVECT,DUAL);
        WrBlkFlt(iovectloc,DUAL,2,iovect);      /*download freq */

        printf("Press RETURN to begin sampling  ");
        scanf( "%s" ,samplecontrol);

        Put32Bit(DSPPROCEEDFLAG,DUAL,0x1L);  /*Start DSP conversions*/

        printf("The DSP is now sampling.....\n");
        printf("Press RETURN to stop  ");
        scanf( "%s" ,samplecontrol);

        Put32Bit(DSPPROCEEDFLAG,DUAL,0x0L);

        RdBlkFlt(iovectloc,DUAL,2,iovect);
        numsamples = (int)(iovect[1]);

        Asampleloc = Get32Bit(ASAMPLEVECT,DUAL);
        RdBlkFlt(Asampleloc,DUAL,numsamples,Asamples);

        Bsampleloc = Get32Bit(BSAMPLEVECT,DUAL);
        RdBlkFlt(Bsampleloc,DUAL,numsamples,Bsamples);

        if ((fpA=fopen(Afilename,"w")) == NULL) {
```

```
        printf("Can't open file %s\n" , Afilename);
        exit(1);
        }
        else{
        Asamples[0] = 0.0;
        Bsamples[0] = 3*Conversion;
        Asamples[numsamples] = Asamples[numsamples-1];
        Bsamples[numsamples] = Bsamples[numsamples-1];
        fpA=fopen(Afilename,"w");
        for(i=0;i<=numsamples && i<=N ;i++)
        fprintf(fpA," %10.6f%10.6f\n",Asamples[i]/Conversion,Bsamples[i]/Conversion);
        fclose(fpA);
        }

        Put32Bit(PCPROCEEDFLAG,DUAL,0X0L);
        printf("Would you like to do another sample? (y/n)");
        scanf("%s",&restart);
        }
}
```

The following program runs on the DSP, and actually samples input.

```
/*
30SAMPL.C -   Generate a ramp waveform and output it via the
                Channel A  D/A.
*/
asm (" .length 58");        /* Adjust assembly language listing  */
asm (" .width  120");       /* (filename: 30SINOUT.LST).         */

#define  MINVAL    -32768       /* Min amplitude of ramp.    */
#define  MAXVAL     32767       /* Max amplitude of ramp.    */
#define  N          10000

#define DACaddressA (int *) 0x804000
#define DACaddressB (int *) 0x804001
#define SWtrigger   (int *) 0x804008

#define  ON   8000
#define  OFF  0

#define  Conversion  10922          /*distance to integer factor */

#define  Delaytime  288120          /*delay factor so timing is  */
                                                  /*correct              */
float Asample[N],Bsample[N],inputvect[2]; /* Input row vector array (from PC).*/
long  *PCproceedflag,*DSPproceedflag;   /* PC communication flags.  */

extern long  Comm0, Comm1;        /* Use these absolute-location      */
extern float  *Comm2, *Comm3, *Comm4; /* communication parameters for flags.*/
                                        /* Pointers to arrays      */


void Delay(float maxval){     /*delay loop so lines write at appropriate speed*/
int i;
for(i=0;i<=(Delaytime/maxval);i++);
}


void main()
```

```
{

int  i,j,numsamples;            /*loop variables for writing */
float frequency;


PCproceedflag = &Comm0; /* Assign meaningful names to pointers to     */
DSPproceedflag= &Comm1; /* flags used to communicate with PC.         */

Comm2 = Asample;   /* Locate address of frequency and time*/
Comm3 = Bsample;
Comm4 = inputvect;

*PCproceedflag = 1;    /* Tell PC that all pointers are initialized.  */
                       /* (The PC inits this to zero, then puts it    */
                       /* back to zero after each time it goes high.) */


while (*DSPproceedflag == 0)   /* Wait for PC to download input arrays. */
 ;
frequency = inputvect[0];
numsamples=0;

while(*DSPproceedflag == 1){

        i = *DACaddressA >> 16;          /* Actual Sampling Step */
        j = *DACaddressB >> 16;
        *SWtrigger = 1;
        if(numsamples<N){
          Asample[numsamples]=i;         /*Add samples to array */
          Bsample[numsamples]=j;
          numsamples++;
          inputvect[1] = numsamples;
          }
        Delay(frequency);                /*User input delay length */
        }

*PCproceedflag = 1;

} /*  End of main(). */
```

**Appendix B.** STM Operation

The combined STM/SEM is as straightforward as any conventional air STM to use, except that the all movements are made with rotary feedthroughs. The user must therefore be familiar with which rotary feedthrough corresponds to which movement, and which rotating direction corresponds to which movement. There are also limitations in how far each hinge can move, so the user must know how to determine when axes have reached the limit of their ranges. Following is a guide to mounting samples and probes, and how to install and use the instrument in the SEM.

Part I. Mounting the probe and sample

Step 1. Turn off the SEM's objective aperture heater. The heater must be off for at least 30 minutes to allow the objective to cool before it is brought to atmosphere.

Step 2. Mount the sample. In this research, conducting paint was most commonly used to secure samples on the SEM sample stubs. Another approach for flat samples is to stick the sample down with an Avery Spot-o-Glue sticker, then connect a strip of copper tape from the sample holder to the sample. Edge on samples should be mounted across the center of the sample holder for good alignment (see step 6). When the STM is tilted, the top of the sample will be in the right position.

Step 2. The sample holder must be installed **before** the probe. The sample holder is held on the piezotube by a set screw located on the sample stub holder opposite the vacuum plate. Use a 0.050 hex key to secure it. Do not tighten the screw too much or it will strip. If you are using an insulated sample holder, connect the holder lead to the ground wire with the socket.

Step 3. Check that all X and Y axes are near the center of their ranges of motion. The position of the Z adjustment can be checked by looking at the side of the probe stage, under the back of the probe Y axis control arm. There is a gap between the probe stage base plate and the bottom of the Z hinge. A compression spring in the gap pushes up against the Z set screw. The limit of downward motion is reached when the round screws on either side of the spring contact the bottom of the gap. There should be at least 2 mm of clearance before starting. If the Z set screw is backed off too far, pressing lightly down on the stage will produce some movement. If the set screw is in proper contact, it preloads the hinge, so pressing down takes more effort, and provides a clear stop when the hinge is returned.

Step 4. The probe mounts in a hinged block controlled by a set screw which is adjusted by a flat screwdriver (See figure 1.4). It should be in the up position when installing the probe. To hold the probe more firmly in the syringe tube, the probe can be kinked slightly, then pushed in. The last 5 mm or so of the probe should be bent. The easiest way is to bend it sideways, then rotate it down with the tweezers.

Step 5. Manually aligning the probe is an iterative process. The probe can be brought down with the set screw, and the position checked. If the probe must be moved, it should be backed off first, then moved down again. The probe should contact the the surface 0.5 to 1 mm in front of the center of the sample holder, and a similar distance to the right, looking from the vacuum end of the instrument. Sometimes, the STM must be installed, and the SEM turned on, before the amount of necessary readjustment can be determined

Step 6. The probe should be brought within at least 0.5 mm of the surface with the coarse adjust, although separations of 0.25 mm can easily be achieved. With a smooth flat sample, the separation between the probe and its reflection on the sample is a good indicator of the gap.

Part II: Exchanging the SEM stage and STM.

This phase should not be attempted without first consulting those in charge of the SEM, who can supervise the procedure.

Step 1. With the objective now cool, the chamber can be vented. Remove the 4 hex head bolts on the large vacuum flange with a 5 mm hex key.

Step 2. Make sure the SC air lock valve on the SEM is **closed** and the specimen stage is **unlocked**. Switch the vacuum control from "SEC" to "SC". **Open** the Specimen Exchange Chamber Air Lock Valve.

Step 3. Press the "Air" button. Hold the SEM stage from the bottom rails, hooking your thumb around the current monitor connector on the right side. When the chamber is vented, gently remove the stage and place it on a safe, clean surface. The stage can be covered with plastic to prevent dust accumulation.

Step 4. Remove the STM from its stand by grasping the feedthroughs. Get the two alignment cylinders through the holes, and slide the STM into the chamber, **being careful not to catch any wires in the vacuum seal.**

Step 5. Press the "evac" button. When the SC vacuum and SEC vacuum lights go green, close the exchange chamber airlock, switch the vacuum control to SEC and lock

the specimen stage. Do not turn on the objective heater until you are sure the probe is aligned properly.

Step 6: While the chamber is pumping down, connect the cables to the STM. Make sure the cables are connected properly. If the high voltage cable is connected to the pre-amp circuit, it is possible to blow the preamp.

Step 7: Once finished using the STM, the SEM stage can be replaced by following the previous steps in reverse.

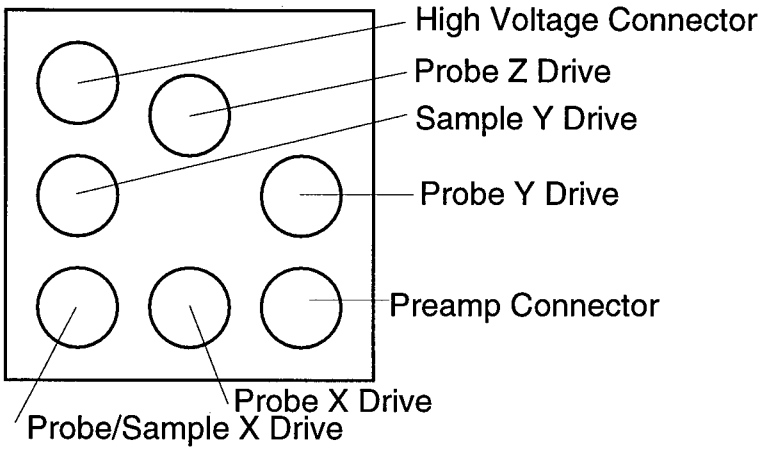


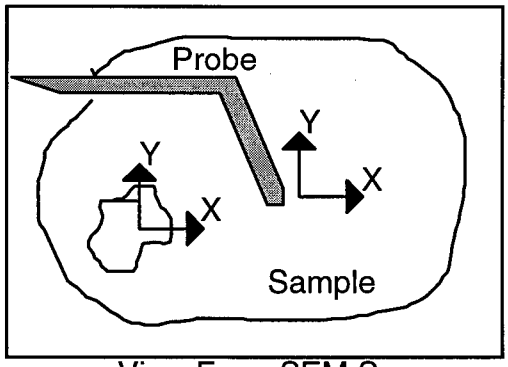


View From SEM Screen

| Movement: | Feedthrough Movement |
|---|---|
| Probe Z Up | Counter Clockwise |
| Probe Z Down | Clockwise |
| | |
| Probe X Right | Counter Clockwise |
| Probe X Left | Clockwise |
| | |
| Probe Y Up | Clockwise |
| Probe Y Down | Counter Clockwise |
| | |
| Probe/Sample X Right | Counter Clockwise |
| Probe/Sample Y Left | Clockwise |
| | |
| Sample Y Up | Clockwise |
| Sample Y Down | Counter Clockwise |

Figure B1: Location of feedthroughs, corresponding sample and probe axes and a table of how feedtrhough movements correspond to probe sample movements

Part III: Using the STM

Figure B1 shows which feedthrough controls which movement, and how. The axes with off axis decouplers all have significant backlash. These feedthroughs must be rotated through six turns to go from actuating in one direction, to actuating in the other. The best operating strategy has been found to only back the feedthrough off about 90° after moving a hinge. The user should keep track of which direction the last movement was made in each axis. It is desirable to avoid turning a feedthrough too fast, hitting the decoupler, and over shooting the target when attempting to make a small movement. If the position of the decoupler is known, such incidents can be avoided.

Range of movement of the STM is relatively limited. The area that can be viewed by the SEM at low magnification is not all accessible. It is important therefore to start with the probe and sample within a millimeter or so of the region of interest. It is also important to be aware of when the axes are reaching their limits of motion. A table of the axis limiting effects is provided below.

| Condition: | Cause: |
|---|---|
| Probe Y too low | screw out, probe stops moving |
| Probe Y too high | screw in. axis becomes hard to turn |
| Sample Y too high | screw out, probe stops moving |
| Sample Y too low | screw in. axis becomes hard to turn |
| Probe Z too low | screw in. axis becomes hard to turn |
| Probe Z too high | screw out, probe stops moving |
| Probe X too far right | screw in. axis becomes hard to turn |
| Probe X too far left | screw out, probe stops moving |
| Sample/Probe X too far right | screw in. axis becomes hard to turn |
| Sample/Probe X too far left | screw out, probe stops moving. Can interfere with probe X axis, making the probe move with respect to the sample |

Do not force the axes if they are screwed in; it will result in damage to the U-joints or set screws. If one of the axes reaches its limit of motion before probe and sample are correctly aligned, STM will have to be removed and the probe of sample manually

realigned. Once again, it is important to make sure the axes are all near the center of their ranges of motion before starting, so that the best initial alignment possible can be made.

Lowering the probe, causes it to move "down screen" with respect to the sample, from the perspective of the SEM, because of the 30° tilt. If the probe is above the desired tunneling site, it will be necessary to periodically move it up in Y while closing the Z gap. The other option is to bring the probe down until it is tunneling, then bring it up a few turns and move it in X and Y. When attempting to image epilayers, it is important to continually monitor whether the probe leaving the edge of the sample as it is brought down. Making sure the probe is directly above the sample with the STM mounted horizontal on its stand helps.

The SEM's focus gives some indication of the probe sample gap. If the end of the probe and sample surface are within a turn of the fine focus adjustment, the STM is within two or three turns of the Z feedthrough. Due to the high quality of the S-4100 SEM, the tip shadowing effect is not really effective, except at low accelerating voltages with the STM off, which isn't very helpful.

If the sample surface is perfectly level with respect to the STM stage, the tip retract is sufficient to be able to move the sample in X and Y. However, if a serious effort is being made to not crash the tip, it should be raised at least a turn before making other movements.